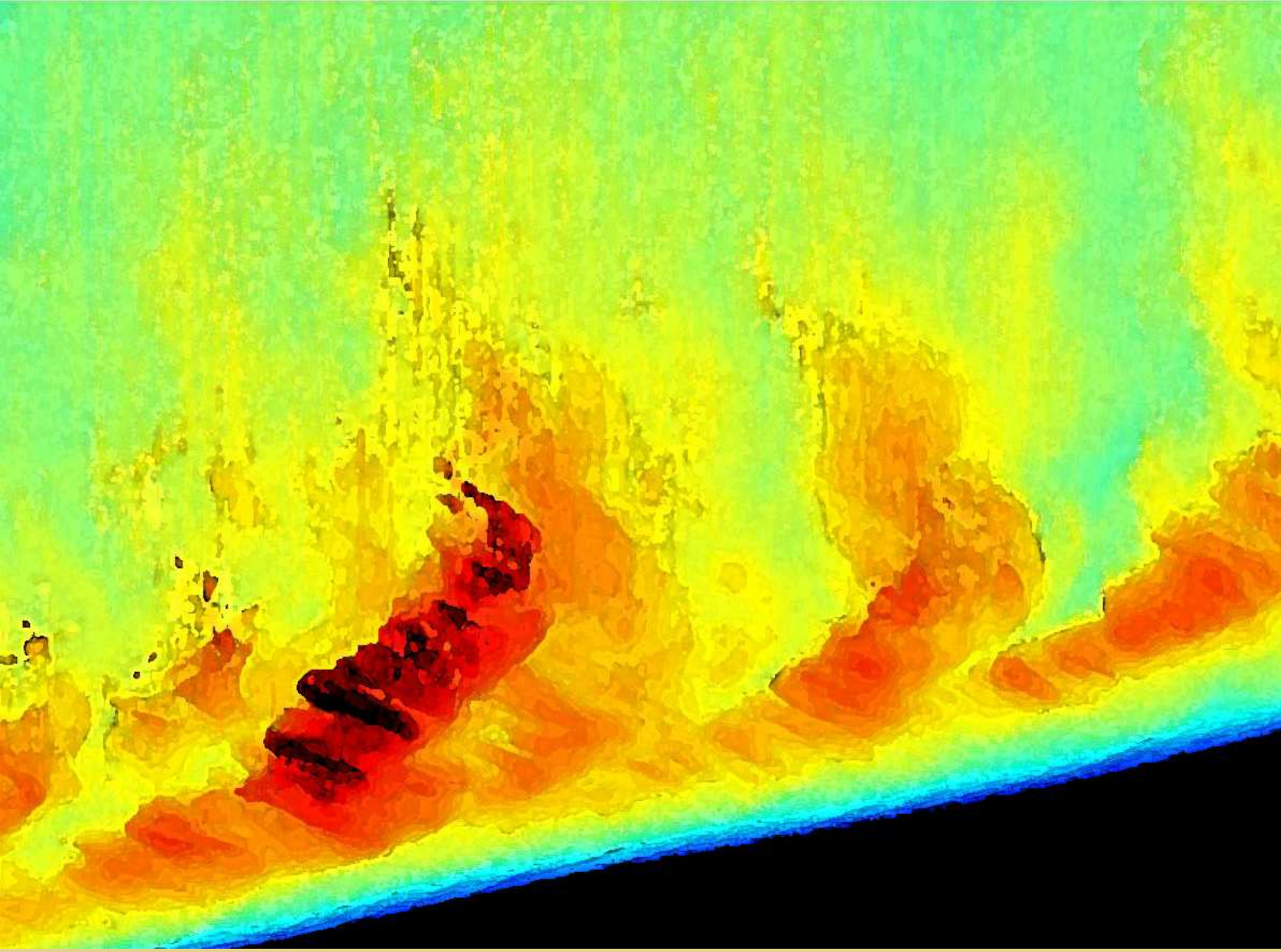

Helena Isabel dos Santos Nogueira

EXPERIMENTAL CHARACTERIZATION OF UNSTEADY GRAVITY CURRENTS DEVELOPING OVER SMOOTH AND ROUGH BEDS

PhD Thesis in the scientific area of Civil Engineering, speciality of Hydraulics, Water Resources and Environment, supervised by Professor Mário Jorge Rodrigues Pereira da Franca and Doctor Elsa Cristina Tavares Lourenço Alves, submitted to the Department of Civil Engineering of the Faculty of Sciences and Technology of University of Coimbra

Coimbra 2013

· U C ·

UNIVERSIDADE DE COIMBRA

· U C ·

UNIVERSIDADE DE COIMBRA

FACULTY OF SCIENCES AND TECHNOLOGY
DEPARTMENT OF CIVIL ENGINEERING

EXPERIMENTAL CHARACTERIZATION OF UNSTEADY GRAVITY CURRENTS DEVELOPING OVER SMOOTH AND ROUGH BEDS

Helena Isabel dos Santos Nogueira

PhD Thesis in the scientific area of Civil Engineering, speciality of Hydraulics, Water Resources and Environment, supervised by Professor Mário Jorge Rodrigues Pereira da Franca and Doctor Elsa Cristina Tavares Lourenço Alves, submitted to the Department of Civil Engineering of the Faculty of Sciences and Technology of University of Coimbra

Coimbra, November 2013

Abstract

Gravity currents are flows driven by density differences between two contacting fluids resulting from temperature gradients, dissolved substances or solid particles in suspension. The release of pollutants into rivers, oil spillage on the sea environment and desalination plant outflows are a few of man-made gravity currents that occur in water masses and frequently cause negative environmental impacts. Examples of gravity currents occurring spontaneously in nature are the sea-breeze and oceanic fronts, underwater debris flows and turbidity currents. Despite the comprehensive knowledge to date on such flows, their dynamics and impact are still topics for research.

The aim of the present work is to experimentally investigate the influence of the initial density gradient and of the bed roughness on the kinematics and dynamics of unsteady gravity currents. The *lock-exchange* technique is herein used, in which two fixed volumes of fluids with different densities, initially at rest in a tank, are put in contact when the gate separating them is rapidly removed, originating a dense current flowing near the tank bed while, simultaneously, a current formed by lighter fluid flows above the dense current, in the opposite direction. Focus is here given to the denser current and to its time-varying complex flow pattern.

Two sets of lock-exchange experiments were performed using both image analysis and Particle Image Velocimetry (PIV) techniques. An image analysis technique was herein developed to assess the two-dimensional width-averaged instantaneous density field. This technique, based on dye concentration in the flow, permits the visualization and characterization of the gravity current allowing the understanding of its general dynamics and, more specifically, of the head dynamics. A PIV system was used in the second set of experiments to measure the two-dimensional instantaneous flow velocity field, in a vertical plane positioned along the tank centerline. This allowed the characterization of the inner flow pattern and of the shear instabilities present in the mixing layer between denser and lighter currents. The influence of the bed roughness and of the initial density gradient on the dynamics of the current and, more specifically, their influence on the propagation of the dense current and on the mixing with the ambient fluid is assessed and

discussed.

Keywords: Gravity Currents, Image Analysis Technique, Particle Image Velocimetry, Entrainment, Density Distribution, Velocity Field.

Resumo

As correntes de densidade são escoamentos gerados por diferenças de densidade entre dois fluidos em contacto, resultantes de gradientes de temperatura, substâncias dissolvidas ou particulas sólidas em suspensão. O lançamento de poluentes em rios, o derramamento de óleo no ambiente marinho e as correntes salinas resultantes de centrais de dessalinização são alguns exemplos de correntes de densidade que ocorrem em massas de água com impactos negativos no ambiente. A brisa do mar, as correntes oceânicas, os fluxos de detritos submersos e as correntes de turbidez constituem exemplos de correntes de densidade expontâneas na natureza. Apesar de extenso o conhecimento actual sobre estas correntes, a sua dinâmica, evolução e impacto são ainda tópicos de investigação.

Esta dissertação tem por objectivo investigar experimentalmente a influência do gradiente inicial de densidade e da rugosidade do leito na cinemática e dinâmica de correntes de densidade não permanentes. A técnica *lock-exchange* é aqui utilizada, na qual dois fluidos de diferentes densidades e volumes fixos, inicialmente em repouso num tanque, são colocados em contacto assim que a comporta que os separa é rapidamente removida, originando uma corrente densa junto ao fundo do tanque e, em simultâneo, uma corrente de fluido menos denso movendo-se sobre a corrente mais densa, na direcção oposta. O objecto da investigação aqui apresentada é a corrente mais densa e o seu escoamento complexo e variável no tempo.

Foram realizadas duas séries de ensaios usando técnicas de análise de imagem e de *Particle Image Velocimetry* (PIV). O campo bidimensional e instantâneo da massa volúmica, por unidade de largura do escoamento, foi avaliado através de uma técnica de análise de imagem aqui desenvolvida. Esta técnica, baseada na concentração de corante no escoamento, permite a visualização e caracterização da corrente, clarificando a sua dinâmica geral e, em particular, da zona frontal. Um sistema de PIV foi utilizado na segunda série de ensaios para medir o campo bidimensional e instantâneo de velocidades do escoamento, num plano vertical posicionado no centro do tanque. A caracterização do padrão interno do escoamento foi assim possível, tal como das instabilidades presentes na interface entre a corrente e o fluido ambiente. A influência da rugosidade do leito e

do gradiente inicial de densidade na dinâmica da corrente e, mais especificamente, na propagação da corrente densa e na mistura com o fluido ambiente é avaliada e discutida.

Palavras-chave: Correntes de Densidade, Técnica de Análise de Imagem, Particle Image Velocimetry, Incorporação de Fluido Ambiente, Distribuição de Densidades, Campo de Velocidades.

Acknowledgments

These four years of research were perhaps the richest and most exciting years of my life. In this big journey I met inspiring people with whom I learned a lot and who I will never forget. The next lines are dedicated to thank the ones that in one way or another contributed to the completion of this thesis.

First I want to thank my supervisor, Mário Franca. It has been an honor to be his first Ph.D. student. He is probably the most enthusiastic, motivated, self-driven person I know and, as you are close to fire you tend to get warm, his energy naturally stimulated me. I appreciate all his encouragement, availability and dedication since we started working together (in the M.Sc. thesis, six years ago...!). He gave me both guidelines and freedom to explore subjects in my own way, being always supportive at optimistic. Most of all, I cherish the friendship that has grown among us through these years.

To my co-supervisor, Dr. Elsa Alves, I would like to thank her support and encouragement through these years. I want to thank her specially for providing a space at LNEC where I could work comfortably in the last two years.

To Prof. Claudia Adduce, who had the role of co-supervising my research leading to this thesis, I want to thank the opportunity to perform experiments in the University of "Roma Tre" and all the support given during that period. I also acknowledge her valuable help in data analysis and interpretation. Her pragmatism reflected in her comments and suggestions was an added value to this research.

I met inspiring people during scientific meetings with whom I had the pleasure to discuss and to have their feedback on my work. I want to thank Profs. Rui Ferreira, Fabian Bombardelli, Dubravka Pokrajac, Wim Uijtewaal, Michele La Rocca, Giampiero Sciortino, Mustafa Altinakar, Jose Anta, Thorsten Stoesser and Vladimir Nikora. Each one, in their own way, helped me to pursue and to refine my research goals. I am grateful for all the discussion to clarify the physics underlying gravity currents and also for the additional material they provided me, including pre-

sentations and papers.

I had the opportunity to work with master students which was an enriching experience for me. I acknowledge the excitement of Alexandre Sousa and his insights on the dynamics of the gravity current head. It was also a pleasure to work with Riccardo Sabatini, Miguel Dias and Andreia Lopes.

Fortunately I met colleagues experiencing the same as me in this roller coaster ride, and by sharing each others experiences we could find an enormous support and energy to keep going. At the end, we all became friends. Here is included my "twin", Valentina Lombardi. She was my right arm in the Hydraulics Laboratory of University Roma Tre and without her I would have spent twice the time to accomplish the experiments. The discussions we had together were both fun and stimulating. Our physical resemblances gave us a lot of fun moments. I remember that it was particularly fun the moment when, at River Flow 2010 conference, Prof. George Constantinescu congratulated me for the presentation given by Valentina. I feel fortunate to have met my Italian twin, I know I have made a friend for a lifetime. I want to thank Ana Margarida Ricardo for being always there for me. As "friends are for the occasions", she has been my colleague, friend, neighbor, cat sitting assistant, dancing partner, nurse when I was caught by a "tropical" virus, etc... We had great time together but the best is yet to come! To my friend Inés Mera Rico I am grateful to share thoughts and experiences with her for the last three years. Since she left Lisbon, she has been my "online" support friend. I want to thank her for always finding five minutes of her time to write motivating words to me, shortening the distance that geographically separates us. Muchas gracias "Giraldilla"! I appreciate those days I worked side by side with Marina Filonovich and Edgar Ferreira. I want to thank the nice discussion moments and all the support they provided me and, of course, their friendship. To my friend Silvia Saggiori I want to thank her for all the good moments we spent together and for her great italian food! Lisbon is just not the same without you. To my poet partner, Rui Aleixo, I want to thank him for accepting the challenge and not letting me alone in the stage! Fernando Pessoa would be proud of us.

To live in Rome during the first year of Ph.D. was a great experience for me. That challenge made me grow both personally and professionally (unfortunately also in weight, after such delicious pasta, pizza, gelato...) I want to thank my colleagues from the Hydraulics Laboratory of Roma Tre, and to the friends in general I have made during my stay in Rome, for making my days in Rome unforgettable. Grazie amici!

I want to thank my colleagues of the Department of Hydraulics and Environment at LNEC for

welcoming an outsider. I appreciate the discussion moments at lunch time, except when the topic is football...

Finally, special gratitude and love goes to my family (including Jeremias, my cat), for their support, encouragement and patience. I want to thank my lovely nieces, Inês and Maria, for the leisure and play time together.

Romain, thank you for always being by my side. Je t'aime.

This research was supported by the Portuguese Foundation for Science and Technology (FCT) with the research grant SFRH/BD/48705/2008 and the research project PTDC/ECM/099752/2008, and by the European Fund for Economic and Regional Development (FEDER) through the Program Operational Factor of Competitiveness (COMPETE) FCOMP 01 0124 FEDER 009735.

An acknowledgment is owed to the following institutions that supported this thesis: Faculty of Sciences and Technology of the University of Coimbra, Coimbra, Portugal; Institute of Marine Research - Marine and Environmental Research Centre (IMAR-CMA), Coimbra, Portugal; Department of Civil Engineering, University of Rome, "Roma Tre", Rome, Italy; Department of Hydraulics and Environment of the National Laboratory of Civil Engineering, Lisbon, Portugal.

Contents

List of Figures

List of Tables

Acronyms

ASTM American Society for Testing and Materials

CCD Charge-Coupled Device

EGU European Geosciences Union

IAHR International Association for Hydro-Environment Engineering and Research

ILA Intelligent Laser Applications

LDA Laser Doppler Anemometry

LDV Laser Doppler Velocimetry

LIF Laser-Induced Fluorescence

PIV Particle Image Velocimetry

PIV-S Particle Image Velocimetry Scalar

PLIF Planar Laser-Induced Fluorescence

PTV Particle-Tracking Velocimetry

RANS Reynolds-Averaged Navier-Stokes

List of Symbols

Symbol	Definition	Units
b	width of the experimental tank	m
C_c	coefficient of curvature of the roughness material	-
C_u	coefficient of uniformity of the roughness material	-
d	characteristic length scale	m
D_{10}	grain size for which 10 % of the particles, by weight, have a smaller diameter	m
D_{30}	grain size for which 30 % of the particles, by weight, have a smaller diameter	m
D_{50}	grain size for which 50 % of the particles, by weight, have a smaller diameter	m
D_{60}	grain size for which 60 % of the particles, by weight, have a smaller diameter	m
D_s	coefficient of diffusion of salt	$m^2 \cdot s^{-1}$
E	water-entrainment parameter	-
E_b	water-entrainment parameter based on bulk quantities	-
E_h	local water-entrainment parameter at the head	-
Fr	densimetric Froude number	-
Fr_b	densimetric Froude number based on bulk quantities	-
Fr_h	local densimetric Froude number at the head	-
Fr_{h_0}	densimetric Froude number computed with h_0	-
Fr_{h_m}	densimetric Froude number computed with h_m	-
Fr_{h_r}	densimetric Froude number computed with h_r	-
Fr_{h,h_0}	local densimetric Froude number at the head computed with h_0	-
Fr_{h,h_m}	local densimetric Froude number at the head computed with h_m	-
Fr_{h,h_r}	local densimetric Froude number at the head computed with h_r	-
g	acceleration due to gravity	$m \cdot s^{-2}$
g'	reduced gravity acceleration	$m \cdot s^{-2}$
g'_0	initial reduced gravity acceleration	$m \cdot s^{-2}$

g'_h	local reduced gravity acceleration at the head	$\mathrm{m{\cdot}s^{-2}}$
h	height of the gravity current	m
h_b	bulk height of the gravity current	m
h_0	initial fluid depth in the lock	m
h_m	maximum height of the head	m
h_r	height at the rear of the head	m
H	depth of the ambient fluid	m
k_s	scale of the bed roughness	m
L_h	length of the head	m
m_a	mass of ambient fluid	kg
m_s	mass of salt	kg
M_{c_0}	initial mass of the saline mixture in the lock per unit width	$\mathrm{kg{\cdot}m^{-1}}$
M_h	mass of the head per unit width	$\mathrm{kg{\cdot}m^{-1}}$
M_h^*	non-dimensional growth rate of mass of the head per unit width	-
N	number of velocity time series acquired in the x-direction	-
OW	Okubo-Weiss parameter	$\mathrm{s^{-2}}$
p	instantaneous pressure	$\mathrm{kg{\cdot}m^{-1}{\cdot}s^{-2}}$
Q_e	water-entrained discharge per unit width	$\mathrm{m^2{\cdot}s^{-1}}$
$Q_{e,h}$	water-entrained discharge at the head per unit width	$\mathrm{m^2{\cdot}s^{-1}}$
r^2	coefficient of determination	-
R	parameter of excess density of salt	-
Re	Reynolds number	-
Re_0	Reynolds number based on initial quantities	-
Re_b	Reynolds number based on bulk quantities	-
Re_h	local Reynolds number at the head	-
Ri	Richardson number	-
S_c	area of the permeable interface of the gravity current per unit width	m
S_h	area of the permeable interface of the head per unit width	m
t	time	s
t_{f1}	time corresponding to the transition between first and second phases	s
t_{rel}	time relative to the instant of current arrival to the window of visualization	s
T	time, or period, between two successive break events	s

T^*	non-dimensional period between break events	-
u	streamwise velocity component	$\mathrm{m{\cdot}s^{-1}}$
u_0	buoyancy velocity	$\mathrm{m{\cdot}s^{-1}}$
u_c	characteristic flow velocity	$\mathrm{m{\cdot}s^{-1}}$
u_d	depth-averaged streamwise velocity	$\mathrm{m{\cdot}s^{-1}}$
u_e	water-entrainment velocity	$\mathrm{m{\cdot}s^{-1}}$
$u_{e,h}$	water-entrainment velocity at the head	$\mathrm{m{\cdot}s^{-1}}$
u_f	front velocity	$\mathrm{m{\cdot}s^{-1}}$
u_{f1}	front velocity during the first phase	$\mathrm{m{\cdot}s^{-1}}$
u_i	instantaneous velocity vector $u_i = (u, v, w)$ in the direction $x_i = (x, y, z)$	$\mathrm{m{\cdot}s^{-1}}$
U	magnitude the flow velocity	$\mathrm{m{\cdot}s^{-1}}$
V	volume of the experimental tank per unit width	$\mathrm{m^2}$
V_a	volume of the ambient fluid per unit width	$\mathrm{m^2}$
V_c	volume of the gravity current per unit width	$\mathrm{m^2}$
V_{c_0}	initial volume of the saline mixture in the lock per unit width	$\mathrm{m^2}$
V_h	volume of the head per unit width	$\mathrm{m^2}$
w	vertical velocity component	$\mathrm{m{\cdot}s^{-1}}$
w_d	depth-averaged vertical velocity	$\mathrm{m{\cdot}s^{-1}}$
W	local vertically-averaged mass per unit width	$\mathrm{kg{\cdot}m^{-1}}$
x	streamwise spatial coordinate	m
x_0	lock length	m
x_i	spatial coordinates in tensorial notation $x_i = (x, y, z)$	m
x_f	streamwise front position	m
x_{f1}	streamwise front position corresponding to the transition between first and second phases	m
z	vertical spatial coordinate	m
$z_{0.5}$	height of half the maximum streamwise velocity	m
$\mathcal{L}$	spatial distance, or wave length, between front positions of two successive break events	m
$\mathcal{L}^*$	non-dimensional wave length between break events	-
α	slope angle of the channel bed	
α_i	parameters of the least-squares regression of the relation $\rho_{a_0} = f(\alpha_i, \Theta)$	-

β_i	parameters of the least-squares regression of the relation $x_f = f(\beta_i, t)$	-
γ	strain rate	s^{-1}
γ_n	normal component of the strain rate	s^{-1}
γ_s	shear component of the strain rate	s^{-1}
δ_η	shear layer thickness	m
δ_η^+	thickness of the layer of positive vorticity	m
δ_η^-	thickness of the layer of negative vorticity	m
Δt	time between two laser pulses	s
ΔT	duration of the quasi-steady streamwise flow	s
Δu	difference between mean front velocities of both denser and return currents	$m{\cdot}s^{-1}$
Δx	distance in x between adjacent points	m
Δz	distance in z between adjacent points	m
$\Delta\rho$	density difference between fluids	$kg{\cdot}m^{-3}$
$\Delta\bar{\rho}$	mean density difference of the gravity current between its final and initial configurations	$kg{\cdot}m^{-3}$
η	vorticity component in the y direction, normal to the velocity measurement plane	s^{-1}
θ	normalized duration of a stretching cycle	-
Θ	temperature of water	°C
μ_c	dynamic viscosity of the saline mixture	$kg{\cdot}m^{-1}{\cdot}s^{-1}$
ν_a	kinematic viscosity of water	$m^2{\cdot}s^{-1}$
ν_c	kinematic viscosity of the saline mixture	$m^2{\cdot}s^{-1}$
ρ	fluid density	$kg{\cdot}m^{-3}$
ρ_a	density of the ambient fluid	$kg{\cdot}m^{-3}$
ρ_{a_0}	initial density of the ambient fluid	$kg{\cdot}m^{-3}$
ρ_{a_1}	density of the lighter fluid in a stratified environment	$kg{\cdot}m^{-3}$
ρ_{a_2}	density of the heavier fluid in a stratified environment	$kg{\cdot}m^{-3}$
ρ_c	density of the gravity current	$kg{\cdot}m^{-3}$
ρ_{c_0}	initial density of the saline mixture in the lock	$kg{\cdot}m^{-3}$
$\bar{\rho}_{end}$	mean density of the gravity current in its final configuration	$kg{\cdot}m^{-3}$
ρ_h	density of the gravity current head	$kg{\cdot}m^{-3}$
ρ_s	density of salt	$kg{\cdot}m^{-3}$
ρ_d	depth-averaged density	$kg{\cdot}m^{-3}$

ρ^*	non-dimensional density	-
ρ_d^*	non-dimensional depth-averaged density	-
σ_h	standard deviation of the gravity current height	m
σ_{OW}	standard deviation of the Okubo-Weiss parameter	s^{-2}
σ_u	standard deviation of the streamwise velocity component	$m{\cdot}s^{-1}$
σ_w	standard deviation of the vertical velocity component	$m{\cdot}s^{-1}$
σ_η	standard deviation of the vorticity	s^{-1}
φ	fractional depth	-
ϕ_a	instantaneous volume fraction of water per unit volume of the saline mixture	-
ϕ_s	instantaneous volume fraction of salt per unit volume of the saline mixture	-
ψ	stability parameter for mixing in stratified flows	-
ψ_c	critical value of the stability parameter	-

a'	fluctuating component of generic flow variable a
$\bar{a}$	mean, or time-averaged, component of generic flow variable a
$\langle a \rangle$	spatial average of generic flow variable a

Chapter 1

INTRODUCTION

Contents

1.1 Motivation

Gravity or density currents are buoyancy driven flows in which differences in density between two contacting fluids result from temperature gradients, dissolved substances or solid particles in suspension. Gravity currents include a wide range of geophysical flows occurring spontaneously in nature or resulting from human intervention. In the atmosphere, examples of gravity currents driven by differences in temperature include katabatic winds, where the radiational cooling of air on the top of a mountain originates downslope flows that can reach extremely high velocity, specially in coastal areas in Antarctica and Greenland (Ball 1956, Parish and Bromwich 1991, Klein *et al.* 2001); the adverse effects of such cold flows include frost damage in agricultural fields and, since these may carry smoke or fog, affect the visibility at ports and aviation fields. Sea-breeze fronts are also generated by temperature gradients and found at many of the world's coasts; in late afternoon, the cold air mass above the sea flows under the warm air mass heated by the land. The investigation of such phenomenon is mostly motivated by pollution studies (Lalas *et al.* 1983, Ding *et al.* 2004). Avalanches of airborne snow, plumes of pyroclasts from volcanic eruptions and sand storms (cf. Figure 1.1) are atmospheric flows where suspended particles play a major role in density gradients. In the water masses, the cooling of the surface waters in polar seas and the evaporation in subtropical areas induce the sinking of the superficial dense waters. These flowing down continental slopes, known as dense overflows, undergo significant mixing with the ambient fluid until reaching the open ocean, influencing the large-scale ocean circulation system (Özgökmen and Fischer 2008, Legg 2012). The understanding of the thermohaline circulation system is particularly important for the prediction of the Earth's future climate conditions (Özgökmen and Fischer 2008). The Mediterranean overflow is an example of dense overflow occurring at the Strait of Gibraltar which feeds the Atlantic Ocean with saline and nutrient-rich water. It is originated by the exchange flow between the less dense Atlantic water, entering the Mediterranean Sea at the surface, and the saltier Mediterranean water that outflows below (Baringer and Price 1997). In Simpson (1997) a comprehensive description of gravity current flows in the environment and in the laboratory can be found, whereas Chassignet *et al.* (2012) provides a summary on the present theoretical, observational, experimental, and modeling understanding of buoyancy-driven flows.

Although gravity currents are a major issue in geophysics (Simpson 1997), they are also important in engineering, particularly in industrial safety and environmental protection. The release of pollutants into rivers, oil spillage in the ocean, outflows from both desalination plants and in-

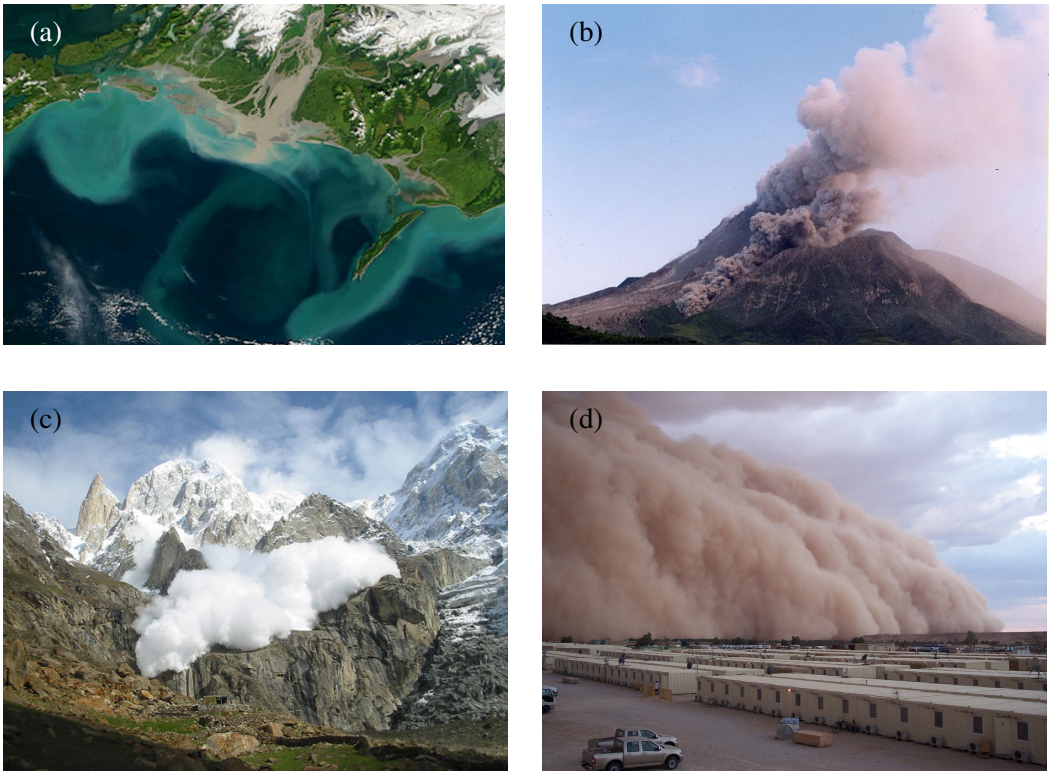

Figure 1.1: Examples of gravity currents in the environment*: (a) Copper River (upper center) spills light grey sediments into the Gulf of Alaska; (b) eruption of Soufrière Hills volcano, in the island of Montserrat; (c) avalanche from Hunza Peak, Karimabad, in Pakistan and (d) dust storm observed in the military Camp Fallujah, Iraq

dustrial cooling systems are a few examples of gravity currents induced by human activities that occur in the water masses and frequently cause negative environmental impacts. Turbidity currents transport fine sediments in suspension and are believed to be the cause for the formation of submarine canyons (Parker *et al.* 1987) and for the break of submarine cables resulting from landslide events, associated to earthquakes (Fine *et al.* 2005). The loss of storage in reservoirs, related to deposition of fine sediments transported by these currents, is a subject of great concern to hydraulic engineers and still a topic of research (Kostic and Parker 2003, Alves 2008, Alves *et al.* 2008, Khavasi *et al.* 2012). Excessive sedimentation at water intakes causes interruption in water supply and, once inside the hydraulic circuit, small sediment particles cause serious abrasion of hydraulic equipment with consequent high operating costs. Several measures have been applied over the years to control sedimentation in reservoirs (Fan and Morris 1992, Kantoush *et al.* 2010) and innovative solutions are being investigated, such as the placement of obstacles in the flow bed as a mitigation measure against sedimentation (Oehy and Schleiss 2007, Rossato and Alves 2011)

*(a) http://www.to.isac.cnr.it/aosta_old/aosta2010/index.htm
(b) http://www.geo.mtu.edu/news/Bluth_jan_04.html
(c) http://blankonthemap.free.fr/95_update/info038_ang.htm
(d) http://www.militec-1.com/index.html

and by exploring alternative methods to release sediments out of reservoirs (Althaus *et al.* 2011).

The understanding of the mechanisms involved in such flows is crucial for a proper modeling and for the development of mitigation measures against their eventual adverse effects.

1.2 Classification and definitions of gravity currents

A gravity current is the flow of a fluid with density ρ_c within an ambient fluid of different density, ρ_a. The density gradient between fluids in such currents is primarily horizontal; flows generated by vertical density gradients are described as plumes, which are not within the scope of the present study. According to the type of the density difference between the current and the ambient fluid, and the state of stratification of the latter, gravity currents can be classified as bottom currents (cf. Figure 1.2), when the current is denser than the ambient fluid, $\rho_c > \rho_a$; top currents, if the density of the current is lower than the ambient fluid, $\rho_c < \rho_a$; or intermediate currents, when the current has intermediate density value when compared to the stratified ambient fluid, $\rho_{a_1} < \rho_c < \rho_{a_2}$.

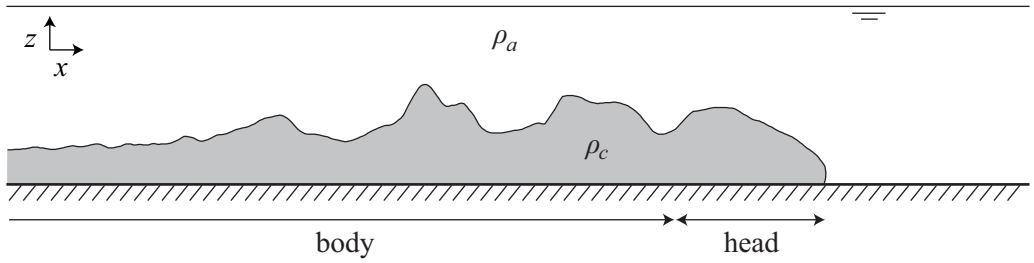

Figure 1.2: Scheme of a bottom gravity current with density ρ_c intruding in the less dense ambient fluid with uniform density ρ_a.

Gravity currents are formed by a head region, or front, advancing into the ambient fluid, being followed by the body. The current head is characterized by three-dimensional unsteady flow, being related to two dominant modes of instability which govern the mixing processes: Kelvin-Helmholtz instability and lobes and clefts (Simpson 1969, 1972, Allen 1971). Kelvin-Helmholtz billows are generated in the interfacial region, at the rear of the current head, and roll up as the current advances; these remain quasi-steadily in the current body, fading away due to continuous mixing with the surrounding fluid. Lobes and clefts are generated by a convective instability formed at the foremost region of the head, caused by the incorporation of less dense fluid by the current head during its propagation along a no-slip lower boundary. According to the initiation mechanisms and supply, the flow in the body region can be classified as unsteady or steady (or quasi-steady). In currents generated by instantaneous, or short-duration, release of heavy fluid,

the body is typically unsteady where the characteristic variables are both space and time dependent. In continuously fed gravity currents, the constant supply of denser fluid balances the density reduction of the current due to mixing with the surrounding fluid, leading to quasi-steady flow in the body region, where the characteristic variables have small variations in time.

When the density difference between fluids is caused by dissolved substances, like salt, and/or by temperature, the current is conservative since the total mass of the dissolved substance is conserved; variations in density in such currents are only due to entrainment of ambient fluid. By contrast, non-conservative gravity currents can entrain particles from the bed and/or deposit suspended material, changing the total amount of particles in the flow; examples of these are particulate, or turbidity, currents formed by granular material in suspension in the ambient fluid.

In this study, focus is given to bottom-conservative gravity currents developing over horizontal beds, generated by the instantaneous release of a saline mixture into a fixed volume of ambient fluid, the so-called "lock-exchange" problem.

1.3 State of the art and theoretical background

1.3.1 Lock-exchange gravity currents

Gravity currents have been widely studied in laboratory through both continuous (Ellison and Turner 1959, Britter and Simpson 1978, Parker *et al.* 1987, García and Parsons 1996, Cenedese and Adduce 2008, Gerber *et al.* 2011, among many others) and instantaneous (Huppert and Simpson 1980, Hacker *et al.* 1996, Marino *et al.* 2005, Adduce *et al.* 2012, Lombardi 2012) releases of a heavier fluid into other fluid of lower density. Unsteady gravity currents experiments are usually performed through the lock-exchange technique (Huppert and Simpson 1980, Rottman and Simpson 1983, Altinakar 1993, Hallworth *et al.* 1996, Zhu *et al.* 2006), which consist of the instantaneous release of a fixed volume of dense fluid into another fluid of slightly lower density. The differences in hydrostatic pressure between fluids cause the denser fluid to flow along the bottom boundary of the channel, while the lighter fluid flows along the top boundary, in the opposite direction (cf. Figure 1.3). The fractional depth, $\varphi = h_0/H$, relates the depths of the denser fluid in the lock, h_0, and of the ambient fluid in the remaining part of the channel, H; by varying this parameter, two types of lock-exchange experiments arise: full-depth releases, $\varphi = 1$, and partial-depth releases, $\varphi < 1$.

The determination of the rate of advance of such currents motivated extensive research over

the years. Gravity currents produced by the lock-exchange technique over a smooth bed present two, or even three, distinct phases: slumping phase, self-similar phase and viscous phase (Huppert and Simpson 1980, Rottman and Simpson 1983). According to Huppert and Simpson (1980), after the instantaneous release, an initial adjustment phase is observed during which the front position varies linearly with time, i.e., the front advances with approximately constant velocity. In the case of lock-exchange experiments, when the flow is confined within a channel of limited length, the initial constant-velocity phase merges into a second phase, or self-similar phase, when a bore generated at the end wall of the channel overtakes the front (Rottman and Simpson 1983). From this instant, the front position advances as $t^{2/3}$, with front speed decreasing as $t^{-1/3}$, t being the time after the gate removal. In both slumping and self-similar phases, the current development is governed by the balance between buoyancy and inertial forces. Eventually, when viscous effects overcome inertial effects, a third phase develops and the current front velocity decreases more rapidly (as $t^{-4/5}$, with front position advancing as $t^{1/5}$). Peters and Venart (2000) reported that viscous effects dominate the flow earlier in the presence of a rough bed, when compared to smooth bed experiments.

Generally, buoyancy is the engine for gravity current propagation; buoyancy forces are in turn counterbalanced by inertia as well as resistance due to Reynolds stresses and viscous drag, both acting at the upper and lower boundaries of the current. When the propagation velocity decreases, viscous stresses become important and counterbalance buoyancy as well. The development of

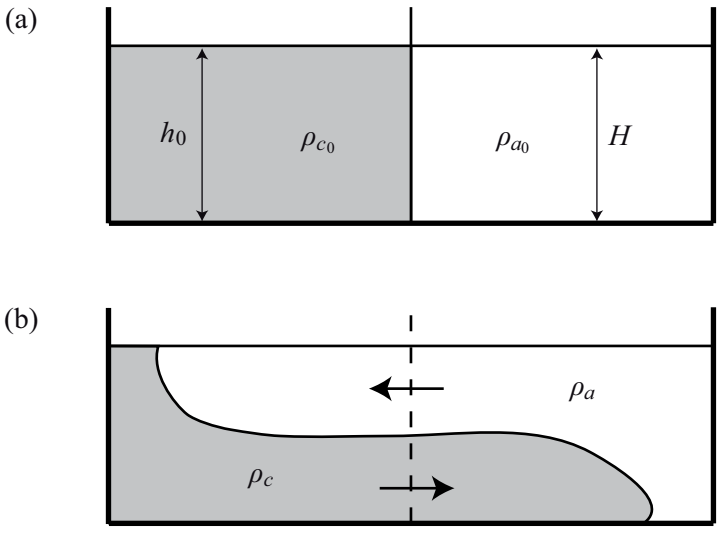

Figure 1.3: Schematic representation of the lock-exchange technique: (a) two fluids with initial densities $\rho_{c_0} > \rho_{a_0}$ are at rest, separated by a vertical gate; (b) after the gate removal, a dense current flows under the lighter fluid and a current formed with ambient fluid develops above the denser current, in the opposite direction.

gravity currents is typically an unsteady phenomenon, i.e., current kinematics and the inner density distribution are time varying, therefore the lock-exchange setup is a simple and convenient way to investigating the flow features of these particular currents.

Numerical modeling has also been used to investigate the evolution and impact of gravity currents (Härtel *et al.* 2000, Ooi *et al.* 2007, Cantero *et al.* 2007, La Rocca *et al.* 2008, Paik *et al.* 2009, Bombardelli *et al.* 2009, Tokyay *et al.* 2011, Gerber *et al.* 2011, Adduce *et al.* 2012, La Rocca *et al.* 2012a,b, Lombardi 2012). Although the motion of these currents is invariably three-dimensional, laboratory experiments and numerical results indicate that the large-scale features may be reasonably well described through a two-dimensional approach (Härtel *et al.* 2000).

Several laboratory studies have been based on image analysis techniques to investigate the dynamics of gravity currents (Hacker *et al.* 1996, Shin *et al.* 2004, Marino *et al.* 2005, La Rocca *et al.* 2008, Adduce *et al.* 2012, the last two with the very same apparatus herein used). Recent advances in measurement techniques have enabled velocity and density measurements within gravity currents. Particle Image Velocimetry (PIV) and Particle-Tracking Velocimetry (PTV) have been used to investigate the inner velocity field of the current (Alahyari and Longmire 1996, Thomas *et al.* 2003, Zhu *et al.* 2006, Adduce *et al.* 2011) and the combination of PIV with other methods, such as Laser-Induced Fluorescence (LIF) (Parsons and García 1998, Martin and García 2009) and PIV-Scalar (Gerber *et al.* 2011), allows the measurement of velocity and density simultaneously.

1.3.2 The head of gravity currents

The dynamics of the head of gravity currents has been studied extensively, both experimentally and theoretically, since the second half of the XX century (Allen 1971, Simpson 1972, Britter and Simpson 1978, Simpson and Britter 1979). The current head is characterized by a three-dimensional unsteady flow, being related to two dominant modes of instability (cf. Figure 1.4) which govern the mixing processes: i) Kelvin-Helmholtz instability, in which billows are generated at the head, induced by the opposite movement of contacting layers with different densities, breaking at the rear of the head causing ambient fluid to be entrained; and ii) lobes and clefts (Simpson 1972), generated by a convective instability formed at the foremost region of the head due to the incorporation of less dense fluid by the current head during its propagation along a no-slip lower boundary. Lobes have different velocities of propagation which leads to irregular current fronts. Clefts appear by the subdivision of large lobes and are continuously absorbed by neighbor clefts (cf. Simpson 1972).

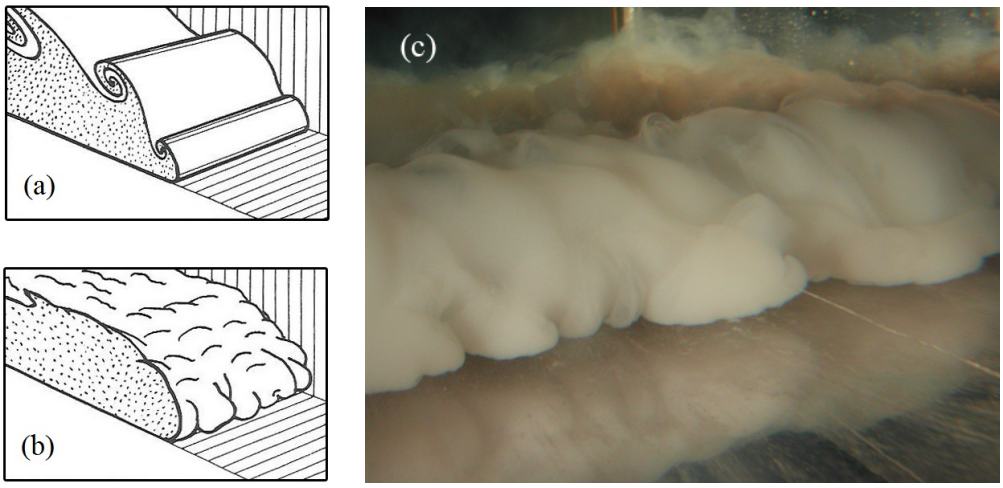

Figure 1.4: Instabilities modes at the gravity current front: (a) Kelvin-Helmholtz billows; (b) lobes and clefts (adapted from Simpson 1972); (c) Lobes and clefts structures at the front of the intruding gravity current (extracted from Neufeld 2002).

Britter and Simpson (1978) used a technique for suppressing the overrunning of the ambient fluid by the dense current, eliminating the lobes and cleft type of instability. In this way, a steady state gravity current was generated where Kelvin-Helmholtz billows were the only instability inducing mixing of the current. Using the shadowgraph technique to visualize the flow, Britter and Simpson (1978) presented a model for the structure of the flow in the head region of a stationary current where three distinct layers are identified: a lower layer of undiluted dense fluid, an upper layer of ambient fluid and the layer in between, where mixing takes place. Hallworth *et al.* (1996) and Hacker *et al.* (1996) investigated unsteady gravity currents over horizontal beds produced by the lock-exchange technique and, through two different visualization techniques, discussed the inner structure of the current. Hallworth *et al.* (1996) observed that unsteady gravity currents have a distinct inner structure when compared to steady gravity currents, namely in what regards the extent of mixing: steady currents have a shorter mixing layer, near the upper boundary, above an undiluted layer which is continuously replenished by denser fluid from the tail. This model is, in its essence, similar to the three-layer model proposed earlier by Britter and Simpson (1978). Regarding entrainment into the head region, Hallworth *et al.* (1996) argue that during the slumping phase, the head remains undiluted, i.e., no entrainment takes place and the head is progressively reduced in length. Thereafter, when the reflected bore reaches the current front, even though ambient fluid is continuously entrained into the head region, the head volume decreases as the current develops towards downstream due to mixed fluid left behind in the tail. Hacker *et al.* (1996), through an image analysis technique based on light absorption, assess the density distribution within the current

and show that this is more complex than what was previously accepted. By analyzing the temporal evolution of different iso-density contours, they observed that entrainment is present at all stages of the current development. The change of the aspect ratio of the lock, the gate removal and the Reynolds number of the flow were seen to influence the initial development of the current, leading to a broad range of density distribution within the current, originating different extents of mixing. A conclusion for the contradictory observations of Hallworth *et al.* (1996) and Hacker *et al.* (1996), regarding the stages of the current at which entrainment occurs, is still awaited (Huppert 2006).

1.3.3 Modeling entrainment

Continuously fed gravity currents are usually performed to characterize the mean structure of gravity currents in terms of velocity, density and turbulence (Simpson and Britter 1979, Martin and García 2009, Gerber *et al.* 2011, Lopes *et al.* 2013) and to study mixing processes and entrainment (Ellison and Turner 1959, Parker *et al.* 1987, García and Parsons 1996, Baines 2001, Cenedese and Adduce 2008, 2010). Entrainment and mixing processes have also been studied, but less extensively, in unsteady gravity currents by both experimental and numerical approaches (Özgökmen and Fischer 2008, Özgökmen *et al.* 2009, Adduce *et al.* 2012). Field data acquired in reservoirs provide valuable information in the investigation of entrainment between current and ambient fluid, particularly in the validation of entrainment laws (Fernandez and Imberger 2006, García *et al.* 2007).

The general characteristics of gravity currents, such as density, are important in many applications in geophysics and civil engineering and are determined by the amount of entrained fluid into the current during its evolution. Ellison and Turner (1959) drew attention to the entrainment phenomenon and performed experiments of continuously fed gravity currents over smooth bed with varying slope, with $Re \sim 1000$. The entrainment parameter is therein defined as the ratio between the velocity of entrained fluid into the current and a velocity scale of the current (E) and it is shown to be dependent on bulk Richardson number, defined as $Ri = g'd\cos\alpha/u_c^2$, where g', d and u_c are the reduced gravity, vertical length scale and characteristic velocity of the current, respectively, and α is the slope angle. Based on their experiments, the well-known relation $E = (0.08 - 0.1Ri)/(1 + 5Ri)$ was established, valid for $Ri <= 0.8$. They predict the entrainment parameter to be negligible for high Richardson numbers ($Ri > 0.8$). Their work motivated the development of further research on mixing in gravity currents (Parker *et al.* 1987, Hallworth *et al.*

1996, García and Parsons 1996, Cenedese *et al.* 2004, Princevac *et al.* 2005, Cenedese and Adduce 2010, among many others), being the parameterization of mixing in dense currents still an area of active research nowadays. The influence of Richardson number, or densimetric Froude number, on the entrainment parameter, as well as the slope of the bed, have been considered since the early works. Only recently, the dependence on Reynolds number was also investigated and seen to be fundamental in the prediction of entrainment (Princevac *et al.* 2005, Fernandez and Imberger 2006, Cenedese and Adduce 2008), especially in natural flows with high Reynolds numbers ($Re \sim 10^7$) where results deviate substantially from the laboratory-based entrainment laws, usually obtained for $Re \sim 1000$. In Adduce *et al.* (2012) a two-layer shallow water model with entrainment was developed and tested by laboratory experiments with lock-exchange gravity currents in which both initial density and initial saline volume in the lock were varied. The entrainment was found to play a key role in their simulations.

1.3.4 Roughness effects

Most of the investigation efforts concern flows developing over smooth beds, though a few investigators have studied the effect of bed roughness in the dynamics of gravity currents. Peters and Venart (2000) used Laser-Induced Fluorescence (LIF) to investigate flow dynamics and mixing processes at the head region of gravity currents developing over rough surfaces. They used regular square cross section elements to reproduce bed roughness, spanning the full channel width, with four different side dimensions. In general, they observed that roughness decreases the front velocity and induces higher dilution in the head region. According to these authors, those effects are due to two mechanisms: an increase in bed roughness induces extra bed resistance and promotes an earlier transition to the viscous/buoyant flow regime; additionally, ambient fluid trapped within the roughness layer is entrained into the current, contributing to a reduction of the buoyancy differences between current and ambient fluid which constitutes the flow driving force. In La Rocca *et al.* (2008) three-dimensional gravity currents were produced by varying the initial density of the mixture in the lock and the bed roughness of the tank, testing four mean diameters within a range of 0.7 mm to 3.0 mm in a thin layer glued to the bed. The front velocity was seen to decrease with the increase of the mean diameter of the roughness elements, this effect being more obvious in the second phase of the current development. The increase in the friction stress induced by roughness precedes the beginning of the current deceleration phase. Adduce *et al.* (2009) performed experiments with a rough bed using quartz sand. They used an image analysis technique to in-

vestigate current dynamics and confirmed the findings reported in both Peters and Venart (2000) and La Rocca *et al.* (2008) regarding roughness effects on front velocity reduction. The effect of bed roughness in the development of dense overflows, such as the Mediterranean Sea overflow, was numerically investigated by Özgökmen and Fischer (2008). The results of their simulations suggest that roughness enhances drag, with effects on the velocity field and mixing between the current and ambient fluid, modifying the density distribution within the current. Despite previous contributions, the effect of the bed roughness in the kinematics of gravity currents is far from being completely understood.

1.3.5 Governing equations

Consider a bottom gravity current developing over an horizontal bed as shown in Figure 1.5. The Cartesian coordinate system considered is $x_i = (x, y, z)$, being x, y and z the streamwise, spanwise and vertical axes directions, respectively. In this coordinate system, the corresponding components of velocity are (u, v, w). The current is advancing with front velocity $u_f(t)$ and height, denoted by $h(x, y, t)$, below the unstratified ambient fluid of depth H with uniform density ρ_a. During its development, mixing with the ambient fluid takes place leading to ambient fluid entrainment with velocity $u_e(x, y, t)$.

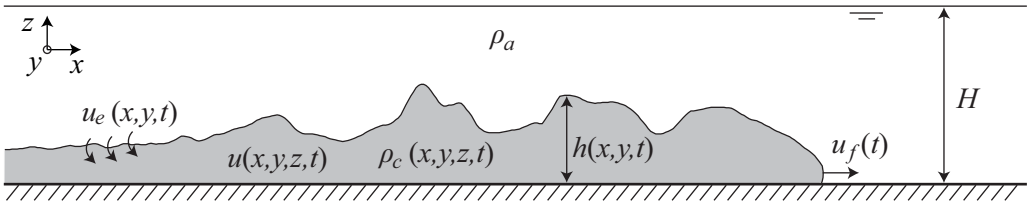

Figure 1.5: Schematic representation of a bottom gravity current and the characteristic flow variables.

The instantaneous density of the gravity current, $\rho_c(x, y, z, t)$, where the excess density is due to dissolved salt, is given by

$$\rho_c = \rho_s \phi_s + \rho_a \phi_a \tag{1.1}$$

where ρ_s is the density of salt, ϕ_s and ϕ_a are respectively the volume fractions of salt and ambient fluid in a unit volume of the current. Dividing the previous relation by ρ_a leads to

$$\frac{\rho_c}{\rho_a} = R\phi_s + 1 \tag{1.2}$$

where $R = (\rho_s - \rho_a)/\rho_a$.

The governing equations for conservative gravity currents can be derived directly from the basic principles of mass conservation of the current (Eq. 1.3), mass conservation of salt (the dissolved substance in the present case, Eq. 1.4) and momentum conservation of the current (Eq. 1.5), presented below in tensorial notation, where i and j take values 1, 2 and 3, corresponding to the directions x, y and z, respectively, leading to $\{x_1, x_2, x_3\} \equiv \{x, y, z\}$ and $\{u_1, u_2, u_3\} \equiv \{u, v, w\}$

$$\frac{\partial \rho_c}{\partial t} + \frac{\partial \rho_c u_i}{\partial x_i} = 0 \tag{1.3}$$

$$\frac{\partial \rho_s \phi_s}{\partial t} + \frac{\partial \rho_s \phi_s u_i}{\partial x_i} = D_s \frac{\partial^2 \rho_s \phi_s}{\partial x_i \partial x_i} \tag{1.4}$$

$$\frac{\partial \rho_c u_i}{\partial t} + \frac{\partial \rho_c u_i u_j}{\partial x_j} = -\frac{\partial p}{\partial x_i} + \frac{\partial}{\partial x_j}\left(\mu_c \frac{\partial u_i}{\partial x_j}\right) + \rho_c g_i \tag{1.5}$$

D_s being the coefficient of diffusion of salt, assumed constant, p the pressure, μ_c the dynamic viscosity of the saline mixture and g_i the component of acceleration due to gravity in the i^{th} direction.

Assuming that the density differences between current and ambient fluid are relatively small $(\rho_c - \rho_a)/\rho_a << 0.1$ (Graf and Altinakar 1998), the Boussinesq approximation can be applied and the density differences can be neglected in the inertia terms, appearing only in the term associated to gravity since this is the flow driving force. Considering that the transport of salt by diffusion is negligible when compared with the advective transport and assuming the fluid incompressible (but non-homogeneous), the previous equations can be simplified to

$$\frac{\partial u_i}{\partial x_i} = 0 \tag{1.6}$$

$$\frac{\partial \phi_s}{\partial t} + \frac{\partial \phi_s u_i}{\partial x_i} = 0 \tag{1.7}$$

$$\frac{\partial u_i}{\partial t} + \frac{\partial u_i u_j}{\partial x_j} = -\frac{1}{\rho_a}\frac{\partial p}{\partial x_i} + \nu_a \frac{\partial^2 u_i}{\partial x_j \partial x_j} + (R\phi_s + 1)g_i \tag{1.8}$$

where ν_a is the kinematic viscosity of the ambient fluid. Equation 1.6 is the continuity equation for an incompressible fluid and states that the divergence of the velocity field is zero. The first term of Eq.1.7 is the local rate of change of salt volume fraction in time, per unit volume of the current, whereas the second term stands for the rate of change, per unit volume, of the same quantity by advection. The member on the left of Eq. 1.8 represents the rate of change of momentum per unit volume of the mixture, where the first and second terms are the local and advective flow

accelerations, respectively. The member on the right of Eq. 1.8 shows the forces responsible by fluid acceleration: the first two terms correspond to the contact forces due to local pressure and viscosity, the last term representing the forces of mass, induced by the action of gravity.

The instantaneous quantities in the equations above can be separated into their mean and fluctuating components by application of the Reynolds decomposition:

$$a(x,y,z,t) = \bar{a}(x,y,z) + a'(x,y,z,t) \tag{1.9}$$

where $\bar{a}(x,y,z)$ is the time average of a generic flow variable a, given by $\bar{a}(x,y,z) = \frac{1}{\Delta t}\int_{\Delta t} a(x,y,z)\mathrm{d}t$, and $a'(x,y,z,t)$ is its instantaneous fluctuating component, being $\bar{a'} = 0$. Analogously, it follows: $u_i = \bar{u}_i + u_i'$, $\phi_s = \bar{\phi}_s + \phi_s'$ and $p = \bar{p} + p'$. Substituting these relations in the equations (1.6) to (1.8), and time-averaging over a time period larger than the largest characteristic period of the turbulent fluctuations of the flow and smaller than the flow macro-scale variables, i.e., a time interval small enough to not smooth out the unsteady character of the flow (Aleixo 2012), the mean conservation equations for mass and momentum are obtained:

$$\frac{\partial \bar{u}_i}{\partial x_i} = 0 \tag{1.10}$$

$$\frac{\partial \bar{\phi}_s}{\partial t} + \frac{\partial}{\partial x_i}\left(\overline{\phi_s u_i} + \overline{\phi_s' u_i'}\right) = 0 \tag{1.11}$$

$$\frac{\partial \bar{u}_i}{\partial t} + \frac{\partial \overline{u_i u_j}}{\partial x_j} = -\frac{1}{\rho_a}\frac{\partial \bar{p}}{\partial x_i} + \frac{\partial}{\partial x_j}\left(\nu_a \frac{\partial \bar{u}_i}{\partial x_j} - \overline{u_i' u_j'}\right) + (R\bar{\phi}_s + 1)g_i \tag{1.12}$$

Comparing this set of equations with Eqs. 1.6 to 1.8, one concludes that most of the terms were replaced by their time-averaged equivalent. An exception is the term $\overline{\phi_s' u_i'}$, in Eq. 1.11, related to the rate of change of the salt fraction due to velocity fluctuations, and the term $\overline{u_i' u_j'}$, in Eq. 1.12, related to the Reynolds stresses, $-\rho_a \overline{u_i' u_j'}$, representing, in the mean flow, the transport of fluctuating momentum by the velocity fluctuations (turbulent fluxes).

Statistics of unsteady flows, as are lock-release gravity currents, can be obtained by ensemble averaging the characteristic flow variables over several realizations of the same experiment in the same conditions, as applied previously to transient turbulent flows (Brocchini and Peregrine 2001, Pokrajac and Kikkert 2011, Aleixo 2012, among others). In the present research, several realizations of the same experiment were not performed. However, it was observed that the time-series of each measured velocity component, $u(t)$ and $w(t)$, are similar among different locations within the

flow. Moreover, the time-series of u showed the existence of two regions within the current with quasi-steady behavior. This feature is highlighted when depth-averaging the streamwise velocity, $u_d(x,t)$, since a good collapse among time series obtained at each x is observed (see Chapter 5 for more details). To assess the Reynolds stresses in those quasi-steady flow regions, the characteristic flow variables were averaged over the time interval, ΔT, where flow steadiness is observed, followed by an 'ensemble average', or spatial average, over x, of the N velocity time series acquired in the streamwise direction. Vertical profiles of Reynolds stresses, for each of the quasi-steady flow regions observed, are thus given by:

$$\langle \overline{u_i' u_j'} \rangle (z) = \frac{1}{N} \sum_{x=1}^{N} \overline{u_i' u_j'}(x,z) \tag{1.13}$$

1.4 Research questions

Gravity currents have been studied over the years through field observations, laboratory experiments and theoretical approaches. The main motivation to study such phenomena is the natural applications to flows in rivers, oceans and atmosphere, as well as to many engineering and industrial problems. Despite the comprehensive knowledge to date on gravity currents, there are still some aspects open for discussion. In general, most of the investigation efforts concern flows developing over smooth beds; the effect of bed roughness on the kinematics and dynamics of such flows is not completely explored. The conditions for which entrainment of ambient fluid into the current occurs is still waiting for conclusion, as well as an adequate entrainment parametrization. Furthermore, there is a lack of characterization of the velocity, vorticity and turbulence fields within gravity currents; this should give a good insight towards the understanding of the mixing mechanisms and of the interaction of the current with its upper and lower boundaries.

The present study aims at contributing experimentally to the characterization of the kinematics and dynamics of unsteady gravity currents. The influence of the bed roughness and of the initial excess density is analyzed by both bulk and local approaches, with special attention being given to the current head. More specifically, this research intends to answer the following questions:

- ◊ Q_1 - *How does the bed roughness and the initial density gradient affect the velocity of propagation and the density distribution of gravity currents?*

- ◊ Q_2 - *In which stages of the gravity current development does entrainment occur? How is it affected by the bed roughness and the density gradient? How does entrainment affect the*

head dynamics?

◊ Q_3 - *What are the effects of the bed roughness on the inner velocity, vorticity and turbulence fields?*

The results presented in Chapter 3 will contribute to answer question Q_1 and partially question Q_2. The most substantial contribution to answer Q_2 comes from Chapter 4, whereas the results presented in Chapter 5 are devoted to answer the last question, Q_3. These questions will be summarized in the conclusions chapter together with their answers.

1.5 Original contributions

A number of contributions emerged during these four years of research, either by papers published (or submitted) in peer-reviewed journals or by papers published in conference proceedings. These are listed below together with the indication of the chapter where their content was included.

◊ Nogueira, H.I.S., Adduce, C., Alves, E. and Franca, M.J. (2013). Kinematic characterization of unsteady gravity currents developing over smooth and rough beds. *Manuscript submitted for publication.* (Chapter 5).

◊ Nogueira, H.I.S., Adduce, C., Alves, E. and Franca, M.J. (2013). Dynamics of the head of gravity currents. *Env. Fluid Mech.* DOI: 10.1007/s10652-013-9315-2 (Chapter 4).

◊ Nogueira, H.I.S., Adduce, C., Alves, E. and Franca, M.J. (2013). Analysis of lock-exchange gravity currents over smooth and rough beds. *J. Hydr. Res.* 51(4), 417 - 431 (Chapter 3).

◊ Nogueira, H.I.S., Adduce, C., Alves, E. and Franca, M.J. (2013). Image analysis technique applied to lock-exchange gravity currents. *Meas. Sci. Technol.* 24(047001) (Section 2.3).

◊ Nogueira, H.I.S., Adduce, C., Alves, E., Franca, M.J. (2013). Phase analysis of the stretching cycles of the head of unsteady gravity currents developing over smooth and rough beds. *Proc. 35th IAHR World Congress*, Chengdu, China, 8-13 September (Chapter 4).

◊ Nogueira, H.I.S., Adduce, C., Alves, E., Franca, M.J. (2012). The influence of bed roughness on the dynamics of gravity currents. *Proc. River Flow 2012*, San José, Costa Rica, 5-7 September (Chapter 4).

◊ Nogueira, H.I.S., Adduce, C., Alves, E. and Franca, M.J. (2012). Visualization and characterization of gravity currents over rough beds by means of PIV measurements. *Proc. 2nd IAHR Europe Congress*, Munich, Germany, 27-29 June (Chapter 5).

◊ Nogueira, H.I.S., Adduce, C., Alves, E. and Franca, M.J. (2012). Periodic cycle of stretching and breaking of the head of gravity currents. *Geophysical Research Abstracts* 14(3486), EGU General Assembly, Vienna (Chapter 4).

◊ Nogueira, H.I.S., Adduce, C., Alves, E. and Franca, M.J. (2012). Dynamics of the head of gravity currents. *Proc. 4th IAHR International Symposium on Hydraulic Structures*, Porto, Portugal, 9-11 February (Chapter 4).

◊ Nogueira, H.I.S, Adduce, C., Alves, E. and Franca, M.J (2011). Phase analysis of lock-exchange gravity currents. *Proc. 7th International Symposium on Stratified Flows*, Rome, Italy, 22-26 August (Chapter 3).

◊ Nogueira, H.I.S (2011). Time and space analysis of entrainment on density currents. *Proc. 34th IAHR World Congress.*, Brisbane, Australia, 26 June - 1 July (Chapter 3).

◊ Nogueira, H.I.S., Adduce, C., Alves, E. and Franca, M.J. (2011). Analysis of the entrainment on lock-exchange density currents. *Geophysical Research Abstracts* 13(7011), EGU General Assembly, Vienna (Chapter 4).

◊ Nogueira, H.I.S., Adduce, C., Alves, E. and Franca, M.J. (2010). Evaluation of time-space varying density distribution on gravity currents by image analysis technique. *Proc. XVIII A.I.VE.LA. National Meeting & Exhibition*, Rome, Italy, 15-16 December (Section 2.3 and Chapter 3).

1.6 Thesis structure

The thesis is organized in six chapters and two appendices. In this chapter, an introduction to gravity currents was provided, being presented the main motivation and objectives of this research. The main contributions to date on gravity currents, in the specific topics covered by this thesis, were presented as well as a theoretical framework.

Chapter 2 is devoted to the experimental details, where the laboratory setup, measuring equipment and experimental procedure are presented for the two types of measurements performed.

The experimental variables and parameters are here summarized for all the experimental runs. The details, and preliminary results, of the new image analysis technique developed to assess the inner structure of gravity currents are presented in Section 2.3, based on the paper Nogueira *et al.* (2013c) and on the preliminary results presented in Nogueira *et al.* (2010).

In Chapter 3 the kinematics of the gravity current front are discussed based on the results obtained through the image analysis technique. The influence of the initial density of the saline mixture in the lock and of the bed roughness on the current front velocity and density are explored. A Froude number analysis based on different characteristic variables assessed at the head is here presented. This chapter is based on the paper Nogueira *et al.* (2013a) and on the preliminary results presented in Nogueira *et al.* (2010, 2011b) and Nogueira (2011), with additional details regarding the current depth-averaged density.

Chapter 4 complements the results presented in Chapter 3 with entrainment estimation and the analysis of the dynamics of the front of unsteady gravity currents, being presented both bulk and local approaches for entrainment estimation. The cyclic behavior observed at the current head is here characterized and related to local variables. This chapter is based on the paper Nogueira *et al.* (2013b) and on the preliminary results presented in Nogueira *et al.* (2011a, 2012a,b,c, 2013e).

Chapter 5 presents the main results arising from the velocity measurements with Particle Image Velocimetry. The influence of the bed roughness on the velocity, vorticity and turbulence fields is investigated. This chapter is based on the paper Nogueira *et al.* (2013d) and on the preliminary results presented in Nogueira *et al.* (2012d).

Since this thesis is mainly based on papers, the document was organized to avoid repetitions of content between sections of different chapters. Therefore, sections of introduction and experimental setup were simplified, and sections of acknowledgments, notation and bibliography were compiled into separate chapters.

In Chapter 6 the main conclusions of the present research are drawn and suggestions and recommendations for future works are given.

Two appendices are included at the end of the thesis, complementing the information presented in Chapter 5. Appendix A gives additional details on the filtering procedure applied to the temporal series of velocity, whereas Appendix B explains the criterion used to isolate the quasi-steady regions identified and analyzed in Chapter 5.

Chapter 2

EXPERIMENTAL DETAILS

Contents

2.1 Introduction

In this chapter the experimental details for the lock-exchange experiments performed to assess both density and velocity fields of unsteady gravity currents are provided. The experimental apparatus and the preliminary experiment preparation are common to both types of measurements and are described in subchapter 2.2, including the experimental variables and main parameters of the runs. Density measurements and the image analysis technique applied to assess the density field are described in subchapter 2.3, whereas subchapter 2.4 is devoted to velocity measurements with the PIV technique.

2.2 Apparatus and experimental procedure

2.2.1 Experimental setup

The experiments were performed at the Hydraulics Laboratory of University "Roma Tre", in a 3.0 m long Perspex tank with rectangular cross-section, 0.2 m wide and 0.3 m deep, as represented in Figures 2.1 and 2.2. The walls are transparent allowing the visualization of the gravity current development; the tank bed is smooth and is kept horizontal for the duration of the experiments. The bed roughness is one of the experimental variables being investigated, therefore a layer of roughness material was placed throughout the tank bed to confer a rough boundary in selected runs, as described further in the text.

The lock-exchange technique consists in having two fixed volumes of fluid with different densities, ρ_{c_0} and ρ_{a_0}, separated by a vertical partition (cf. Figure 2.2). A Perspex sliding gate, with the dimensions of the tank cross-section, is placed inside the tank dividing it in two sections of different volumes. The section with smaller volume, herein referred as "lock", is filled with a

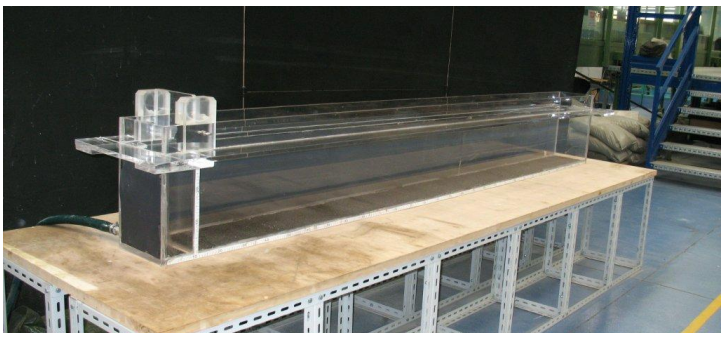

Figure 2.1: Perspex tank in a perspective view

saline mixture with density ρ_{c_0} up to a depth of h_0, whereas the remaining section is filled with fresh water, with density ρ_{a_0}, up to a depth of H (cf. Figure 2.2). The streamwise position of the gate is kept constant for all runs, at a distance from the left wall of x_0. In the runs performed over smooth bed, the bottom of the tank is the reference level used to measure the initial depth of both fluids and the gravity current height, while in the runs over rough bed the top of the bed crests was used as reference level. Full-depth lock-exchange flows are the case under analysis, where the fluids in both sections of the tank have the same depth, $\varphi = h_0/H = 1$.

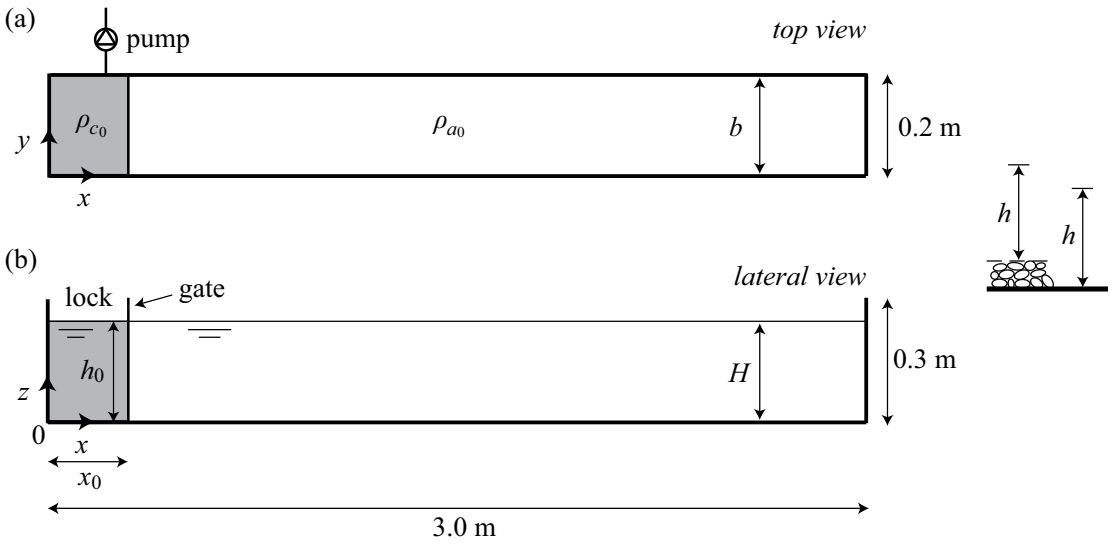

Figure 2.2: Schematic views of the Perspex tank aimed at the lock-exchange experiments with main dimensions and the Cartesian reference system herein considered

2.2.2 Sediment bed

Roughness material mainly composed by quartz and feldspar minerals were manually placed throughout the tank bed, forming a layer with thickness of around $3D_{50}$, where D_{50} is the median grain diameter, i.e., the grain size for which 50 % of the particles, by weight, have a smaller diameter. Herein, D_{50} is taken as the roughness scale k_s. The bed material was set uniformly all over the tank bed, (Figure 2.3), where no bed forms were allowed. During the experiments no erosion of the bed material was observed.

Three sets of materials with different grain size distributions were used, one for each experimental run, with the granulometric curves presented in Figure 2.4 and the characteristic diameters summarized in Table 2.1, where D_{10}, D_{30} and D_{60} represent the diameters for which 10, 30 and 60 % of the material have smaller diameters, respectively. Table 2.1 also presents the coefficients

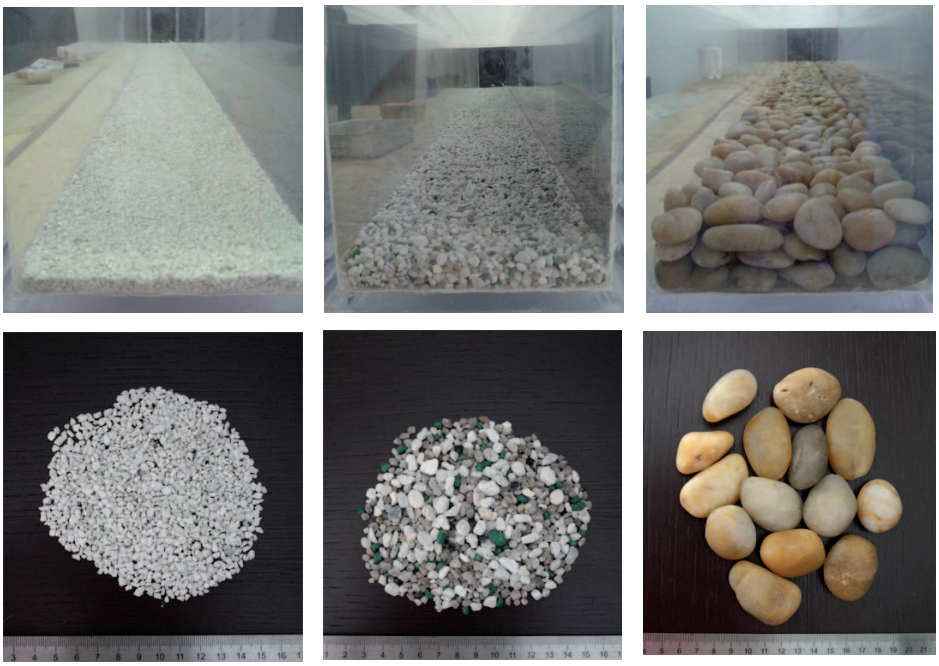

R1 R2 R3

Figure 2.3: Details of the rough beds used for runs of type R: R1, D_{50} = 2.9 mm (left), R2, D_{50} = 4.6 mm (centre) and R3, D_{50} = 24.6 mm (right). View of the tank bed from the downstream section, i.e., right end wall (top); sediment samples (bottom)

of uniformity, C_u, and curvature, C_c, for the bed material, given as

$$C_u = \frac{D_{60}}{D_{10}} \tag{2.1}$$

$$C_c = \frac{D_{30}^2}{D_{10} \times D_{60}} \tag{2.2}$$

Based on the ASTM unified classification system (cf. King and Galvin 2002), the two sets of materials with smaller mean diameter, used in runs R1 and R2, are classified as coarse sand while the sediments with larger diameter, in run R3, correspond to a coarse gravel (for a complete description of the runs see subsection 2.2.4).

Table 2.1: Characteristics of the bed material used in runs of type R

Run	D_{10} (mm)	D_{30} (mm)	D_{50} (mm)	D_{60} (mm)	C_u	C_c
R1	1.6	2.4	2.9	3.2	2.1	1.1
R2	2.7	3.5	4.6	5.2	2.0	0.9
R3	19.8	22.1	24.6	26.6	1.3	0.9

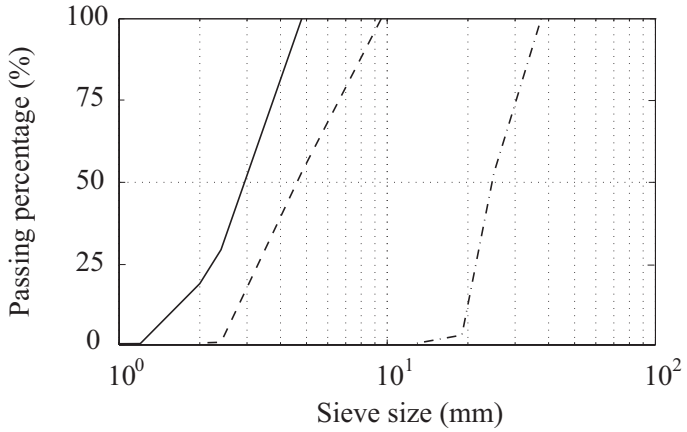

Figure 2.4: Distribution of the grain diameters of the bed material used in runs R1 (solid), R2 (dashed) and R3 (dashed-dot)

2.2.3 Experimental procedures

Before filling each part of the tank, the contact zones between the gate and the tank walls were sealed with petroleum jelly to avoid fluid leaking between tank sections (cf. Figure 2.5). Two rulers are placed in the sidewall of the tank, in both vertical and horizontal directions, for geometric calibration purposes.

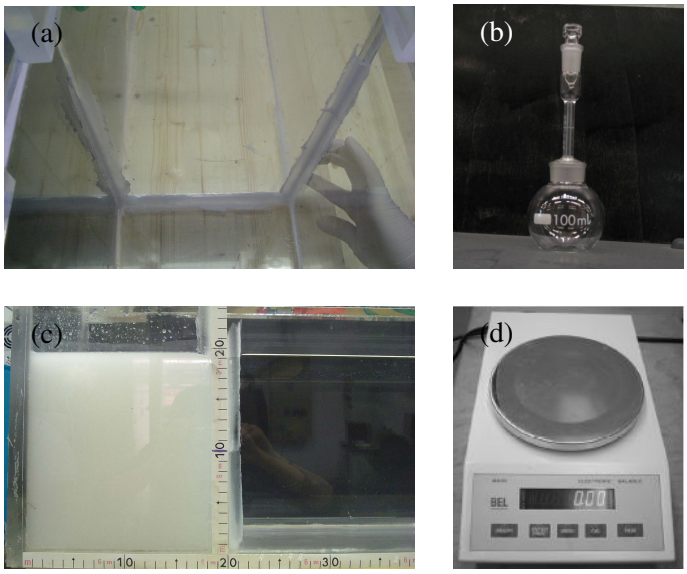

Figure 2.5: Details of the experiment preparation and equipment used to measure the initial density of the saline mixture. Top: placement of the sealing material (a); pycnometer (b). Bottom: detail of the lock after filling both tank sections (c); weighing apparatus (d)

The saline mixture was prepared as follows: for a selected density of the mixture, ρ_{c_0}, the

amount of salt, m_s, was estimated by

$$m_s = V_{c_0} \frac{\rho_{c_0} - \rho_{a_0}}{1 - \frac{\rho_{a_0}}{\rho_s}} \tag{2.3}$$

where V_{c_0} is the volume of the mixture of density ρ_{c_0} and ρ_s is the salt density, here considered as $\rho_s = 3450$ kg·m^{-3} for fine table salt. The density of the mixture is then checked through a pycnometer (Figure 2.5) with filling volume of 100 ml. Three samples of the saline mixture are weighted and taken the average density value, which is then compared to the value of the selected density. If the relative error exceeds 0.05 %, adjustments are then made by adding water or salt to the mixture, until reaching an acceped error.

The density of the ambient fluid was also determined in the beginning of each run by measuring the temperature of the water added in the tank, in three random locations, and by using the following relation proposed by Tanaka *et al.* (2001) for the density of water, ρ_{a_0}, as function of temperature, Θ, given as

$$\rho_{a_0} = \alpha_5 \left(1 - \frac{(\Theta + \alpha_1)^2 (\Theta + \alpha_2)}{\alpha_3 (\Theta + \alpha_4)} \right) \tag{2.4}$$

where α_i are the best fit parameters obtained by the least-squares method, with the values presented in Table 2.2. The density difference between fluids is a result of both temperature and salt concentration.

Table 2.2: Parameters of the expression (2.4) relating the density to the temperature of water (Tanaka *et al.* 2001)

Parameter	Value
α_1	-3.983035
α_2	301.797
α_3	522528.9
α_4	69.34881
α_5	999.974950

Both fluids are initially at rest and the experiment starts when the gate is manually removed, as fast as possible. The difference in pressure between fluids leads to the collapse of the vertical column of heavier fluid, being then accelerated along the bottom of the tank in the downstream direction (to the right), while the light fluid is accelerated towards upstream (to the left), above the dense current. Figure 2.6 shows a sequence of snapshots of the phenomenon, with the dense grav-

ity current developing over a rough bed (run R2). During this process, mixing between both fluids takes place, inducing entrainment of ambient fluid into the dense current, reducing its density. The experiment ends when the dense current reaches the right end wall of the tank. At the end of a run, the fluid within the tank is removed by a pump, connected to a hole in the back sidewall of the tank (Figure 2.2), being the walls and the bed cleaned to remove sediments, colorant or seeding particles, depending on the type of experiment performed.

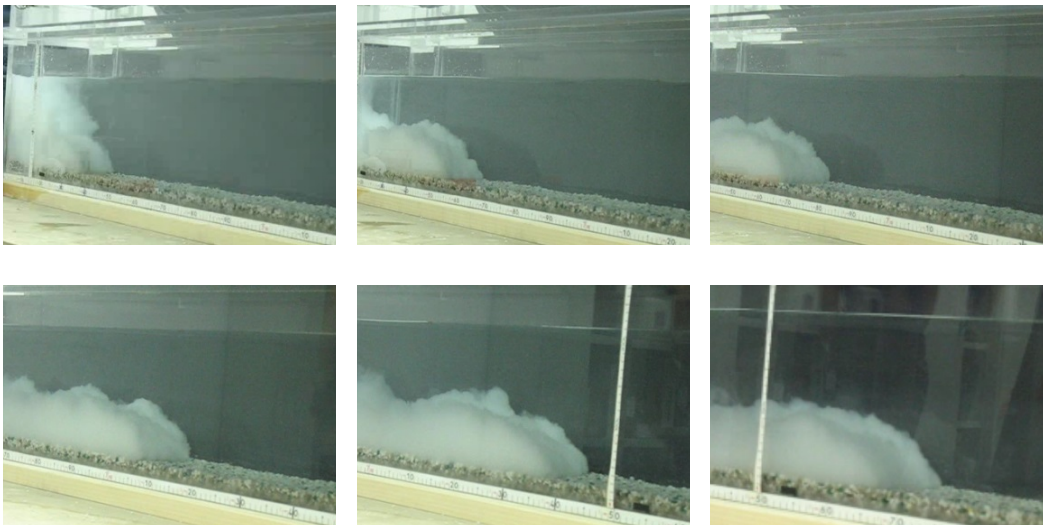

Figure 2.6: Snapshots with the gravity current development over rough bed (run R2)

2.2.4 Experimental parameters

Two types of experiments were performed to assess the density and the velocity fields independently. In the density experiments, seven runs were performed by varying the initial density of the saline mixture in the lock, ρ_{c_0}, and the bed roughness, k_s, leading to two different sets of runs, designated as "D" (density) and "R" (roughness), respectively. The experiments were performed by varying one parameter at a time. For velocity measurement purposes, four experiments were performed by changing the bed roughness, k_s, maintaining constant all other variables. The initial depth of both ambient fluid and saline mixture are kept constant among runs and equal to $h_0 = H = 0.20$ m; the lock length is kept at $x_0 = 0.15$ m for all runs. Table 2.3 summarizes the parameters of all lock-exchange experiments and the symbols used later in the figures presenting the results.

Each run was performed with an initial reduced gravity of the mixture in the lock, defined as

$$g'_0 = g\frac{\rho_{c_0} - \rho_{a_0}}{\rho_{a_0}} \tag{2.5}$$

being g the acceleration of gravity.

The main parameters are presented in the non-dimensional form by adopting the following dimensionally independent scales, in accordance with previous studies (Hacker *et al.* 1996, Marino *et al.* 2005, Ungarish and Zemach 2005): lock length x_0 as the streamwise length scale, h_0 as the vertical length scale and a velocity scale given by the buoyancy velocity defined as

$$u_0 = \sqrt{g'_0 h_0} \tag{2.6}$$

Reynolds number based on initial quantities is given by

$$Re_0 = \frac{u_0 h_0}{\nu_c} \tag{2.7}$$

where ν_c is the kinematic viscosity of the saline mixture, being a function of temperature, pressure and concentration of salt, and is herein obtained through the results presented in Kestin *et al.* (1981). Values of the initial Reynolds number show the turbulent nature of the gravity currents performed since $Re_0 > 35000$ (cf. Table 2.3).

Bulk quantities of the current were estimated for the assessment of overall entrainment of ambient fluid into the denser current. Densimetric Froude, Fr_b, and Reynolds, Re_b, numbers based on bulk quantities are defined as:

$$Fr_b = \frac{\bar{u}_f}{\sqrt{g\Delta\bar{\rho}/\rho_{a_0} h_b}} \tag{2.8}$$

$$Re_b = \frac{\bar{u}_f h_b}{\nu_a} \tag{2.9}$$

where $\bar{u}_f$ is the bulk front velocity of the denser current, obtained by taking the initial and final positions of the current front and the duration of the experiment, $\Delta\bar{\rho} = \bar{\rho}_{end} - \rho_0$, with $\bar{\rho}_{end}$ being the mean density of the gravity current in its final configuration, i.e., when it reaches the end of the tank, and h_b the bulk height of the current, taken as $h_b \approx 1/3 h_0$ based on the results presented further in the text.

Table 2.3: Main parameters of the lock-exchange experiments performed

Type	Run	ρ_{a_0} (kg·m^{-3})	ρ_{c_0} (kg·m^{-3})	$\Delta\rho$ (kg·m^{-3})	k_s (mm)	g'_0 (m·s^{-2})	u_0 (m·s^{-1})	$\bar{u}_f$ (m·s^{-1})	Δu (m·s^{-1})	Re_0	Re_b	Fr_b	Symbols in figures
Density	D1	997.8	1014.7	16.9	0.0	0.17	0.18	0.06	0.09	40756	3872	1.31	○
	D2	997.4	1029.7	32.3	0.0	0.32	0.25	0.09	0.13	53230	5716	1.31	□
	D3	997.4	1044.6	47.2	0.0	0.46	0.30	0.11	0.16	66918	7237	1.55	△
	D4	998.0	1060.0	62.0	0.0	0.61	0.35	0.12	0.19	64680	8244	1.66	▽
	R1	997.4	1030.0	32.6	2.9	0.32	0.25	0.08	0.13	64922	5647	1.59	+
	R2	997.4	1030.1	32.7	4.6	0.32	0.25	0.08	0.12	55058	5283	1.54	×
	R3	997.6	1030.2	32.6	24.6	0.32	0.25	0.07	0.10	52479	4385	0.89	*
Velocity	R0	998.5	1015.2	16.6	0.0	0.16	0.18	-	-	40156	-	-	○
	R1	998.6	1015.5	16.9	2.9	0.17	0.18	-	-	40412	-	-	□
	R2	998.0	1015.3	16.4	4.6	0.16	0.18	-	-	39674	-	-	△
	R3	999.1	1014.9	15.9	24.6	0.16	0.18	-	-	36976	-	-	▽

In full depth lock-release flows, the return current, propagating above the denser current in the opposite direction, has non-negligible velocity. The difference between mean front velocities of both denser and return currents, Δu (cf. Table 2.3), is obtained considering the bulk height of the denser current, $\bar{h}$, and by mass conservation considerations, resulting in $\Delta u \approx 1.5\bar{u}_f$.

2.3 Density measurements

2.3.1 Introduction

This subchapter (2.3) is based on the technical design note 'Image analysis technique applied to lock-exchange gravity currents' published in *Measurement Science and Technology (IOP), 24*(047001), in 2013, by the authors H.I.S. Nogueira, C. Adduce, E. Alves and M.J. Franca.

An image analysis technique was applied to assess the instantaneous two-dimensional density field within the gravity current. Using dye concentration as a tracer, a calibration procedure was established for each pixel in the image relating the amount of dye uniformly distributed in the tank and the greyscale values in the corresponding images. The results are evaluated and corrected by applying the mass conservation principle within the experimental tank. The procedure is a simple way to assess the time-varying density distribution within the gravity current, allowing the investigation of gravity current dynamics and mixing processes.

2.3.2 Image analysis technique

A CCD camera with 768 × 576 pixels of resolution and acquisition frequency of 25 Hz, was used to record the current evolution, being kept at a fixed perpendicular position from the sidewalls of the tank. The camera was aligned with the center of the tank and placed at a sufficient distance to capture its entire length, as shown in Figure 2.7.

The experimental tank was placed in a room where the source of light could be controlled. The illumination is made by means of fluorescent ceiling light, being the upper part of the tank covered with a thin black painted wooden board, to avoid reflection of light from the water surface. A controlled quantity of white colorant (E171, titanium dioxide) is added to the saline mixture in the lock to provide flow visualization and for density assessment purposes. High contrast between the current and its background is achieved through the placement of black paperboard in the back sidewall of the tank, producing a dark, uniform background (Figure 2.7).

The captured video frames with the current development are subsequently converted into greyscale matrices, in the region of the tank with fluid (702 × 43 pixels) and then converted into instantaneous density fields of the current through a calibration procedure described further in the text. Results are shown for a selected window of the field of view (dashed white rectangle in Figure 2.7). Density values so obtained give an estimation of the width-average density of the current, for each pixel of the region of analysis and for each instant.

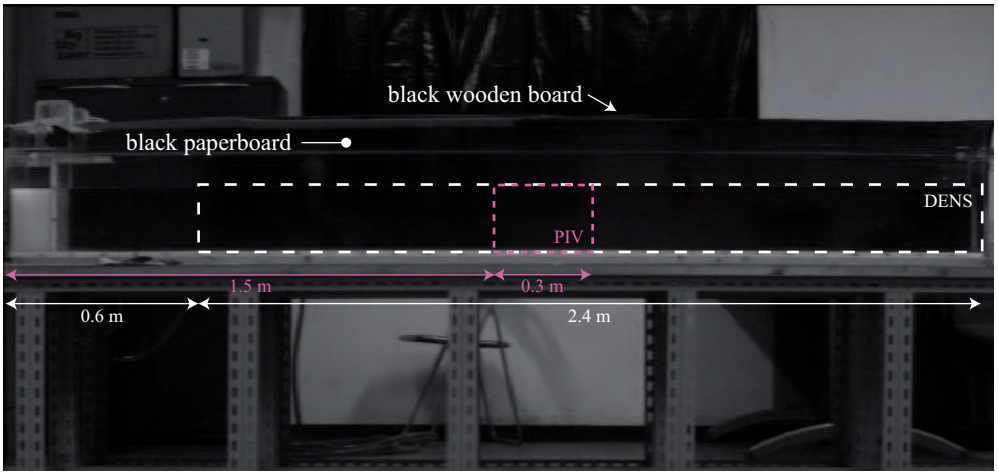

Figure 2.7: Picture representing the windows of the flow field used for data analysis. White dashed rectangle represents the location of the region analyzed in the density experiments, whereas the pink dashed rectangle represents the region captured during velocity measurements with PIV

2.3.3 Calibration method

The evaluation of the current density distribution is based on a relation between reflected light intensity and concentration of dye present in the flow; this latter is considered linearly correlated with salt concentration within the current body. A calibration procedure was carried out for each single pixel in the region defined earlier, leading to $702 \times 43 = 30186$ calibration curves, relating the amount of dye in the water and the values of greyscale in the frames representing light intensities. A pixel-by-pixel calibration avoids the errors induced by assuming uniform light and background conditions in the region of analysis. Eight known dye quantities, increasingly from zero to a maximum value corresponding to ρ_1, were uniformly distributed through the tank being the corresponding images captured for calibration for the very same light conditions and distance between camera and tank as during the experiments. Assuming a direct relation between the amount of dye and density of the current, it is thus possible to infer density values at any given pixel and at any given instant from its instantaneous greyscale value. A cubic interpolation applied to each pixel individual calibration curve allows the conversion, in a continuous way, of the greyscale values into density. Figure 2.8 shows a calibration curve for one single pixel in the center of the image, whose location is illustrated with a white dot in the presented frames, where greyscale values increase nonlinearly with the amount of dye in the flow.

Figure 2.8: Example of images used for calibration and corresponding calibration curve. The reference point corresponds to one central pixel of the image and is represented in the frames by white dots

Oscillations in the intensity of the ambient light were detected when analyzing the temporal series of greyscale values in each pixel of a selected region in the acquired frames. Both "dark" (low greyscale values) and "white" (high greyscale values) regions were analyzed and compared the deviations from the temporal mean of greyscale values, in each pixel. Average deviations are higher in "dark" regions (8 %), which corresponds to a deviation of 0.5 % in terms of density. "White" regions show lower average deviations from the mean (1.3 %) but in terms of density the

deviation is more relevant (6 %), once the calibration curves (Figure 2.8) are of exponential type, in which density grows with the increase of greyscale values. These deviations are overall corrected when applying the mass conservation principle to the entire experimental tank, accounting thus with the current mass and the mass of ambient fluid. This correction covers overall experimental and data treatment errors and it proves to be of the order of magnitude of 0.1 %, i.e., the relative deviation between the total mass in the tank, considering the amount of water (m_a) and salt (m_s) introduced in the tank in the beginning of the experiment ($m_a + m_s$), and the total mass evaluated experimentally $b\Big(\int_{V_{c(t)}} \rho_c(x,z,t)\mathrm{d}V + \int_{V_{a(t)}} \rho_a \mathrm{d}V\Big)$, where b is the width of the tank, $\rho_c(x,z,t)$ is the local density of the current, being t the time after gate removal, V_c and V_a volumes of the gravity current and the ambient fluid per unit width of the tank, respectively, and V volume considered per unit width of the tank.

2.3.4 Density maps

Figure 2.9 shows the development of the current captured at instants t = 20, 28 and 36 s after the gate removal in run D1 (see Table 2.3) and the corresponding reconstructed non-dimensional instantaneous iso-density contours plotted for 0.02, 0.15, 0.30 and 0.50, being the non-dimensional density defined as $\rho^*(x,z,t) = (\rho_c(x,z,t) - \rho_{a_0})/(\rho_{c_0} - \rho_{a_0})$, where $\rho_c(x,z,t)$ is the local density of the current.

In general, three regions within the current can be distinguished: near-bed region where bed drag exerts influence mainly on momentum transfer related processes, central region where velocity is expected to be maximum and little mass and momentum transfer processes are verified and interfacial shear layer, the main region for mass and momentum transfer (Legg 2012). A preliminary assessment of the density fields shows that mixing processes are not confined to the boundary between current and ambient fluid, they rather extend through the entire depth of the current. Figure 2.9 shows that the head is the region where higher density is observed, which is in accordance with previous observations (Hacker *et al.* 1996, Hallworth *et al.* 1996, Marino *et al.* 2005). The evolution of the current front position and velocity and the transition between first and second phases of the current development (cf. Chapter 3) are comparable to previous observations in currents with similar characteristics (Rottman and Simpson 1983, Marino *et al.* 2005, Adduce *et al.* 2012). Furthermore, the analysis of the temporal evolution of the dimensions and mass of the head of these currents shows interesting cycles of head stretching and breaking throughout the gravity current development (cf. Chapter 4 and Nogueira *et al.* 2012b), being the breaking events

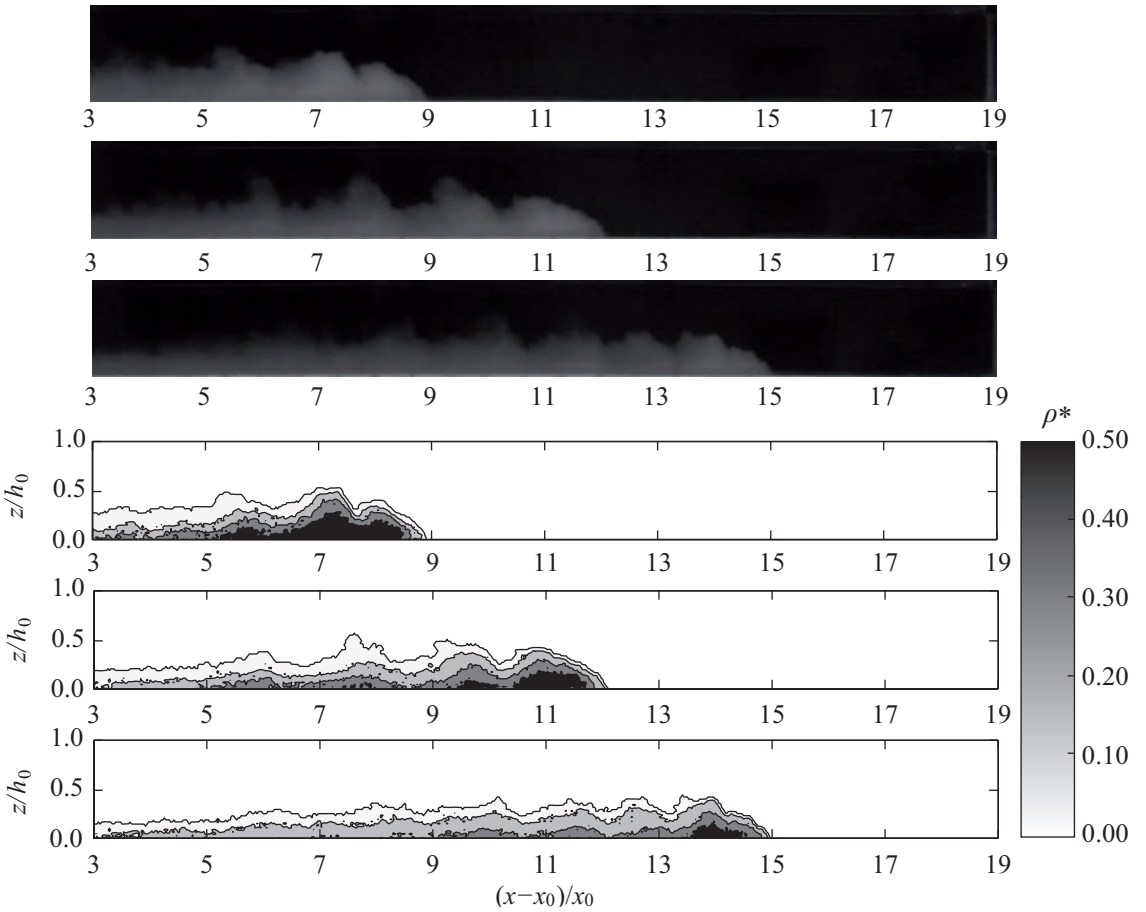

Figure 2.9: (top) Photos of the current acquired at t = 20, 28 and 36 s after the gate removal; (bottom) corresponding non-dimensional iso-density contours plotted at ρ^* = 0.02, 0.15, 0.30 and 0.50.

followed by the formation of large-scale billow structures at the rear of the gravity current head, which eventually fade in time by diffusion-type processes. This is visible in Figure 2.9, following the evolution of the billow structure at positions $(x - x_0)/x_0$ = 7.0, 8.0 and 8.5 (at t = 20, 28 and 36 s, respectively).

2.4 Velocity measurements

2.4.1 Introduction

The Particle Image Velocimetry (PIV) technique was used to measure the instantaneous two-dimensional flow velocity field. This is an non-intrusive technique that provides the spatial distribution of the velocity field based on the displacement of tracer seeding particles. The main components of the PIV system include a light source, i.e., a laser with one or two cavities for

single or double laser pulses, optics to transform the laser beam into a light sheet to illuminate a given two-dimensional section of the flow, a CCD camera synchronized with the laser to capture the illuminated flow region and an appropriate software to control the laser properties, data acquisition and treatment process (Raffel *et al.* 2007).

2.4.2 PIV principle

The PIV system consisted on a double laser pulse, illuminating the flow field at two successive instants, t_1 and $t_1 + \Delta t$, respectively, being acquired the corresponding frames with the illuminated seeding particles. These frames are then split into a grid of interrogation areas where a cross-correlation function is applied, allowing the estimation of the most likely particle displacement within each interrogation area. Dividing the particle displacement by the time between laser pulses, Δt, a velocity vector is thus obtained. This procedure is then applied to all the interrogation areas in the frame leading to a two-dimensional flow velocity map, which will then be validated and optimized.

The quality of PIV data acquisition is controlled by the relation between the time between pulses, the size of the interrogation areas and the size and amount of seeding particles. For a given flow velocity, the time between laser pulses should be long enough to detect the particles displacement among successive frames and short enough to avoid particles to leave the light sheet between frames. The size of the interrogation areas define the spatial resolution of the velocity measurements and depend on the time between pulses and on the amount of particles within the flow. A limit of 9 particles per interrogation area is usually enough for good velocity measurements, whereas a maximum particle displacement of 25 % in each interrogation area should be verified. Each of these parameters are selected and optimized after several tests by analyzing the acquired image pairs.

Each PIV image pair results in a raw velocity map after applying a cross-correlation. The velocity map includes valid vectors and a certain percentage of outliers, i.e., erroneous vectors resulting, for instance, from inhomogeneous seeding distribution, loss of particles between frames or in areas where the light sheet is shadowed. Even in optimized PIV images analyzed with appropriate parameters, a certain percentage of outliers is obtained. These are removed through global and local filtering operations, where the magnitude of each velocity component is compared with the mean value obtained for the entire velocity map and with mean value of the nearest neighbor vectors, respectively. Outliers are then substituted by interpolation of the valid neighbor

vectors, based on a weighted mean technique. An adaptive cross-correlation is then applied to improve the spatial discretization of the velocity field. The resulting vectors are again filtered and smooth, leading to the final velocity map of the flow.

2.4.3 PIV technique

The laser source of the PIV system (ILA - Intelligent Laser Applications GmbH®) was placed at the right end wall of the tank (cf. Figure 2.10), the laser sheet being adjusted to illuminate the vertical plane in the centerline of the tank. The laser is double pulsed (Nd:YAG laser, 532 nm green) and the image pairs were acquired at 3 Hz with an interval of 30 ms between pulses. Both saline mixture and ambient fluid were seeded with polyamide tracer particles with 100 μm of mean diameter and mean density of 1016 kg·m^{-3}. This is an appropriate density to trace the saline fluid, being nevertheless higher than the density of the ambient fluid. We assume the effect of this density difference (ambient fluid/particles) to be negligible for the short duration of the experiments (longest run lasts $\approx$ 80 s) and for the small amount of particles introduced in the tank.

A CCD camera (PCO Pixelfly^{TM} double shutter with 1392 $\times$ 1024 pixels of resolution) was kept at a fixed perpendicular position to the sidewall, capturing a window of the flow of 0.30 m long and 0.18 m deep, starting from x = 1.50 m, as shown schematically in Figure 2.10. To improve the quality of the acquired images, a black paperboard was placed in the back wall of the tank, producing a dark uniform background, and the room where the experiments were performed

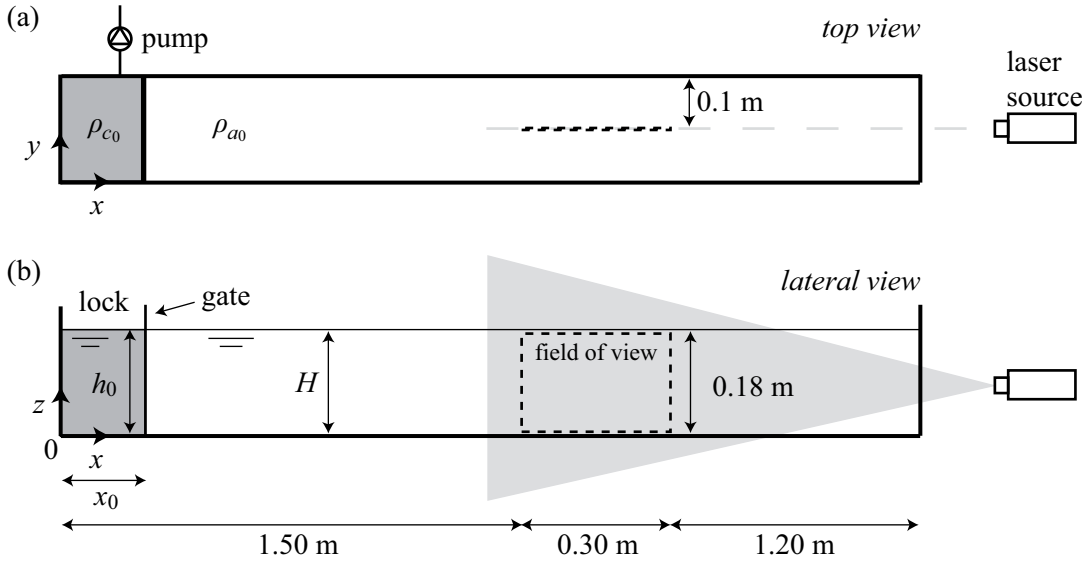

Figure 2.10: Schematic view of the Perspex tank with main dimensions and main elements for the velocity measurement setup

was made as dark as possible. In the experiments with rough bed, the grains located on the top of the sediment layer and in the visualization region, were previously painted with black spray to reduce the reflection of the incident laser light, allowing velocity measurements near the flow bed. Before starting each run, a perspex plate with a graduated square grid was placed in the tank centerline for calibration and camera focus purposes, as illustrated in Figure. 2.11

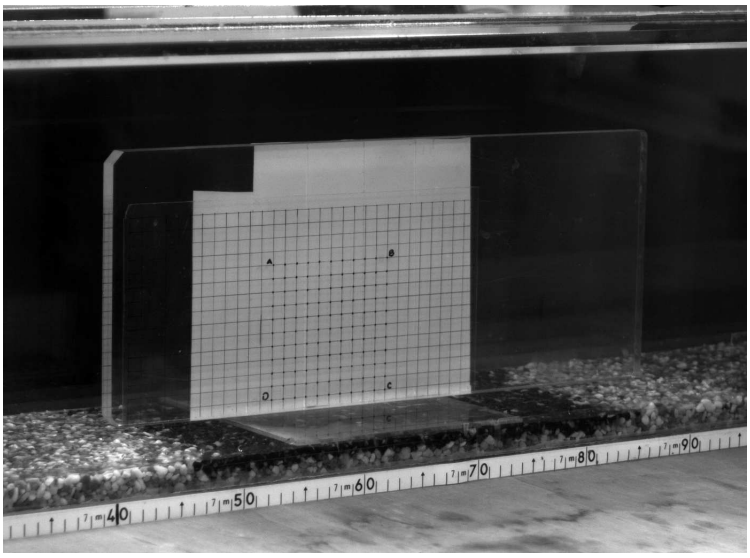

Figure 2.11: Grid used for camera focus and for geometric calibration of the captured field of view

The laser starts firing, synchronized with the CCD camera, before removing the lock gate to ensure that the measurements are being performed when the current enters the visualization window. The zero time reference is associated to the gate removal.

Velocity measurements with PIV intend to complement the analysis based on the density information provided by the image analysis technique presented in subchapter 2.3. Experiments therein described were performed with an excess density, $\Delta\rho$, in the range 17 to 63 kg·m^{-3}. One of the difficulties of using PIV to measure the velocity field of gravity currents is that both brine and ambient fluid have different refractive indices and, as a consequence, the direction of the incident laser sheet is deviated when crossing the interface of both fluids. This causes blurry PIV images where individual particles are difficult to distinguish (cf. top images in Figure 2.12). This was confirmed by our experiments and only with the lowest excess density tested, 17 kg·m^{-3}, the particles had a sufficient definition for velocity measurement purposes, as shown by the PIV images in Figure 2.12 (bottom), where individual seeding particles can be distinguished. It was thus decided to reproduce saline currents with comparably low excess density, avoiding the need to use refractive index matching techniques, which would change other properties of the intervening

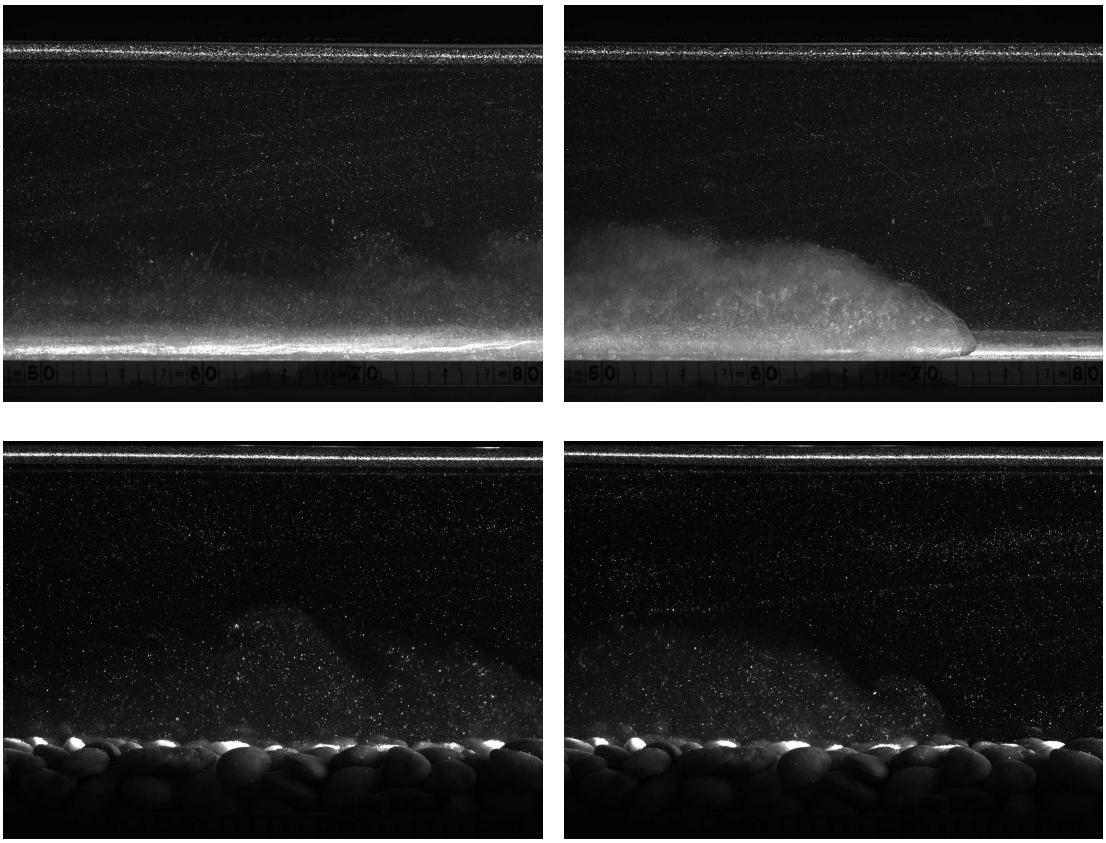

Figure 2.12: Frames capturing two gravity currents performed with initial density $\rho_{c_0} = 1029.6$ kg·m^{-3} (top) and $\rho_{c_0} = 1014.9$ kg·m^{-3} (bottom)

fluids such as viscosity.

The software VidPIV (version 4.6) was used to control the image acquisition parameters, image processing and data analysis. In the application of the cross-correlation method, the interrogation areas had a size of 64 × 64 pixels with 50 % overlap, reduced to 32 × 32 pixels in the adaptive correlation. Both global and local filtering procedures were applied to the velocity maps obtained after image correlation. The global filter identifies the globally inconsistent vectors for the whole velocity map while the local filter compares each vector only with the nearest neighbors. Filter boundaries were defined based on a trial and error procedure, resulting in an approximate 4 x 4 mm^2 final grid of two-dimensional (vertical and streamwise) instantaneous velocity vectors. An example of the velocity field is given in Figure 2.13, where the velocity magnitude is superimposed by the velocity vectors, for an instant in run R3, $t = 28$ s after the gate removal, where the current is entering the visualization window.

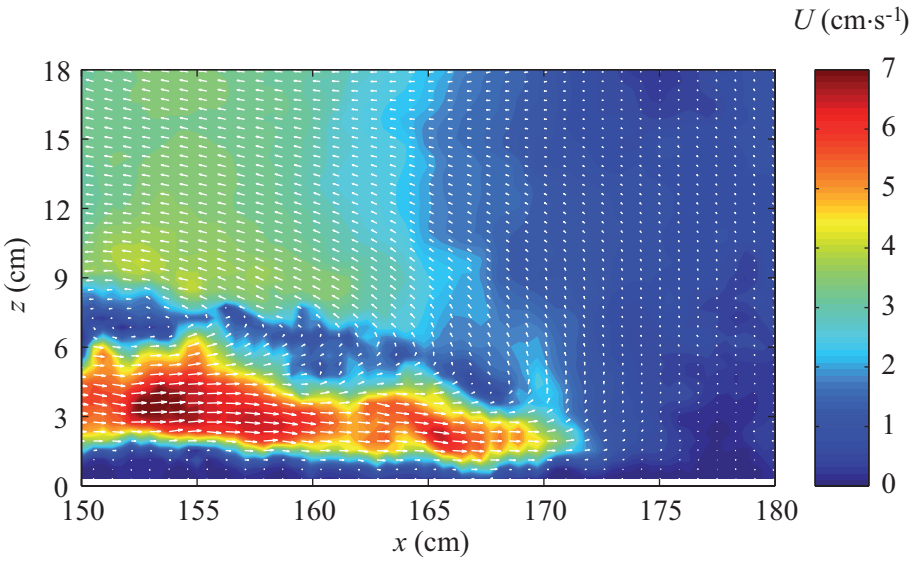

Figure 2.13: Velocity map obtained for run R3 at $t = 28$ s after the gate removal. Map with the velocity magnitude, U, superimposed by the velocity vectors.

Chapter 3

CHARACTERIZATION OF GRAVITY CURRENTS BASED ON DENSITY MEASUREMENTS

Contents

Chapter 3 is based on the paper 'Analysis of lock-exchange gravity currents over smooth and rough beds', published as a research paper in Journal of Hydraulic Research, volume 51(4), 2013, by the authors H.I.S. Nogueira, C. Adduce, E. Alves and M.J. Franca, and based on the preliminary results presented in Nogueira et al. *(2010, 2011b) and Nogueira (2011). It deals with the main kinematic features observed in the lock-released gravity currents, arising from an image analysis technique applied to assess the inner density field. The influence of the initial excess density and of the bed roughness in the front velocity, current height and depth-averaged density is herein discussed. Further results on the vertical distribution of density, not included in Nogueira* et al. *(2013a), are herein provided.*

Abstract

Gravity currents produced by full-depth lock-release of saline water into a fresh water tank are studied focusing on the influence of the initial density of the saline mixture in the lock and the bed roughness on gravity current kinematics. Temporal evolution of the current front position and front velocity are analyzed and related to different phases of the current. Time-space evolution of current depth-averaged density and current height are assessed as well. Vertical density profiles show the effect of the bed roughness. Density profiles obtained at the current head show strong similarity among runs when normalized with adequate flow variables. Roughness of the tank bed plays an important role in the current kinematics, particularly in decreasing the front velocity due to extra drag at the bed. The analysis of Froude numbers, estimated with the initial and local reduced gravity and established with different length scales of the current, allow for the definition of the important variables and current dynamics of each phase of the current development.

3.1 Introduction

Gravity currents have been studied extensively in the laboratory through lock-exchange experiments (Huppert and Simpson 1980, Rottman and Simpson 1983, Altinakar 1993, Hallworth *et al.* 1996, Zhu *et al.* 2006), which consist of the instantaneous release of a fixed volume of dense fluid into another fluid of slightly lower density. The differences in hydrostatic pressure between fluids cause the denser fluid to flow along the bottom boundary of the channel, while the lighter fluid flows along the top boundary, in the opposite direction. The development of gravity currents is typically an unsteady phenomenon, i.e., current kinematics and inner density distribution are time

varying. Therefore, the lock-exchange setup is a simple and convenient way to investigating the flow features of these particular currents. Although the motion of these currents is invariably three-dimensional, laboratorial experiments and numerical results indicate that the large-scale features may be reasonably well described through a two-dimensional approach (Härtel *et al.* 2000).

Few investigators have studied the effect of bed roughness in the dynamics of gravity currents. Peters and Venart (2000) investigated the flow dynamics and mixing processes at the head region of gravity currents developing over rough surfaces through LIF measurements. Regular square cross section elements were used to reproduce bed roughness, spanning the full channel width, with four different side dimensions. In general, they observed that roughness decreases the front velocity and induces higher dilution in the head region. According to these authors, those effects are due to two mechanisms: an increase in bed roughness induces extra bed shear stress, extra flow resistance and viscous effects; additionally, ambient fluid trapped within the roughness layer is entrained into the current, contributing to a reduction of the buoyancy differences between current and ambient fluid which constitutes the flow driving force. In La Rocca *et al.* (2008) three-dimensional gravity currents were produced by varying the initial density of the mixture in the lock and the bed roughness of the tank, testing four mean diameters within a range of 0.7 mm to 3.0 mm in a thin layer glued to the bed. The front velocity was seen to decrease with the increase of the mean diameter of the roughness elements, this effect being more obvious in the second phase of the current development. The increase in the friction stress induced by roughness precedes the beginning of the current deceleration phase. Adduce *et al.* (2009) performed experiments with a rough bed using quartz sand. They used an image analysis technique to investigate current dynamics and confirmed the findings reported in both Peters and Venart (2000) and La Rocca *et al.* (2008) regarding roughness effects on front velocity reduction. The effect of bed roughness in the development of gravity currents, developing downslope in the ocean and important in ocean circulation, was numerically investigated by Özgökmen and Fischer (2008). The results of their simulations suggest that roughness enhances drag, with effects on the velocity field, and mixing between the current and ambient fluid modifying the density distribution within the current. Despite previous contributions, the effect of the bed roughness in the kinematics of gravity currents is far from being completely understood.

Gravity currents produced by the lock-exchange technique over a smooth bed present two, or even three, distinct phases: (i) a slumping phase develops after the sudden release of the heavy fluid into the ambient fluid, during which the front position varies linearly with time, i.e., the front

advances with approximately constant velocity (Huppert and Simpson 1980); (ii) a second phase, or self-similar phase, starts when a bore generated at the end wall of the channel overtakes the gravity current front (Rottman and Simpson 1983); from this instant, the front position advances as $t^{2/3}$, with front speed decreasing as $t^{-1/3}$, t being the time after the gate removal; (iii) third phase develops when viscous effects overcome inertial effects, and the current front velocity decreases more rapidly (as $t^{-4/5}$, with front position advancing as $t^{1/5}$).

In both slumping and self-similar phases, the current development is governed by the balance between buoyancy and inertial forces. Peters and Venart (2000) reported that viscous effects dominate the flow earlier in the presence of a rough bed, when compared to smooth bed experiments. Generally, buoyancy is the engine for gravity current propagation. Buoyancy forces are in turn counterbalanced by inertia as well as resistance due to Reynolds stresses and viscous drag, both acting at the upper and lower boundaries of the current.

The present work aims to (i) investigate the influence of the density of the fluid in the lock and of the bed roughness on the gravity current development and (ii) analyze characteristic variables for each phase of the current by comparing different kinematic scales, bulk and local (the latter characterizing the current head), for normalization of the front velocity. This research is based on experimental work where lock-exchange density currents, induced by salinity differences, are reproduced under controlled conditions in an open channel. The development of the saline currents is captured by a CCD camera, using dye concentration as a tracer, thus allowing for the reconstruction of time and space (2D) evolution of the density fields. The assessment of the density fields through the image analysis technique herein presented contains information supplementary to previous works on gravity currents, specifically the works by La Rocca *et al.* (2008), with gravity currents developing over rough beds, and Adduce *et al.* (2012), with gravity currents developing over smooth beds.

After this introduction, experimental setup is summarized in section 3.2, main results concerning flow visualization, front position and velocity, current height, depth-averaged density and vertical density profiles are presented and discussed in section 3.3 and section 3.4 is devoted to the main conclusions.

3.2 Experimental setup

The lock-release experiments were performed in the experimental tank (Figures 2.1 and 2.2) described in Chapter 2. The saline mixture with initial density ρ_1 was placed in a lock with a vertical sliding gate at a distance $x_0 = 0.15$ m from the left wall of the tank. The right side of the tank was filled with fresh water with density ρ_{a_0}, both sides filled up at same depth, $h_0 = 0.20$ m. In all experiments, the relative depth of the initial configuration was kept $\varphi = h_0/H = 1$, where $H = 0.20$ m is the total depth of the ambient fluid (cf. Figure 2.2). The preparation of the experiments is as described in subchapters 2.2 and 2.3. Variables between runs are the initial density of the saline mixture in the lock, ρ_{c_0}, and the bed roughness, k_s, the parameters of the experiments being summarized in Table 2.3 (runs Density).

An image analysis technique was applied to assess the density field, as described in Chapter 2.3. Results are herein shown for a selected window (dashed rectangle in Figure 2.7) of the field of view. The conversion of greyscale video images into density fields is illustrated by Figure 2.9 which shows the development of the current captured at instants $t = 20$, 28 and 36 s after the gate removal in run D1 and the corresponding reconstructed non-dimensional instantaneous iso-density contours plotted for $\rho^* = 0.02, 0.15, 0.30$ and 0.50.

3.3 Results

3.3.1 Front position

The instantaneous front position $x_f(t)$ was estimated through the instantaneous density maps by taking the x-position of the foremost point of the current and by adopting the non-dimensional iso-density contour of 0.02 as the boundary of the current. The amplitude of the error of the front position corresponds to a half pixel (± 2 mm) in space and to half the camera sampling time (0.02 s) in time. Figure 3.1(a) shows the variation with time of the front position in terms of lock lengths, $(x_f - x_0)/x_0$, and Figure 3.1(b) the corresponding log-log plot for all runs including the regression curves found in literature for both slumping and self-similar phases.

Figure 3.1 shows data collapsing when front position and time are normalized by the geometric and kinematic parameters introduced earlier. Generally, two distinct phases were observed during the development of the gravity current: i) a first slumping phase, characterized by a linear relation between front position and time after the gate removal and ii) a second phase, or self-similar phase,

in which the current moves under the balance between buoyancy and inertial forces, with the front position a nonlinear function of time. Run R3 shows, however, deviation from the general trend of the remaining runs which is more evident during the second phase of the current development, as also observed by La Rocca *et al.* (2008) when analyzing the effect of bed roughness on the front propagation.

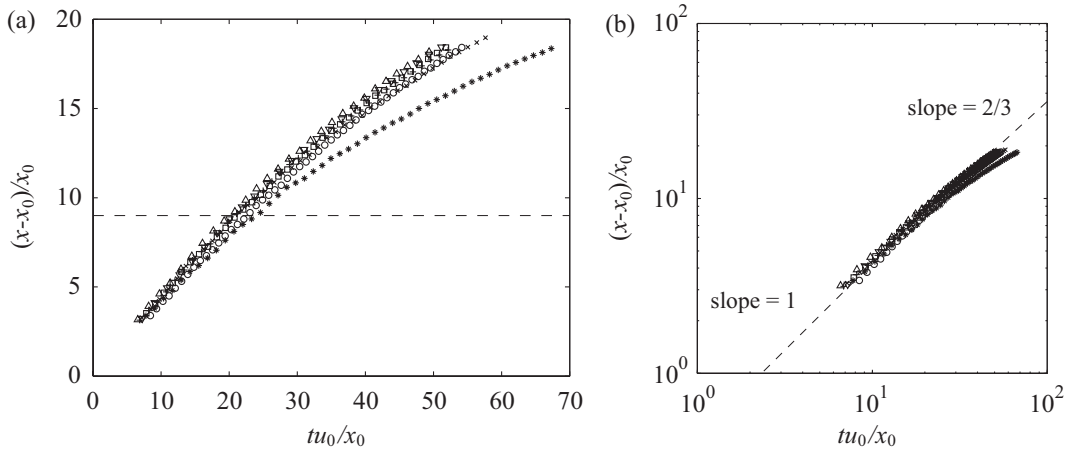

Figure 3.1: Temporal evolution of the non-dimensional current front position for each run: (a) normal scale; (b) logarithmic scale (symbols explained in Table 2.3)

According to the literature (i.e. Rottman and Simpson 1983), a linear phase takes place until $(x_f - x_0)/x_0 \approx 9$, which is confirmed by the general trend observed in Figure 3.1. Run R3, however, has a shorter linear phase, the transition to a second phase occurring earlier than the remaining runs, which leads to the conclusion that scales related to bed roughness and possibly to bed porosity may play a role in the current kinematics. As argued by Peters and Venart (2000), extra resistance due to bed shear stress of rougher beds combined with a reduction of the current buoyancy due to entrainment of ambient fluid at the bed level may cause an earlier end of the first phase. Therefore, for a proper normalization of front position in time, an additional parameter, taking into account the roughness of the bed material, is needed.

Transition points between linear and nonlinear phases were estimated by applying a linear regression to $x_f(t)$ data by a least-squares approach. The nonlinear phase was adjusted by a power law of type

$$(x_f - x_0)/x_0 = \beta_1 (tu_0/x_0)^{\beta_2} \tag{3.1}$$

where coefficients β_i were obtained through a least-squares regression applied after data linearization. The coefficient of determination, r^2, was used to evaluate the goodness of fit. Table 3.1 summarizes the main parameters of each phase for all runs, where t_{f1} and x_{f1} are the time and

space coordinates corresponding to the transition between linear and nonlinear phases and u_{f1} the constant velocity during the first phase. Values of front velocity shown here were obtained by derivation in time of the regression function adjusted to the linear phase.

Table 3.1: Main parameters of the two phases of the current development identified on the lock-exchange experiments

Run	linear phase					nonlinear phase		
	$t_{f_1}u_0/x_0$ (-)	$(x_{f_1}-x_0)/x_0$ (-)	u_{f_1} (m·s^{-1})	u_{f_1}/u_0 (-)	r^2 (-)	β_1 (-)	β_2 (-)	r^2 (-)
D1	20.8	8.5	0.07	0.41	0.9993	0.74	0.81	0.9982
D2	14.7	6.6	0.11	0.46	0.9993	0.74	0.81	0.9986
D3	18.1	8.4	0.14	0.47	0.9964	0.90	0.78	0.9987
D4	20.4	9.1	0.16	0.45	0.9979	0.87	0.78	0.9990
R1	21.3	9.3	0.11	0.44	0.9977	0.91	0.76	0.9985
R2	21.4	9.3	0.11	0.44	0.9967	1.01	0.73	0.9983
R3	6.8	3.1	0.12	0.48	0.9835	0.78	0.76	0.9947

In the slumping phase, front velocity is roughly constant, the average being a non-dimensional value, normalized by the buoyancy velocity (cf. Eq. 2), $u_{f1}/u_0 = 0.46 \pm 0.02$ for all the runs, in agreement with previous results (Rottman and Simpson 1983, Marino *et al.* 2005). Transition between slumping and self-similar phases were obtained in the range $(x_f - x_0)/x_0 = 8.4 \pm 1.0$, which is in accordance with previous observations. The earlier end of the linear phase observed for run R3 does not affect the propagating velocity of the current during the initial phase. Nevertheless, in the first instants of the current, buoyancy and inertial effects seem to still be balanced, indicating that both mechanisms originated by the rougher bed, i.e., current deceleration due to extra bed drag and extra entrainment at the bed level, did not produce effect at that stage. Both the rough scale and the porosity of the bed material may play a role in the current kinematics, although in the present case, given that the current dilution in run R3 is similar to run D2 (see discussion on Section 3.3.2), the main effect on delaying the current front velocity is produced by the extra bottom drag. Although 3D gravity currents were seen to have different kinematic behaviors in the first phase (La Rocca *et al.* 2008), since the reflected bore could not reach the current front due to geometric constraints, an early transition to a second phase of decreasing velocity was still detected when increasing the bed roughness. Moreover, roughness effect is more visible in the second phase.

During the second phase, a deceleration of the flow was observed converging to the front evolution typical of the self-similar phase of lock-exchange experiments when finally the upstream bore arrived at the front. Linearized front position data collapse well and consistently around straight lines with slopes in the range 0.73 to 0.81 (Table 3.1), with an average value of 0.78 (excluding test R3), slightly higher than the value of 2/3 predicted in the literature. The tank where the experiments were performed is 3.0 m long, thus no viscous phase was observed in accordance with previous results in the literature (Huppert 1982).

3.3.2 Time-space varying current height and depth-averaged density

Figure 3.2 shows the temporal evolution in the non-dimensional current height, h/h_0, where h is the current height, along the x-axis for all runs performed. These plots show the signatures of the instabilities typically present in the mixing layer of the current (near vertical darker regions in Figure 3.2), of which the imprint persists in time. These instabilities are *quasi*-stationary, or at least moving downstream at a different time scale than the remainder current, being slightly advected downstream (by drag effect) by the current mean velocity. These structures eventually fade in time and lose their signature by diffusive-type processes (Figure 3.2, final instants).

The initial density of the saline mixture seems to influence the size and periodicity of the instabilities: for lower initial density (run D1) the instabilities show better definition, higher vertical length scale and more regular periodicity, when compared with the runs performed with higher initial density. The effect of the bed roughness is similar to the density one, i.e, bed roughness has a homogenizing effect throughout the current height: less evident billows, or with smaller length scale, were detected when the roughness scale is higher. In fact, preliminary PIV observations from similar experiments (Nogueira *et al.* 2012a) indicate that larger bed roughness induces larger turbulent production in the lower levels, thus higher mixing within the current, justifying the homogenization of density throughout the depth.

Figure 3.3 shows the evolution in the depth-averaged current density in time along the x-axis for all runs performed. Depth-averaged density was obtained by integrating the density within the current below its upper boundary defined by a threshold of excess density of 2 %. The depth-averaged density plots show in general a strongly diluted current in the region of analysis, the maximum of non-dimensional density being around 0.7. Differences in the density value, decreasing as the initial density increases, which are observed for instance when normalizing depth-averaged densities by the density of ambient fluid (not shown here), seem to suggest that the initial buoy-

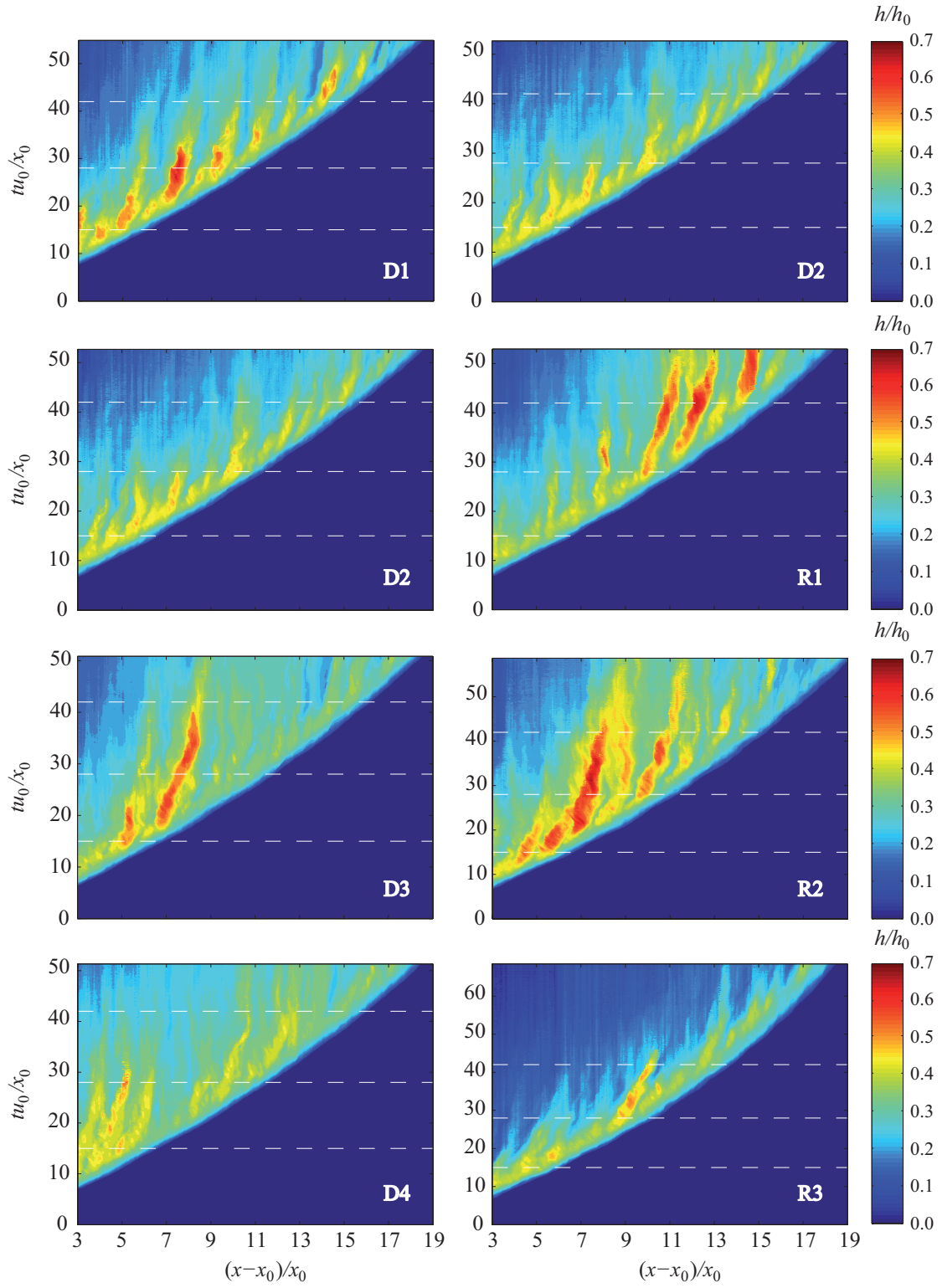

Figure 3.2: Time-space evolution of the non-dimensional current height h/h_0. Left: runs with increasing initial density in the lock, ρ_{c_0}; right: runs with increasing bed roughness, k_s. Horizontal dashed lines at $tu_0/x_0 = 15$, 28 and 42 correspond to the instants represented in Figure 3.4 and 3.5

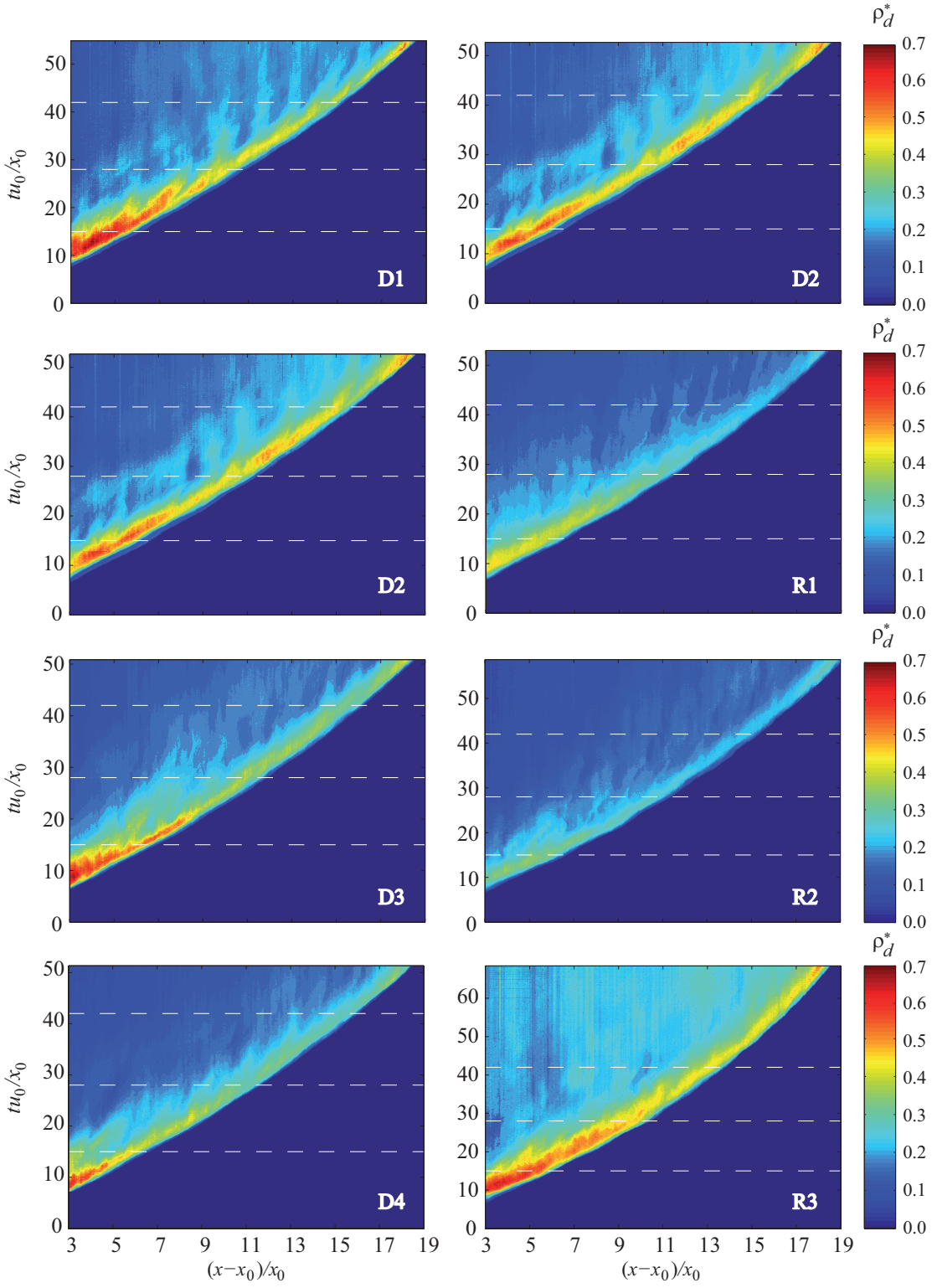

Figure 3.3: Time-space evolution of the non-dimensional current depth-averaged density $\rho_d^* = (\rho_d - \rho_{a_0})/(\rho_{c_0} - \rho_{a_0})$. Left: runs with increasing initial density in the lock, ρ_{c_0}; right: runs with increasing bed roughness, k_s. Horizontal dashed lines at $tu_0/x_0 = 15$, 28 and 42 correspond to the instants represented in Figure 3.4 and 3.5

ancy plays an important role in the mixing process: as the initial buoyancy increases, a faster decay of current density was observed due to a stronger mixing between current and ambient fluid, as observed also by Cenedese and Adduce (2008, 2010). Figure 3.3 also shows, as expected, that the foremost region of the current, i.e., the current head, is the region in the entire current where higher density was observed (cf. Figure 2.9).

Regarding the roughness effect, in general, as the bed roughness increases the front velocity decreases; it can be seen by observing the evolution in the front position in time (Figure 3.1; Figure 3.2 and Figure 3.3, sequence D2, R1, R2 and R3; the slope of the edge between white and grey regions represents the front velocity), which is in accordance with literature (Peters and Venart 2000, La Rocca *et al.* 2008, Adduce *et al.* 2009); the sequence D2, R1 and R2 of increasing roughness in Figure 3.3 shows a gradual decrease in the depth-averaged density. However, for the highest roughness (run R3) that observation is not valid; in terms of density, no meaningful difference was observed when comparing with smooth bed (run D2). These observations suggest that bed roughness plays an important role in the current kinematics and the effect induced by the size of the roughness material needs further investigation.

3.3.3 Height and depth-averaged density profiles

For each run, profiles of non-dimensional current height for three selected time instants (tu_0/x_0 = 15, 28 and 42, shown in Figs. 3.2 and 3.3 with horizontal dashed lines) are plotted in Figure 3.4. The effect induced by the increase in initial density in the lock is clear in the increase in the front velocity, as expected (Cantero *et al.* 2007). In general, current height does not seem to be influenced by the initial buoyancy or roughness: current height is kept quite the same over time, varying roughly between $0.3 < h/h_0 < 0.5$. The instabilities identified in Figure 3.2 are visible; both figures confirm their *quasi* stationary character and their disappearance mainly by diffusive-type processes. Figure 3.4 indicates as well that an increase in the initial density is related to a more stable mixing layer, i.e. with less evidence of large-scale billows. For each run, profiles of non-dimensional depth-averaged density for three selected time instants (tu_0/x_0 = 15, 28 and 42, shown in Figure 3.2 and 3.3 with horizontal dashed lines) are plotted in Figure 3.5.

As already observed in Figure 3.3, the current head is the region within the current where the highest density was observed, in agreement with previous observations by Marino *et al.* (2005). The roughness effect, as already discussed in 3.3.2, induces a gradual decrease in the depth-average density (sequence D2, R1 and R2). Again, run R3 does not follow the decaying trend and exhibits

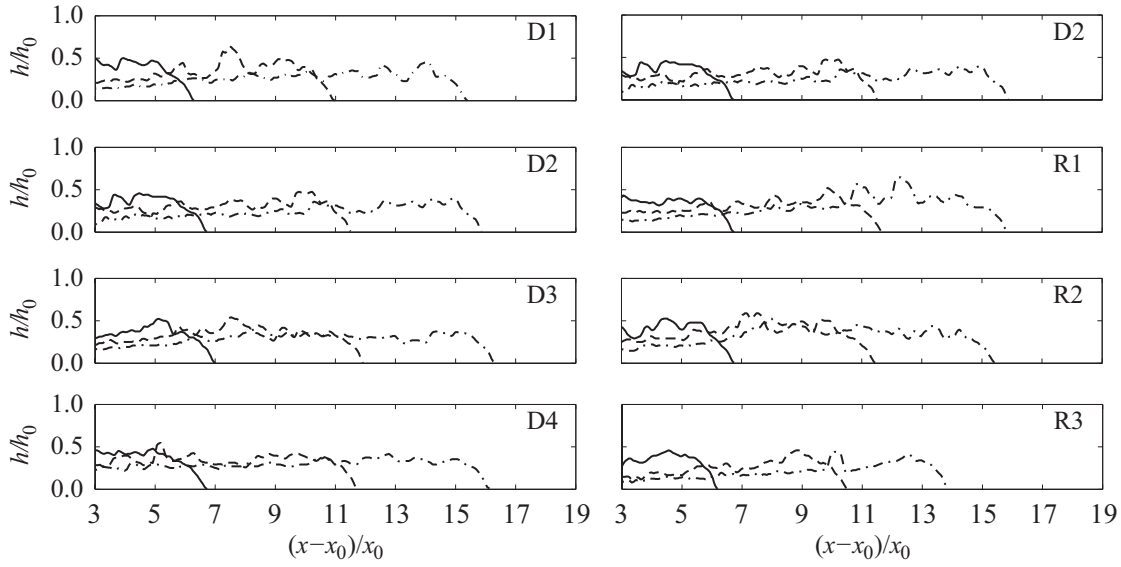

Figure 3.4: Time-space evolution of the non-dimensional current height h/h_0 at selected time instants $tu_0/x_0 = 15$ (solid), 28 (dashed) and 42 (dashed-dotted) (these instants are represented in Figure 3.2 and 3.3 by horizontal dashed lines). Left: runs with increasing initial density in the lock, ρ_{c_0}; right: runs with increasing bed roughness, k_s. Note that both h and h_0 are measured from the top of the crests in the R-type experiments

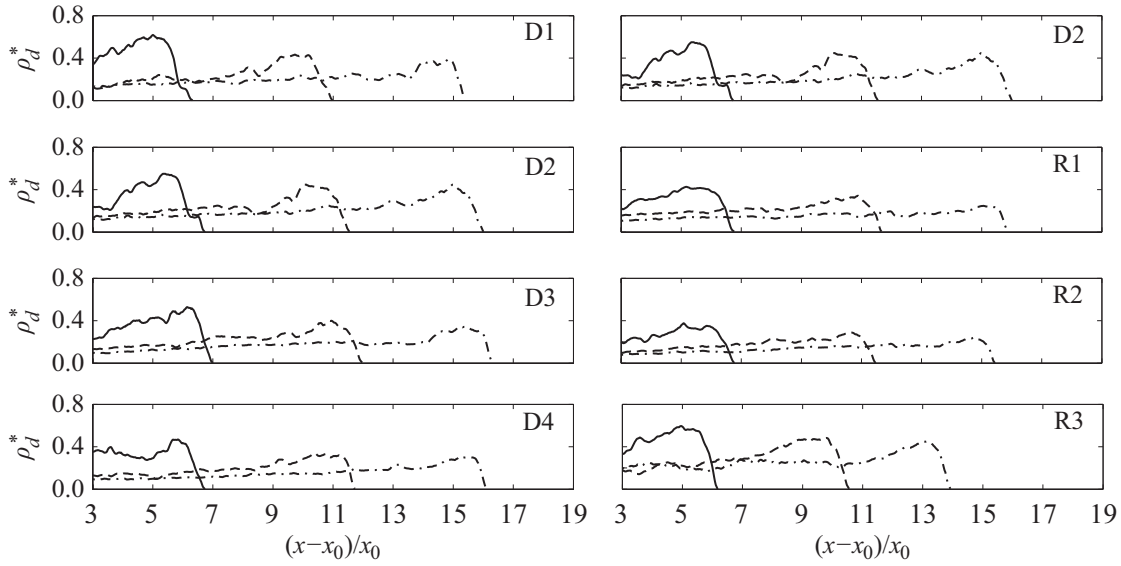

Figure 3.5: Profiles of the non-dimensional depth-averaged density at selected time instants $tu_0/x_0 = 15$ (solid), 28 (dashed) and 42 (dashed-dotted) (these instants are represented in Figure 3.2 and 3.3 by horizontal dashed lines). Left: runs with increasing initial density in the lock, ρ_{c_0}; right: runs with increasing bed roughness, k_s

values of the same order of magnitude of run D2. Runs performed with smooth bed (D-type runs) do not show relevant variations in time in the depth-averaged density. These differences are more evident when roughness is present. Generally, a slight temporal decay of density values in the head region was observed. As seen before, only run R3 shows an earlier decay in the front velocity caused by the extra bottom drag exerted by the larger bed roughness. The inertial-buoyancy equilibrium existing in the first stages of the current development is interrupted earlier, originating a concentration of mass in the head higher than in other cases. This is evident for instance in the plot corresponding to run R3 in Figure 3.5, in which high values of concentration extend further upstream when compared with the other runs, explaining thus the lesser dilution observed already in Figure 3.3. This justifies the earlier statement that, in this case, extra dilution of the current due to the entrainment of ambient fluid trapped within the bed porosity is not relevant here to current deceleration, when compared with the bed drag influence.

3.3.4 Time series of depth-averaged density

Time series of the depth-averaged density, $\rho_d(t)$, in each streamwise location, x, were shifted in time in order to align the time of arrival of the current front at each x, providing an inertial reference system for further analysis. The temporal series for each streamwise location are plotted in Figures 3.6 and 3.7 (shaded regions), normalized as $\rho_d^* = (\rho_d - \rho_{a_0})/(\rho_{c_0} - \rho_{a_0})$. Two temporal scales are presented, on the top is the time relative to the instant of the current arrival at each x (t_{rel}), and on the bottom is the time relative to the instant the current front first enters the visualization area (x = 0.6 m, Figure 2.7), which shows the relative difference in front velocities among runs. Averaging over the x position, considering the inertial reference system, provides the spatially averaged time series of depth-averaged density, $\langle\rho_d^*\rangle$, also shown in Figures 3.6 and 3.7.

Besides the observations made in the previous sections, regarding front velocity and distribution of density within the current, these plots additionally show that the distribution of $\rho_d(t)$ is similar among streamwise locations. The head region, where higher density values are observed, is also where higher deviation between local and averaged density values is detected; this confirms once more that the head is the region within the current where intense mixing, and consequent high dilution, occurs. The body of the current is characterized by continuously decreasing depth-averaged density in time.

Figure 3.8 shows the normalized spatially averaged density, $\langle\rho_d^*\rangle$, plotted over normalized time after the gate removal, tu_0/x_0, for all runs performed. Despite deviations in the head region, more

evident as the bed roughness increases, there is a good data collapse in the arrival of the current as well as in the current body, highlighting the similarity of $\langle \rho_d^* \rangle$ between runs. Run R3 again deviates from the general trend, where fairly constant depth-averaged density values characterize the body region. Values of excess density should tend to zero for later times, not seen in these experiments due to geometric limitations in the tank length.

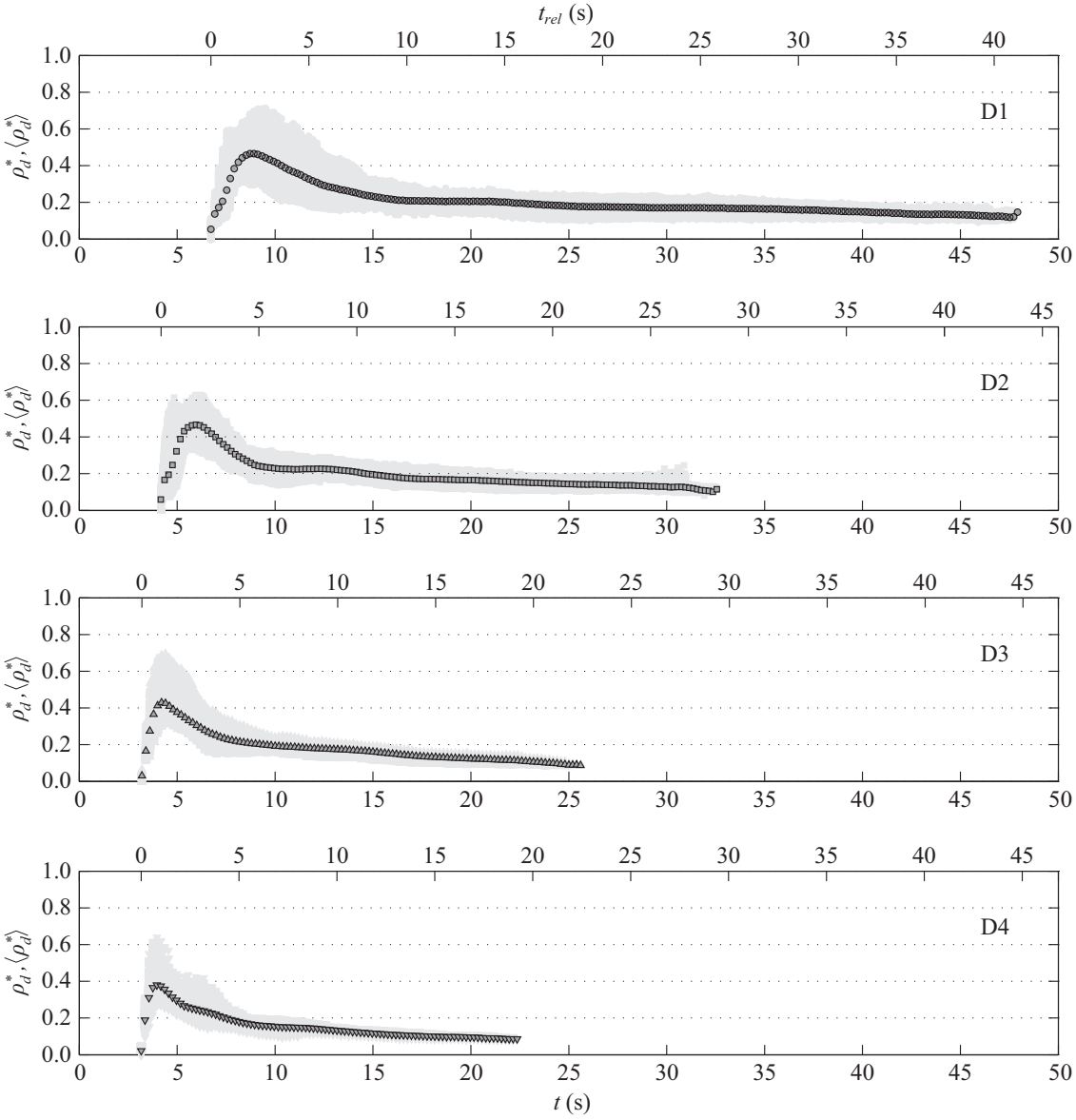

Figure 3.6: Non-dimensional depth-averaged density ρ_d^*: time series for each individual streamwise location, $\rho_d^*(t)$ (shaded areas), were shifted in time in order to align the time of arrival of the current at each x; spatially averaged time series $\langle \rho_d^* \rangle$ (filled symbols), for D-type runs (symbols explained in Table 2.3).

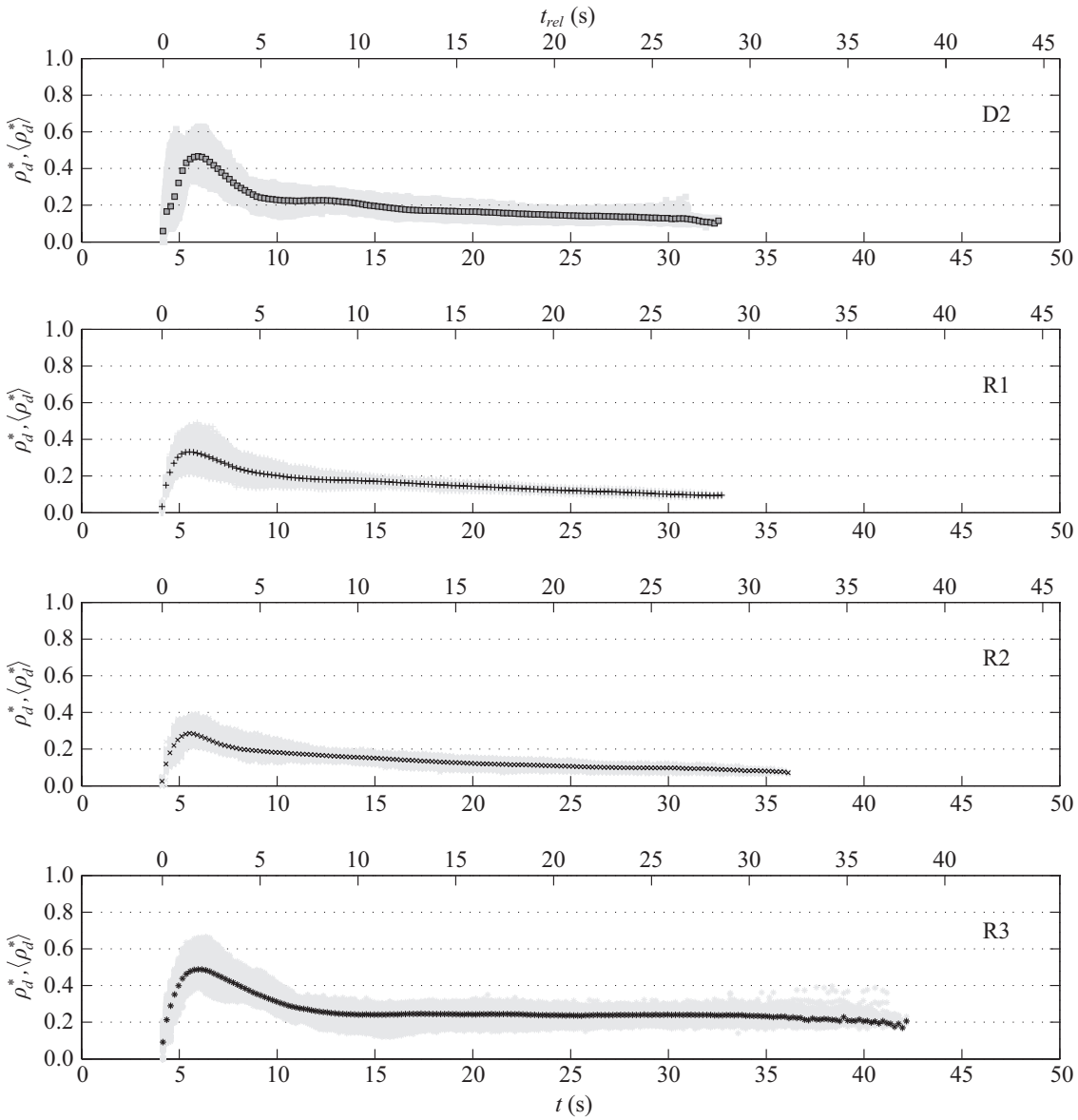

Figure 3.7: Non-dimensional depth-averaged density ρ_d^*: time series for each individual streamwise location, $\rho_d^*(t)$ (shaded areas), were shifted in time in order to align the time of arrival of the current at each x; spatially averaged time series $\langle\rho_d^*\rangle$ (filled symbols), for R-type runs (symbols explained in Table 2.3).

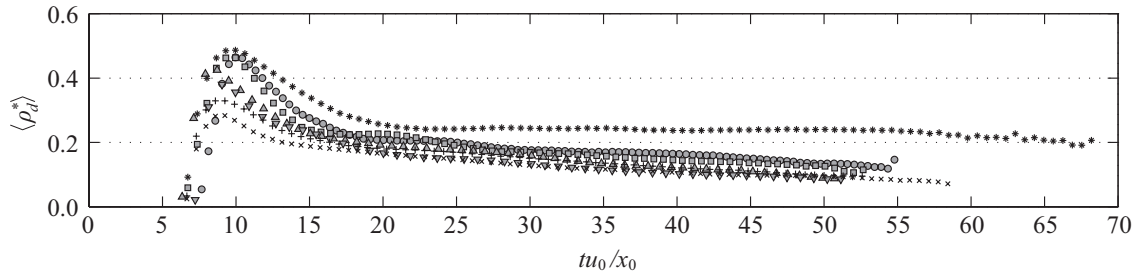

Figure 3.8: Time series of non-dimensional spatial-depth averaged density $\langle\rho_d^*\rangle$, for all runs performed (symbols explained in Table 2.3)

3.3.5 Vertical density profiles

Based on the time series of $\langle \rho_d^* \rangle$ (Figure 3.8), four instants were selected to visualize the vertical density profiles of the gravity current: the instant of maximum $\langle \rho_d^* \rangle$, inside the gravity current head, and three instants corresponding to the body of the current, $tu_0/x_0 = 15$, 25 and 35. Non-dimensional excess density profiles, where the excess density is normalized as $\rho^* = (\rho_c - \rho_{c_a})/(\rho_{c_0} - \rho_{a_0})$, are presented in Figures 3.9 and 3.10, and were obtained by spatial-averaging in x the instantaneous vertical profiles obtained at each x in the selected instants. The vertical axis is normalized by the initial depth in the lock, z/h_0.

Figure 3.9 presents vertical density profiles for the runs performed over smooth bed with varying initial density of the mixture in the lock, ρ_{c_0}. In general, as the initial density increases, the current experiences stronger mixing with the ambient fluid, leading to lower density values overall, as already observed in the plots of Figure 3.3 and discussed in section 3.3.2. Density maxima in the head region is located slightly above the bottom of the tank; the lower values of density at the bottom level are in accordance with the theory of currents advancing on horizontal boundary with no-slip: due to friction, the nose of the current is lifted above the bed, allowing ambient fluid to be entrained below the head, diluting the current. After the head passes, entrainment of ambient fluid from below the current vanishes and the level of density maxima tends to approach the bed level.

For the runs performed over rough bed (Figure 3.10), significant differences from the smooth bed profiles are observed: entrainment from below the head of the current is less pronounced for the two smaller roughnesses tested (runs R1 and R2), whereas in run R3 this effect is more evident, although with lower dilution levels than the smooth bed case (D2); the shape of the density profiles are considerably different in the head region, where density increases nonlinearly with depth.

Figure 3.11 shows the collapse of the density profiles obtained at each selected instant within each run. Here, excess density is normalized by the maximum excess density of each profile and the current height of the mean profile was selected for the vertical length scale (Altinakar 1993). These plots show that there are considerable differences in the mean density profiles obtained in different regions of unsteady gravity currents. However, when plotting together the profiles for all runs, for each instant selected (Figure 3.12), a better data collapse is obtained, in particular in the head region. These observations indicate that there is similarity of the density profiles between unsteady gravity currents performed under different conditions of initial excess density and bed roughness.

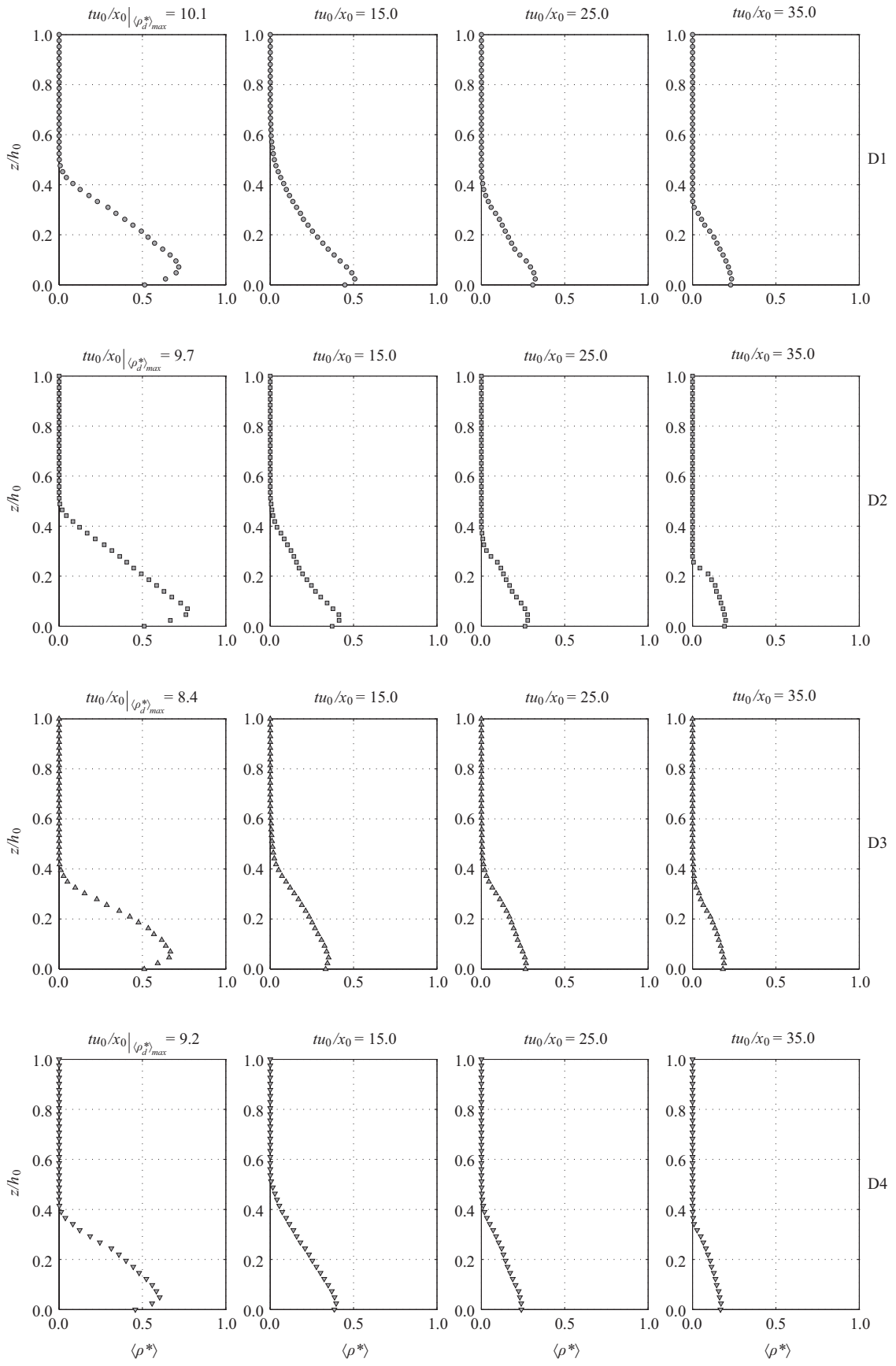

Figure 3.9: Averaged vertical density profiles, $\langle\rho^*\rangle$, for the instants of maximum $\langle\rho_d^*\rangle$ and at instants tu_0/x_0 = 15, 25 and 35. Runs with increasing initial density in the lock, ρ_{c_0} (symbols explained in Table 2.3)

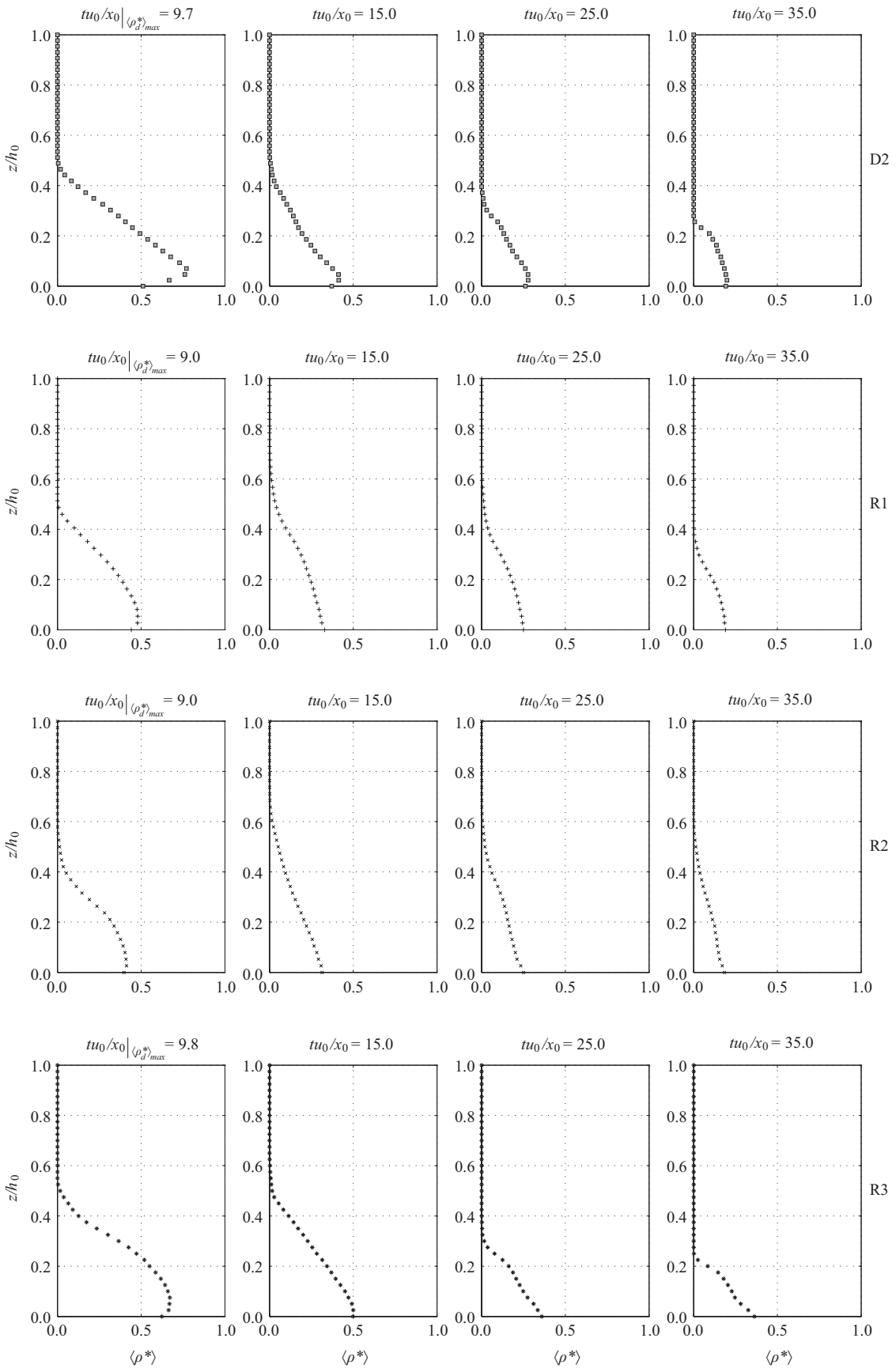

Figure 3.10: Averaged vertical density profiles, $\langle\rho^*\rangle$, for the instants of maximum $\langle\rho_d^*\rangle$ and at instants tu_0/x_0 = 15, 25 and 35. Runs with increasing bed roughness, k_s (symbols explained in Table 2.3)

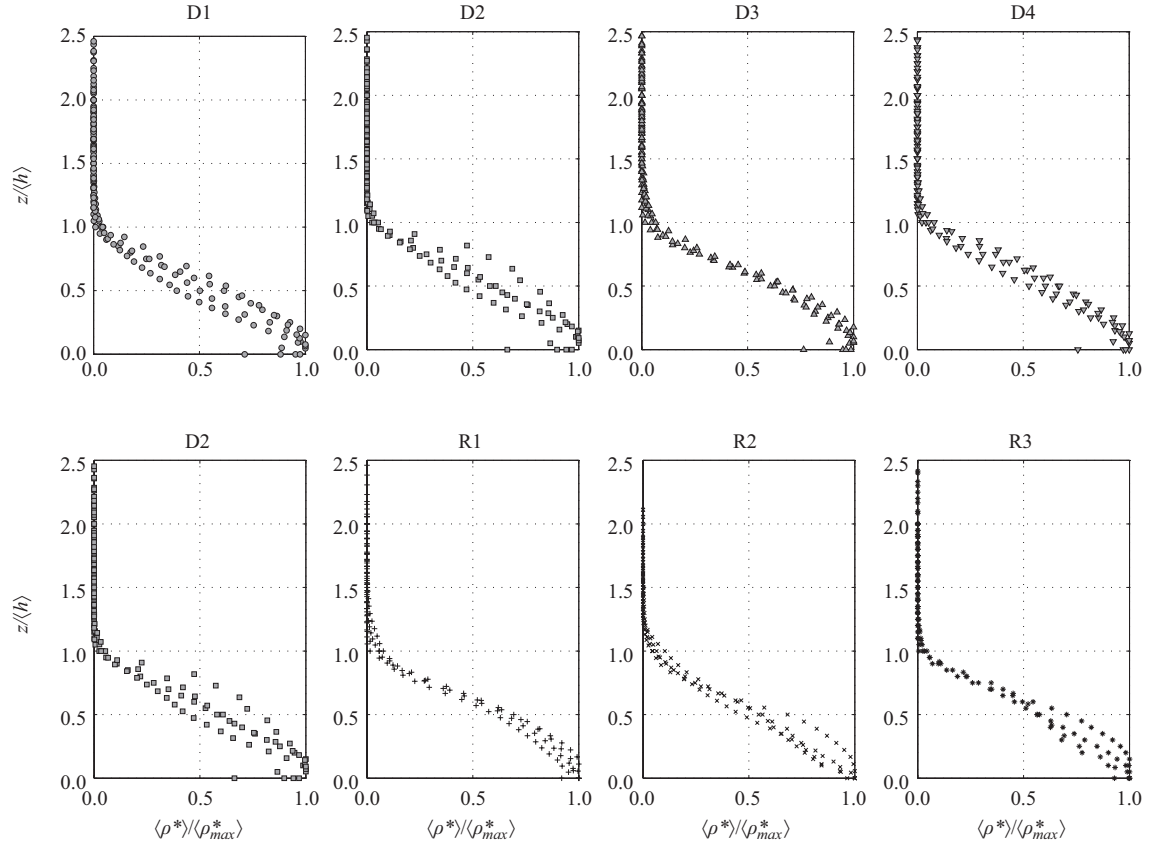

Figure 3.11: Collapse of the averaged vertical density profiles within each run, for the instants of maximum $\langle\rho_d^*\rangle$ and for tu_0/x_0 = 15, 25 and 35 (symbols explained in Table 2.3)

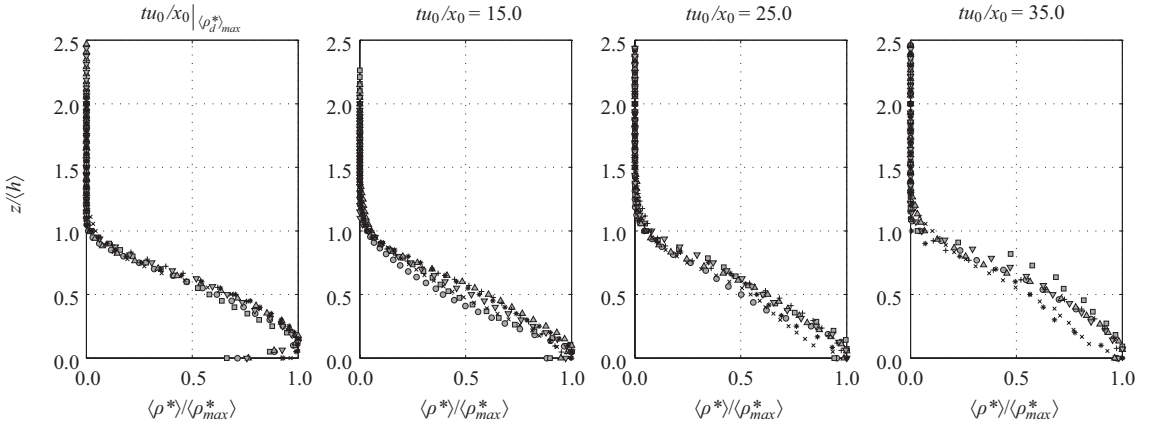

Figure 3.12: Collapse of the averaged vertical density profiles for all runs, for the instants of maximum $\langle\rho_d^*\rangle$ and for tu_0/x_0 = 15, 25 and 35 (symbols explained in Table 2.3)

3.3.6 Front velocity

Time-varying densimetric Froude number, based on the front velocity, u_f, defined as:

$$Fr = \frac{u_f}{\sqrt{g'_0 d}} \tag{3.2}$$

was computed using three different length scales, i.e. characteristic depths, d, of the current: initial water depth in the lock, h_0, maximum height of the head, h_m, and, height at the rear of the head, h_r (see Figure 3.13 for an explanation of the latter). Froude numbers so obtained were compared with local Froude numbers of the head region defined as:

$$Fr_h = \frac{u_f}{\sqrt{g'_h d}} \tag{3.3}$$

where g'_h is the local reduced gravity computed by using the head-averaged density of the current at each instant: $g'_h = g(\rho_h - \rho_{a_0})/\rho_{a_0}$. Similarly, the very same three different depths were used as characteristic heights: h_0, h_m and h_r.

To assess local parameters at the current head, a criterion to isolate this region of the current has been established. Previous contributions have shown that the head is the region where higher density is observed within the current (Hacker *et al.* 1996, Hallworth *et al.* 1996, Marino *et al.* 2005), which is in accordance with the results above discussed in sections 3.3.2 and 3.3.3. Therefore, the criterion defined here to characterize and isolate this region is based on a dynamic function given by the product between local values of depth-averaged density and current height:

$$W(x,t) = \rho_d(x,t)h(x,t) \tag{3.4}$$

which corresponds to local vertically-averaged mass of the current. The upstream limit of the head, and therefore the head length L_h, was defined by taking the position of the first meaningful local minimum of function W (Eq. 3.4), near the front. Figure 3.13 shows a scheme of the current with the definition of the characteristic variables of the head.

Figure 3.14 shows Froude numbers computed for runs performed with smooth bed (runs D), with bulk initial reduced gravity (Eq. 3.2) and local reduced gravity (Eq. 3.3) (left and right, respectively), and using the three above mentioned characteristic heights - h_0, h_m and h_r (a to c and d to f, respectively). Velocities are taken from derivation of regression curves (Table 3.1)

applied to $x_f(t)$ data.

In general, a good data collapse is observed using both initial and local reduced gravity (Figure 3.14 left and right, respectively). An evident distinction between first and second current phases is observed in all plots; during the constant-velocity phase, Fr exhibits some scatter which is reduced in the self-similar phase.

Froude numbers estimated using h_0 and initial reduced gravity (Figure 3.14a) show a constant plateau around 0.46 during the constant-velocity phase, in agreement with what is reported in literature (Shin *et al.* 2004, Marino *et al.* 2005). During the self-similar phase, $(x_f - x_0)/x_0 > 9$, Froude number Fr_{h_0} starts to decrease. When using h_r and h_m as characteristic height (Figure 3.14b and c), data collapses to a constant plateau of 0.6 during the second phase. Both results, with h_r and h_m are similar, only slightly different in terms of amplitude due to the evident differences in these geometric values (cf. Figure 3.13). In terms of magnitude, Fr_{h_m} and Fr_{h_r} plateaus are slightly lower than the value reported in literature, 0.81, when using the maximum height of the head (Marino *et al.* 2005). These differences may be explained by differences in the length scale used by these authors.

When normalizing by local reduced gravity (Figure 3.14, right side), higher values of Fr are observed. Froude numbers estimated using h_0 (Figure 3.14d) show a roughly constant plateau around 0.6 during the constant-velocity phase, decreasing gradually to $(x_f - x_0)/x_0 > 9$. Local Froude numbers based on h_m and h_r oscillate around 0.9 and 1.1, respectively, and a narrow collapse is observed during the self-similarity phase (Figure 3.14e and f).

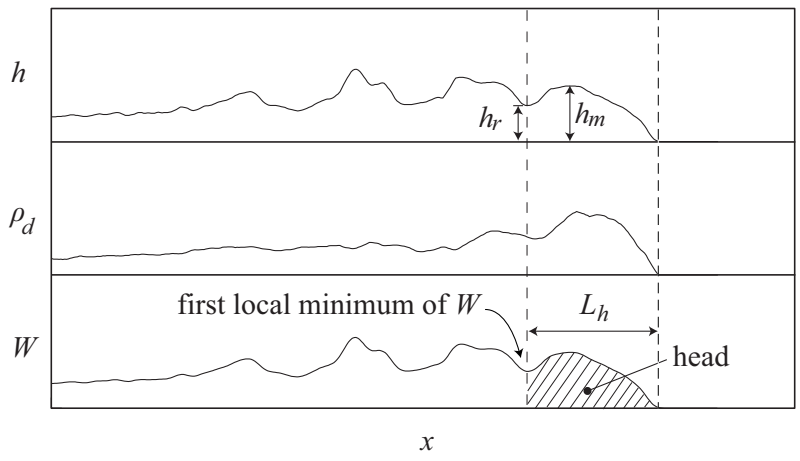

Figure 3.13: Definition of the head of the density current and its characteristic variables

In general, observations show that after the constant-velocity phase current kinematics are ruled by the current head, i.e., the remaining body of the current does not play an important role in the current development. When using bulk quantities for the normalization of the front velocity (Figure 3.14a), data collapses well around the expected value of 0.46 in the first phase indicating that at this early stage, the whole current body rules the front propagation. At this stage no apparent head detached from the remaining current is observed. The evolution of the current is governed by the bulk movement of the denser mass stored in the lock, indicating that buoyancy effects are given by the total body and its bulk parametrization. During the second phase, when the reflected bore catches the front of the current, the current is clearly fragmented into a body and a well defined head with own momentum, penetrating in the ambient fluid. The front velocity is thus determined

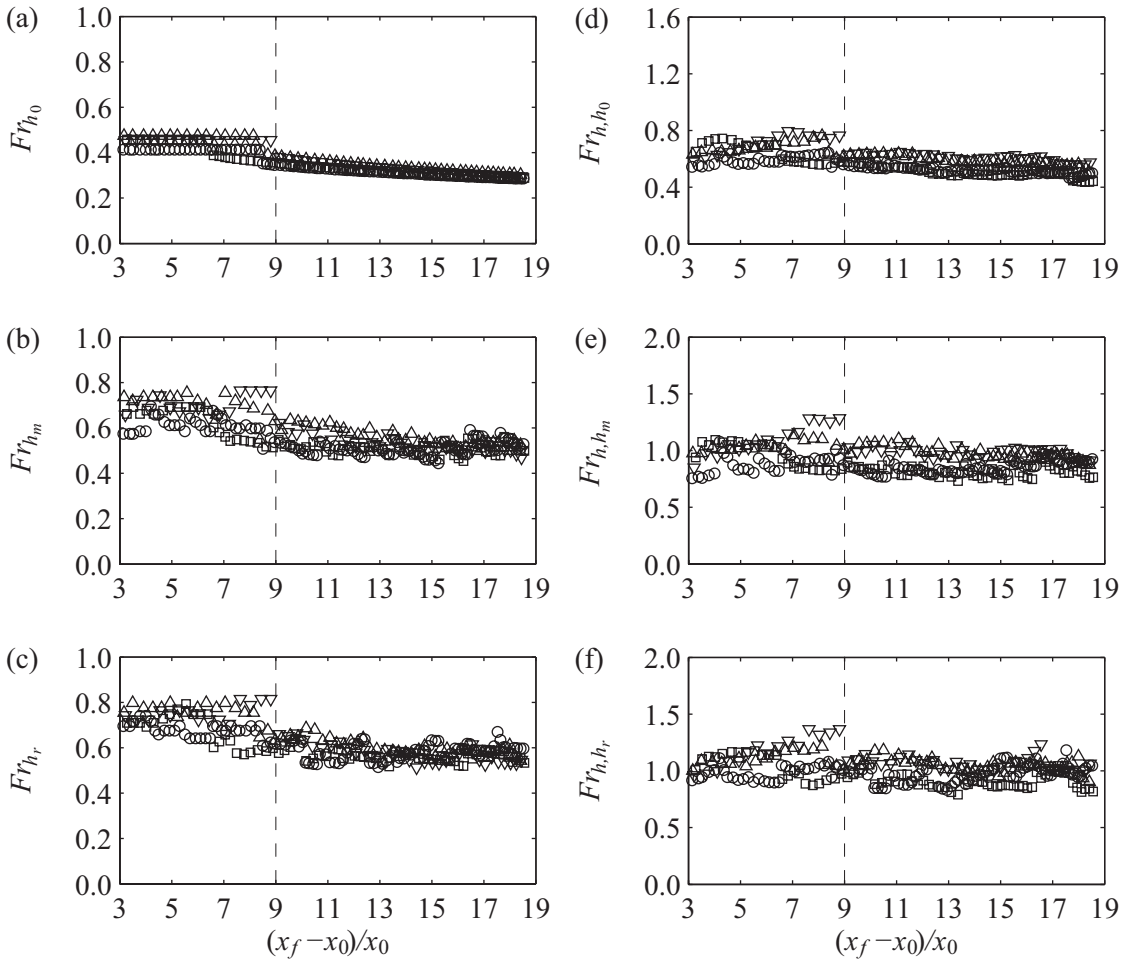

Figure 3.14: Evolution of Froude numbers considering (left) initial reduced gravity and (right) local reduced gravity, and using different characteristic heights defined as: (a) and (d) initial depth in the lock, h_0; (b) and (e) maximum height of the head, h_m; and (c) and (f) height at the rear of the head, h_r. Runs performed with smooth bed (D1, D2, D3 and D4). The limit of the first phase suggested in the literature of $(x_f - x_0)/x_0 = 9$ (Rottman and Simpson 1983) is indicated by vertical dashed lines (symbols explained in Table 2.3)

by this detached head, being in equilibrium with its buoyancy celerity, as concomitantly observed in Figure 3.14(e) ($Fr_{h,h_m} \approx 1$, thus $u_f \approx \sqrt{g'_h h_m}$). Only when using all local variables to define Froude number (Figure 3.14e and f), a plateau (and not a decreasing trend as seen in Figure 3.14b and c) is observed indicating the full dependency of the front velocity on the head dynamics. The fact that in the early stages of the current development no well defined head exists may be responsible for the scatter observed in Froude numbers for $(x_f - x_0)/x_0 < 9$, when using local variables (Figure 3.14d to f) which justifies the bulk character of the current propagation at this stage and, hence, local parametrization may not be adequate here.

Figure 3.15 shows Froude numbers concerning run D2 and runs of R-type, which show a similar trend observed in Figure 3.14 for runs performed with smooth bed. These plots show again

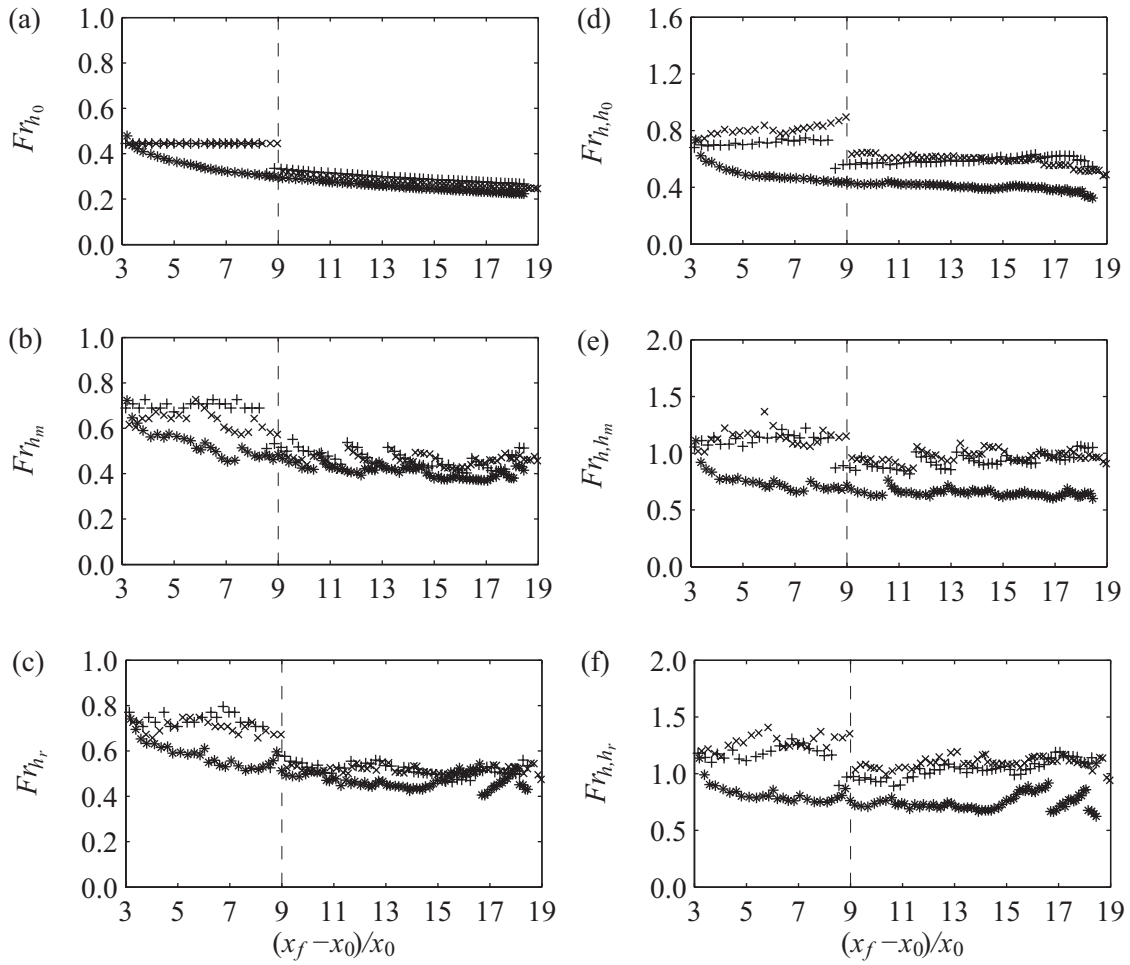

Figure 3.15: Evolution of Froude numbers considering (left) initial reduced gravity and (right) local reduced gravity, and using different characteristic heights defined as: (a) and (d) initial depth in the lock, h_0; (b) and (e) maximum height of the head, h_m; and (c) and (f) height at the rear of the head, h_r. Runs performed by changing the roughness of the bed (D2, R1, R2 and R3). The limit of the first phase suggested in the literature of $(x_f - x_0)/x_0 = 9$ (Rottman and Simpson 1983) is indicated by vertical dashed lines (symbols explained in Table 2.3)

an evident deviation from run R3, which assumes, in general, lower Froude numbers. Figure 3.15a shows a constant plateau around 0.45 for runs R1 and R2, while run R3 exhibits a decreasing trend starting at the early stages of current development. During the second phase, data from the three experiments collapse and decrease at similar rate. Runs R1 and R2 show Fr_{h_m} and Fr_{h_r} data collapsing above 0.6 in the similarity phase when using initial reduced gravity (Figure 3.15, left side). When normalizing by local reduced gravity (Figure 3.15, right side), runs R1 and R2 show data collapsing around approximately constant values, independently from the stage of development of the current: $Fr_{h,h_0} = 0.7$, $Fr_{h,h_m} = 1.0$ and $Fr_{h,h_r} = 1.2$.

3.4 Discussion and conclusions

Gravity currents produced by lock-release of saline water into a finite open-channel of horizontal bed, filled with an ambient fluid of fresh water, are presented and discussed as regards the evolution of the front position, the time and space evolution of the current height, as well as the depth-averaged density, density profiles and front propagation velocity. Seven different experiments were performed by varying the initial density of the saline mixture in the lock and bed roughness, maintaining constant all the other experimental variables.

In general, all runs show the development of the current in two distinct phases, which is in agreement with the literature for lock-exchange flows with similar characteristics. Results confirm that in the first stage of current development front velocities are nearly constant. When normalized by a characteristic velocity defined with initial quantities of each experiment, u_0, values of non-dimensional front velocity fall in the range $u_f/u_0 = 0.46 \pm 0.02$, confirming previous observations. The transition between slumping and self-similar phases occurs when the reflected bore overtakes the front of the current. This stage was seen to occur in the range $(x_f - x_0)/x_0 = 8.4 \pm 1.0$, which is in accordance to what has been previously observed. During the self-similar phase, front position decreases in time and is a function of $t^{0.78}$, approximately, which is higher than $t^{2/3}$ described in literature. The run performed with higher bed roughness does not follow the general observations since the transition to the self-similar phase occurs earlier than the remaining runs. The deviation of run R3 from the remaining runs is more evident during the self-similar phase, which shows that the effect induced by bed roughness is more relevant during the second stage of current development. For a proper parametrization of the front position in time, a parameter taking into account the roughness and porosity of the bed material is thus required.

The increase in the initial density of the mixture in the lock has a direct effect on the front propagation, higher front velocities being detected when the initial buoyancy of the gravity current increases. When normalizing the evolution of the front position by the initial parameters x_0 and u_0, a good data collapse was obtained. Besides front velocity, the initial density was seen to influence the size and periodicity of the large-scale instabilities present in the mixing layer: evident large-scale billows with regular periodicity were detected in the run performed with the lowest density tested. Increasing the initial density was seen to reduce the number of detected large-scale billows.

Results confirm that bed roughness plays an important role in the current development. The influence of the bed roughness apparently depends on its length scale. Three materials with different D_{50} to reproduce different rough beds were investigated; runs R1 and R2, with lower D_{50}, show a smooth deceleration in the front propagation; run R3, in turn, presents a stronger deceleration, as expected, but no significant dilution is observed when compared with the smooth bed case (run D2). These observations show that bed roughness plays an important role in the current kinematics and it needs further investigation.

Large-scale instabilities present in the mixing layer between current and ambient fluid are well observed in the plots of current height. The length scale and the periodicity of these structures seem to depend both on the initial buoyancy of the current and on bed roughness: as the initial buoyancy increases, billows with smaller length scales are observed and no well defined spatial periodicity is detected; regarding the effect of bed roughness, it was observed that an increase in the size of the bed material induces a homogenizing effect throughout the current height, less large-scale billows being observed. This may be related to extra turbulent production in the lower levels, inducing extra mixing within the current. The genesis of these large-scale instabilities might be related to dynamics at the current head, which in turn is ruled by local buoyancy forces; as current develops and ambient fluid is being entrained into the current, local density decreases and so does local reduced gravity. The resulting buoyancy forces are reduced allowing fluid to expand in the vertical direction, forming billows with higher length scales.

The analysis of the temporal evolution of current depth-averaged density shows a significantly diluted current in the region of analysis, indicating that entrainment and consequently, current dilution, occurs since the early stages of current development. In these experiments, it was confirmed that the head region is where higher density is observed within the gravity current. This observation was used as a criteria to isolate the head region, enabling an analysis based on local variables at the head.

Vertical density profiles have shown that entrainment of ambient fluid also occurs from below the gravity current, since the profiles taken in the head region show lower density values near the flow bed. This effect vanishes towards the body of the current, where the density maxima tends to be located near the flow bed.

In the early stages of the current development, no apparent head detached from the remaining current is observed. This may be responsible for the scatter observed in the densimetric Froude numbers in the slumping stage when using local variables, justifying the bulk character of the current propagation at this stage. When the reflected bore overtakes the current front, the current is fragmented into a body and a well defined head, the front velocity being in equilibrium with its buoyancy celerity. Froude numbers defined by all local variables show a plateau around $Fr = 1$ in the self-similar stage, indicating the full dependency of the front velocity on the head dynamics.

Chapter 4

DYNAMICS OF THE HEAD OF GRAVITY CURRENTS BASED ON DENSITY MEASUREMENTS

Contents

Chapter 4 is based on the paper 'Dynamics of the head of gravity currents' published online in Environmental Fluid Mechanics, 2013, by the authors H.I.S. Nogueira, C. Adduce, E. Alves and M.J. Franca, and based on the preliminary results presented in Nogueira et al. *(2011a, 2012a,b,c, 2013b). This paper explores the dynamics of the head of unsteady gravity currents by assessing the time-varying variables characterizing the head. Entrainment of ambient fluid into the denser current is assessed by both bulk and local approaches as well.*

Abstract

The present work experimentally investigates the dynamics of unsteady gravity currents produced by lock-release of a saline mixture into a fresh water tank. An image analysis technique was applied to visualize and characterize the current allowing thus the understanding of its general dynamics and, more specifically, of the current head dynamics. The temporal evolution of both head length and mass shows repeated stretching and breaking cycles: during the stretching phase, the head length and mass grow until reaching a limit, then the head becomes unstable and breaks. In the instants of break, the head aspect ratio shows a limit of 0.2 and the mass of the head is of the order of the initial mass in the lock. The average period of the herein called breaking events is seen to increase with bed roughness and the spatial periodicity of these events is seen to be approximately constant between runs. The rate of growth of the mass at the head is taken as a measure to assess entrainment and it is observed to occur at all stages of the current development. Entrainment rate at the head decreases in time suggesting this as a phenomenon ruled by local buoyancy and the similarity between runs shows independence from the initial reduced gravity and bed roughness.

4.1 Introduction

Hallworth *et al.* (1996) and Hacker *et al.* (1996) investigated unsteady gravity currents over horizontal beds produced by the lock-exchange technique and, through two different visualization techniques, commented the inner structure of the current. Hallworth *et al.* (1996) observed that unsteady gravity currents have a distinct inner structure when compared to steady gravity currents, namely in what regards the extent of mixing: steady currents have a shorter mixing layer, near the upper boundary, above an undiluted layer which is continuously replenished by denser fluid from the tail. Regarding entrainment into the head region, Hallworth *et al.* (1996) argue that during

the slumping phase the head remains undiluted, i.e., no entrainment takes place during this phase, and the head is progressively reduced in length. Thereafter, when the reflected bore reaches the current front, even though ambient fluid is continuously entrained into the head region, the head volume decreases as the current develops towards downstream due to mixed fluid left behind in the tail. Hacker *et al.* (1996), through an image analysis technique based on light absorption, assess the density distribution within the current and show that this is more complex than what was previously accepted. By analyzing the temporal evolution of different iso-density contours, they observed that entrainment is present at all stages of the current development. The change of the aspect ratio of the lock, the gate removal and the Reynolds number of the flow were seen to influence the initial development of the current, leading to a broad range of density distribution within the current, originating different extents of mixing.

The general characteristics of gravity currents, such as density and location, are important in many applications in geophysics and civil engineering and are determined by the amount of entrained fluid into the current during its evolution. Ellison and Turner (1959) drew attention to the entrainment phenomenon and performed experiments of continuously fed gravity currents over smooth bed with varying slope, with $Re \sim 1000$. The entrainment parameter is therein defined as the ratio between the velocity of entrained fluid into the current and a velocity scale of the current (E) and it is shown to be dependent on bulk Richardson number. Based on their experiments, the well-known relation $E = (0.08 - 0.1Ri)/(1 + 5Ri)$ was established, valid for $Ri <= 0.8$. They predict the entrainment parameter to be negligible for high Richardson numbers ($Ri > 0.8$). Their work motivated the development of further research on mixing in gravity currents (Parker *et al.* 1987, Hallworth *et al.* 1996, García and Parsons 1996, Cenedese *et al.* 2004, Princevac *et al.* 2005, Cenedese and Adduce 2010, among many others), being the parameterization of mixing in dense currents still an area of active research nowadays. The influence of Richardson number, or densimetric Froude number, on the entrainment parameter, as well as the slope of the bed, have been considered since the early works. Only recently, the dependence on Reynolds number was also investigated and seen to be fundamental in the prediction of entrainment (Princevac *et al.* 2005, Fernandez and Imberger 2006, Cenedese and Adduce 2008), especially in natural flows with high Reynolds numbers ($Re \sim 10^7$) where results deviate substantially from the laboratory-based entrainment laws, usually obtained for $Re \sim 1000$. In Adduce *et al.* (2012) a two-layer shallow water model with entrainment was developed and tested by laboratory experiments with lock-exchange gravity currents in which both initial density and initial saline volume in the lock

were varied. The entrainment was found to play a key role in their simulations.

The present work aims at investigating the dynamics of the head of gravity currents, namely the influence of the density of the fluid in the lock and the bed roughness on entrainment of ambient fluid into the current. This research is based on an experimental work where lock-exchange density currents, induced by salinity differences, are reproduced under controlled conditions in an open tank. The development of the saline currents is captured by a CCD camera, using dye concentration as a tracer, allowing the reconstruction of time and space (2D) evolution of the density fields.

After this introduction, experimental setup is summarized in section 4.2, main results concerning head dynamics and entrainment are presented and discussed in section 4.3, being section 4.4 devoted to the main conclusions.

4.2 Experimental setup

The lock-release experiments were performed in the experimental facilities described in Chapter 2. The saline mixture with initial density ρ_{c_0} is placed in a lock with a vertical sliding gate at a distance $x_0 = 0.15$ m from the upstream section, i.e. left wall, of the tank (cf. Figures 2.1 and 2.2). The right side of the tank is filled with fresh water with density ρ_{a_0}, both sides filled up at same depth. In all experiments, the relative depth of the initial configuration is kept $\varphi = h_0/H = 1$, where $h_0 = 0.2$ m is the depth of the fluid in the lock and H is the total depth of the ambient fluid.

Seven lock-exchange experiments were performed by varying the initial density of the saline mixture in the lock, ρ_{c_0}, and the bed roughness, k_s, leading to the runs (Density) presented in Table 2.3. The preparation of the experiments is as described in subchapters 2.2 and 2.3. The captured video frames are subsequently converted into grey scale matrices in the region of the tank with fluid (702×43 pixels) and then converted into instantaneous density fields of the current through a calibration procedure. Results are shown for a selected window of the field of view (dashed rectangle in Figure 2.7). Details on the evaluation of the current density distribution can be found subchapter 2.3.

4.3 Results

4.3.1 Entrainment parameterization

Following previous definitions for a bulk entrainment parameter (Ellison and Turner 1959), this was herein estimated by:

$$E_b = \frac{u_e}{u_c}, \tag{4.1}$$

being u_e the entrainment velocity and u_c a characteristic velocity of the flow, usually taken as the current velocity relative to its surroundings. The entrainment velocity is obtained by the entrained discharge per unit width over the upper interface of the current, following Cenedese and Adduce (2008) and Adduce *et al.* (2012), defined as follows:

$$u_e = \frac{Q_e}{S_c} = \frac{\mathrm{d}V_c}{\mathrm{d}t}\frac{1}{S_c} \tag{4.2}$$

being Q_e the entrained discharge and S_c the area of the permeable interface of the current, through which entrainment occurs, both time dependent variables and defined per unit width, being $\mathrm{d}V_c/\mathrm{d}t$ and S_c assessed by our experiments. The nature of the gravity currents herein performed is highly unsteady, i.e., their characteristics change continuously as the current evolves towards downstream. In order to evaluate a global entrainment parameter for each run, a bulk evaluation of the properties of the gravity current between two sections was considered. A bulk value for u_e was obtained considering the initial and final configurations of the current during a run for the bulk estimation of $\mathrm{d}V_c/\mathrm{d}t$ while S_c was defined at the end of the experiment. In full depth lock-release flows, the return current, propagating above the denser current in the opposite direction, has non-negligible velocity. Therefore, the difference between mean velocities of both denser and return currents, Δu (cf. Table 2.3), is here considered as the bulk characteristic velocity of the flow (u_c in Eq. 4.1). Considering the bulk height of the denser current, h_b, as $h_b \approx 1/3h_0$, based on the performed experiments (Chapter 3) and by mass conservation considerations, the characteristic velocity of the flow results in $\Delta u \approx 1.5\bar{u}_f$, being $\bar{u}_f$ the bulk front velocity of the denser current, obtained by taking the initial and final positions of the current front and the duration of the experiment (Table 2.3).

Figure 4.1 shows the entrainment parameter obtained for each run as function of bulk Froude and Reynolds numbers defined in equations 2.8 and 2.9, respectively. In general, entrainment parameter, E_b, increases with both Fr_b and Re_b and a plot with a combination of both, Fr_bRe_b clearly

shows this relation. Gravity currents performed with higher initial excess density are expected to have higher values of overall entrainment. Regarding the influence of the bed roughness, slight entrainment increase is detected when comparing runs R1 and R2, over rough bed, with run D2, over smooth bed, suggesting that bed roughness induces higher entrainment. This trend, however, is not followed by run R3, where a lower value for E_b is obtained when using sediments with higher roughness scale to compose the channel bed. Apparently, the effect of extra bed drag in run R3 is more effective in the reduction of current velocity rather than promoting higher entrainment of ambient fluid, confirmed by lower Fr_b and Re_b numbers (cf. Table 2.3).

Keulegan (1949) defined a stability parameter for mixing in stratified flows, $\psi = 1/(Fr^2 Re)^{1/3}$ (in Vanoni 1975), representing the dependence of mixing on both viscous and gravity forces. This parameter is analogous to $Fr_b Re_b$ (Figure 4.1), the difference being attributed to the length scale h_b, which is canceled in ψ. A critical value of the stability parameter for turbulent flows was experimentally obtained by Keulegan (1949), $\psi_c = 0.18$, above which no mixing is expected to occur. For comparison purposes, ψ was herein computed with Fr_b and Re_b and was seen to vary in the range $0.06 < \psi < 0.09$, the lowest value being obtained for the run with highest initial excess density, which is also the run where the highest value for the entrainment parameter, E_b, was obtained.

Figure 4.2 shows the entrainment parameter as function of bulk densimetric Froude number for the present experiments and previous results found in the literature, for gravity currents with $Re > 0.7$, both from laboratory experiments and field observations. Previous experimental results herein presented concern continuously fed gravity currents developing over smooth sloping beds, in both rotating (Cenedese *et al.* 2004, Wells 2007, Cenedese and Adduce 2008) and non rotating

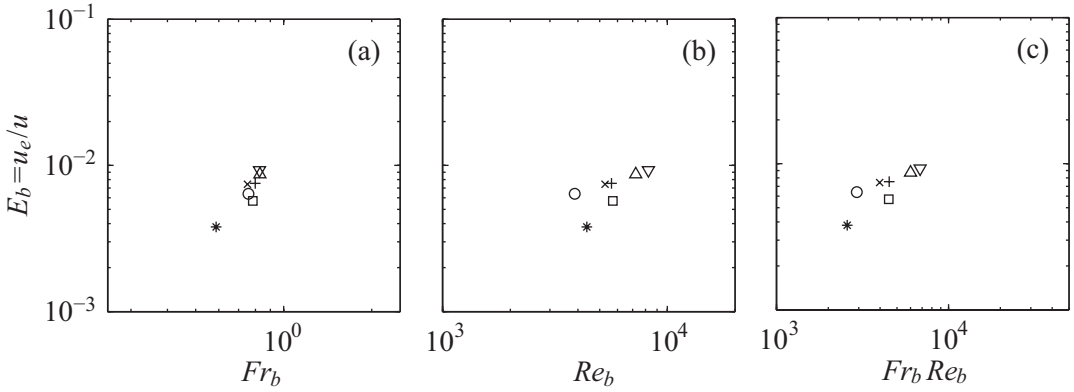

Figure 4.1: Entrainment parameter as function of Fr_b (a), Re_b (b) and $Fr_b Re_b$ (c) (symbols explained in Table 2.3).

(Ellison and Turner 1959, Alavian 1986) experimental apparatus. Field data was obtained in Lake Ogawara (Dallimore *et al.* 2001), Mediterrean (Price and Baringer 1994), Denmark Strait (Girton and Sanford 2003), Faroe Bank Channel (Mauritzen *et al.* 2005), Baltic Sea (Arneborg *et al.* 2007) and in atmospheric katabatic flows (Princevac *et al.* 2005). Figure 4.2 also presents well-known entrainment parameterizations proposed by Ellison and Turner (1959), for conservative gravity currents, and by Parker *et al.* (1987), based on both conservative and non-conservative currents.

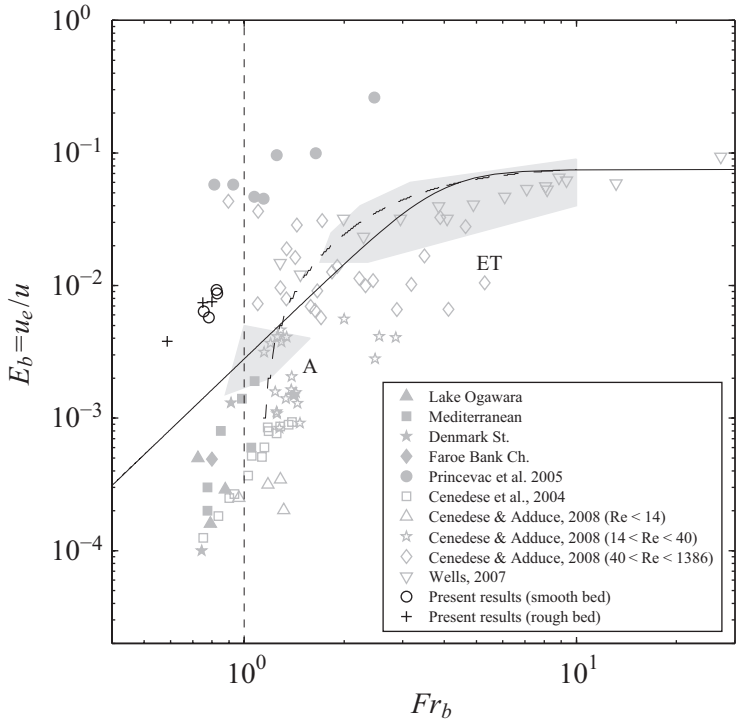

Figure 4.2: Entrainment parameter as function of Froude number. Comparison of present results with results obtained in the field (solid symbols), in the laboratory (open symbols and shaded areas for experiments of Ellison and Turner (1959), ET, and Alavian (1986), A) and entrainment laws suggested by Ellison and Turner (1959) (dashed line) and Parker *et al.* (1987) (solid line) (data from Cenedese and Adduce (2008)).

Figure 4.2 confirms what was observed in Figure 4.1 regarding the dependence of the entrainment parameter on Froude number. Significant deviations of the entrainment parameter for the same Froude number are observed. Martin *et al.* (2012) observed a similar behavior when comparing the entrainment coefficient of gravity currents in the field and in the laboratory; entrainment coefficient had significant deviation for the same Richardson number, leading to conclude that it is unreasonable to have a single relationship of the type $E = f(Ri)$ to cover all shear stratified flows. Those deviations are due to the dependence of the entrainment coefficient also on Reynolds number (cf. Cenedese and Adduce 2008, where is shown that E_b is also an increasing function of Re_b). In Figure 4.2, entrainment parameter obtained in katabatic flows (Princevac *et al.* 2005),

with $Re \sim 10^7$, is always higher than values obtained in continuously fed gravity currents in laboratory by Ellison and Turner (1959) with $Re \sim 10^3$. It is important to note that entrainment occurs under subcritical conditions ($Fr < 1$), which is supported by oceanic observations, by our experimental results and from Cenedese *et al.* (2004) (cf. Figure 4.2) and also confirmed by field data from Fernandez and Imberger (2006), Elder and Wunderlich (1972) and Hebbert *et al.* (1979).

The entrainment parameter obtained for the performed runs, with kinematics nevertheless different from the gravity currents whose results are shown in Figure 4.2, agrees well with previous results, in particular with the entrainment estimations of Cenedese and Adduce (2008). Bed roughness seems to play a role since a clear deviation of run R3, performed with higher roughness scale (cf. Table 2.3), from the remaining runs is detected. Runs R1 and R2, with lower roughness scale, do not show significant difference from the smooth bed run D2, with same initial buoyancy, suggesting that the scale of the bed roughness, and possibly porosity, are parameters that influence current kinematics and, therefore, needs further investigation.

4.3.2 Head dynamics

4.3.2.A Head definition

In order to assess local parameters at the current head, a criterion to isolate this region was established in subchapter 3.3.6 by defining the function W (Eq. 3.4), given by the product between local values of depth-averaged density, ρ_d, and current height, h. The downstream limit of the head is given by the position of the foremost point of the current, being the upstream limit, and consequently the head length L_h, defined by taking the position of the first meaningful local minimum of function W, near the front. Figure 4.3 complements the scheme presented in Figure 3.13, where additional head variables are included. The mass of the head of the gravity current per unit width, M_h, is then evaluated by integrating function W over the head length, L_h, given by:

$$M_h(t) = \int_{x_f(t)-L_h(t)}^{x_f(t)} W(x,t)\mathrm{d}x \tag{4.3}$$

where $x_f(t)$ is the position of the foremost point of the current.

4.3.2.B Front velocity

The time-varying front velocity of the gravity current, $u_f(t)$, was obtained by derivation in time of the regression functions adjusted to the front position (cf. Chapter 3). Generally, two distinct

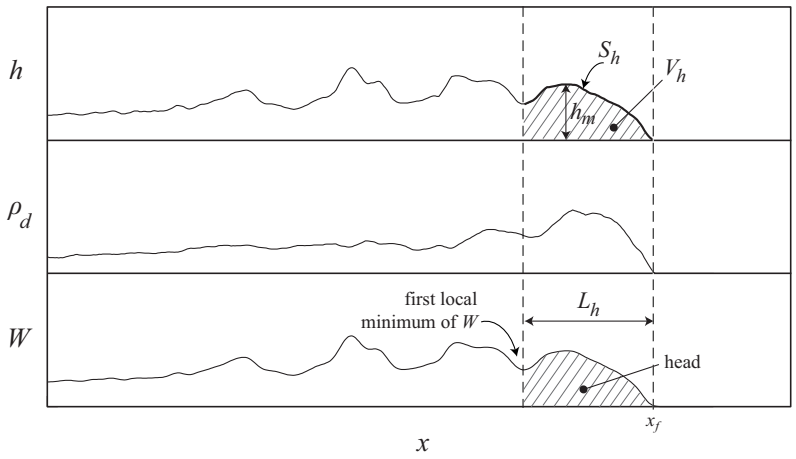

Figure 4.3: Definition of the density current head and its characteristic variables: maximum height, h_m, area of the permeable interface per unit width, S_h, volume per unit width, V_h, length, L_h, and front position, x_f

phases were observed for the development of the current: i) first phase, or slumping phase, characterized by a linear relation between front position and time after the gate removal and ii) second phase, or self-similar phase, in which the current moves under the balance between buoyancy and inertial forces, being the front position an evident nonlinear function of time; the transition between both phases was seen to occur at $x_f/x_0 = 9.4 \pm 1.0$, corroborating previous observations (Rottman and Simpson 1983). No viscous phase was observed in the performed experiments due to geometric limitations of the experimental tank.

During the slumping phase, the normalized front velocity (by u_0, Eq. 2.6) was obtained in the range $u_f/u_0 = 0.46 \pm 0.02$, values slightly higher than the predictions of the DNS model by Cantero *et al.* (2008), $u_f/u_0 = 0.42$, and below the theoretical predictions of Benjamin (1968), $u_f/u_0 = 0.527$ for an average current height of $h_b/h_0 = 1/3$. For the self-similar phase, the normalized front velocity was seen to decrease with time as $t^{[-0.19,-0.27]}$, decreasing rates lower than the predictions in literature ($t^{-1/3}$, Rottman and Simpson (1983), Cantero *et al.* (2008)).

Froude number assessed locally at the head, defined in Eq. 3.3, with the characteristic depth given by the maximum height of the current head, h_m (cf. Figure 4.3), is here referred as Fr_h for notation simplification purposes. During the constant-velocity phase, Fr_h exhibits some scatter which is reduced in the self-similar phase, where a narrow collapse around $Fr_h = 0.9$ is obtained (cf. Figure 3.14). Run R3 deviates from the general trend, assuming, in general, lower Froude numbers than the remaining runs; a decreasing trend is observed in the early stages of the current development, evolving towards a plateau of $Fr_h = 0.6$ after $(x_f - x_0)/x_0 = 9$ (cf. Figure 3.15).

At the early stage no apparent head detached from the remaining current is observed and buoyancy effects are given by the total body, thus evolution is governed by the bulk movement of the denser mass stored in the lock. This may explain the scatter in Froude numbers for $(x_f - x_0)/x_0 < 9$, justifying the bulk character of the current propagation at this stage and that local parametrization may not be adequate here. During the second phase, when the reflected bore catches the front of the current (cf. Rottman and Simpson 1983), the current is clearly fragmented into a body and a well defined head with own momentum penetrating in the ambient fluid. The front velocity is determined by this detached head being in equilibrium with its buoyancy celerity. These observations suggest that after the constant-velocity phase current kinematics are ruled by the current head, i.e., the remaining body of the current does not seem to play an important role in the current development.

4.3.2.C Head variables

Figure 4.4 shows the temporal evolution of the head mass per unit width, M_h, plotted as function of dimensionless time, tu_0/x_0, after the gate removal.

Remarkable patterns characterized by successive events of stretching and break of the head are observed (cf. Figure 4.4, run D2). Similar behavior was observed when analyzing other variables computed at the head, namely L_h, S_h and V_h, presented in Figures 4.5 to 4.7. During the stretching phase, a general increase of the head is observed due to entrainment of ambient fluid into the head region. These observations suggest that entrainment at the head is present throughout its development, inclusively in the early stages (in agreement with the observations of Hacker *et al.* (1996), consequently deviating from the theory of Hallworth *et al.* (1996)), where a faster rate of increase of both head length and mass is observed. The break cycles show that a limit exists in the entrainment capacity of the head, indicating an instability process eventually controlled by a dynamical quantity. After this limit is reached, the head breaks leaving behind quasi-steady large-scale billows, which eventually fade in time by diffusion-type processes. This is visible in Figure 2.9, following the evolution of the billow structure at positions $(x-x_0)/x_0 = 7.0$, 8.0 and 8.5 (at t =20, 28 and 36 s, respectively). A detailed characterization of the stretching cycles, namely their periodicity and the analysis of the evolution of head variables during stretching, is presented in section 4.3.4.

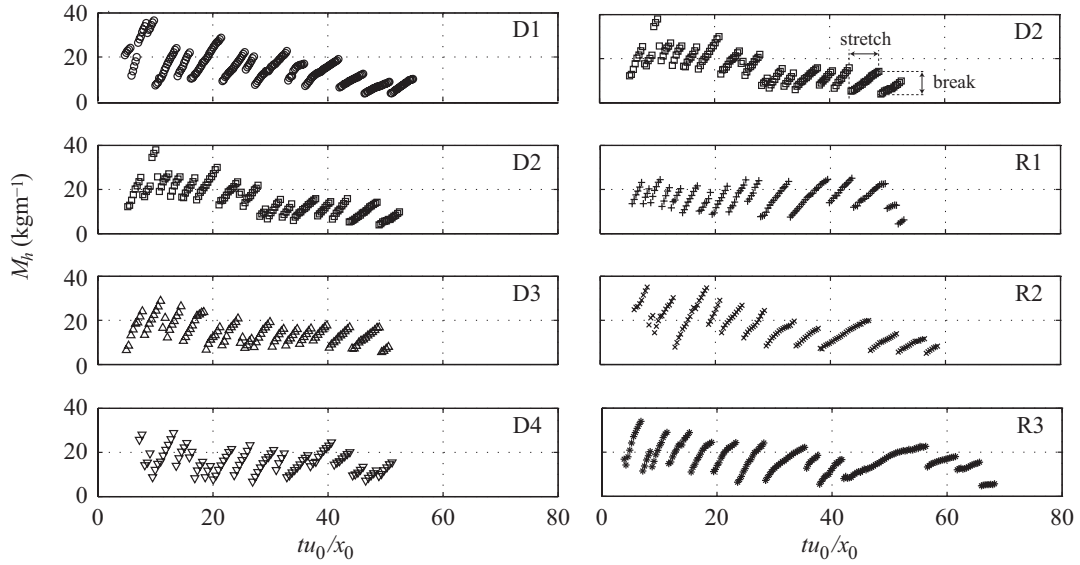

Figure 4.4: Mass per unit width of the gravity current head, M_h, as function of non-dimensional time.

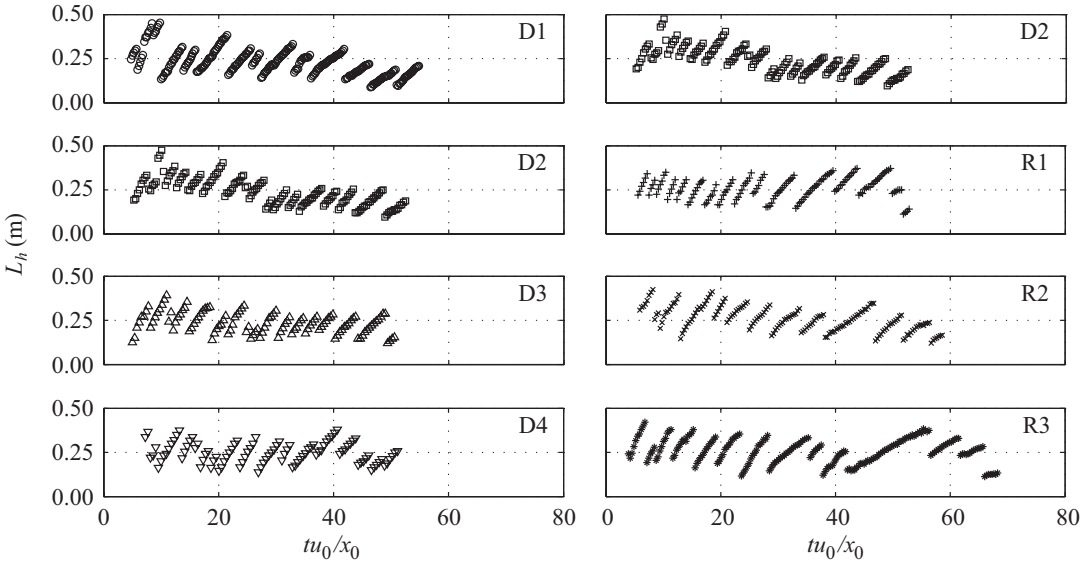

Figure 4.5: Length of the gravity current head, L_h, as function of non-dimensional time.

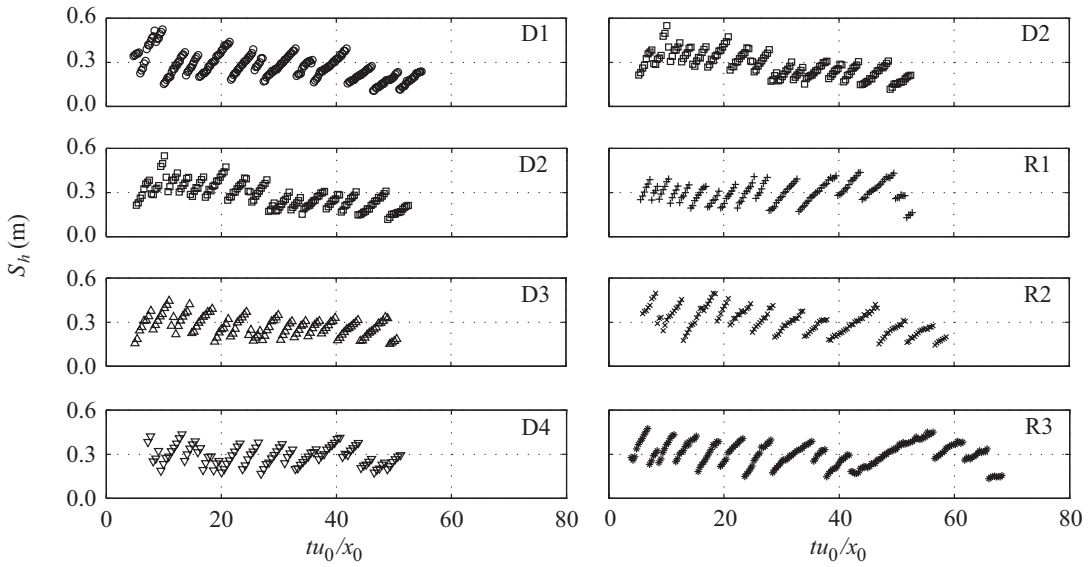

Figure 4.6: Area of permeable surface per unit width of the gravity current head, S_h, as function of non-dimensional time.

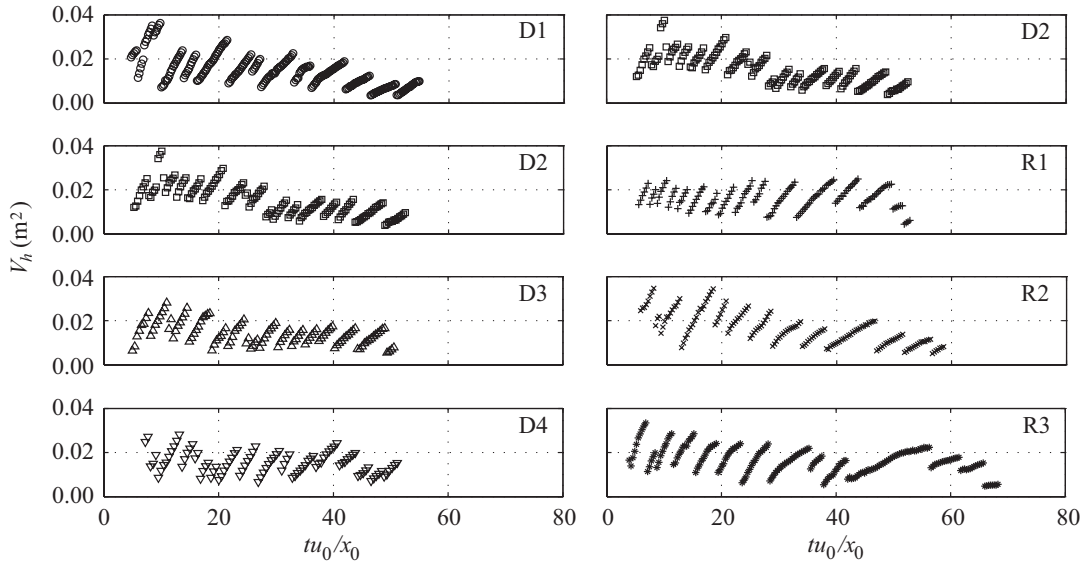

Figure 4.7: Volume of the gravity current head per unit width of the gravity current head, V_h, as function of non-dimensional time.

4.3.3 Head entrainment

4.3.3.A Entrainment parameterization

Entrainment parameter at the head, E_h, was estimated for each stretching phase (cf. section 4.3.2.C) by analogy to E_b (Eq. 4.1), being the initial and final sections considered corresponding to the begin and end of each stretching phase, respectively, leading therefore to one value of E_h for each phase.

Figure 4.8 shows the entrainment discharge at the head per unit width, $Q_{e,h}$, obtained by computing the variation of volume of the head during each stretching phase, normalized by bulk entrainment discharge earlier estimated, Q_e, as function of non-dimensional time tu_0/x_0. The ratio $Q_{e,h}/Q_e$ shows that entrainment discharge at the head is significantly higher than its bulk estimation for the entire current. In general, the entrained discharge decreases in time as expected given the results presented in Figure 4.4, where it is shown that the slope of M_h in each stretching phase tends to decrease in time. In the early stages of current development, i.e., for $tu_0/x_0 < 20$ approximately, the ratio $Q_{e,h}/Q_e$ is, in average, $Q_{e,h}/Q_e \approx 3$, thereafter it decreases linearly, until $tu_0/x_0 = 40$, converging to $Q_{e,h}/Q_e = 1$. For later instants, the ratio remains approximately constant and equal to 1. A good data collapse between runs is observed except for run R3, which shows, in average, a ratio $Q_{e,h}/Q_e$ twice the value for the remaining runs during most part of the current development, converging nevertheless to $Q_{e,h}/Q_e = 1$ for $tu_0/x_0 > 40$.

The entrainment velocity, $u_{e,h}$, was computed in analogy to Eq. 4.2, considering the entrained discharge over the permeable surface of the head, S_h, averaged over each stretching phase, and is presented in Figure 4.9 normalized by bulk entrainment velocity earlier estimated, u_e. The ratio $u_{e,h}/u_e$ shows that the entrainment velocity at the head is much higher than the bulk entrainment velocity u_e, being in average $u_{e,h} \approx 30u_e$ in the beginning of a run, reducing to $u_{e,h} \approx 12u_e$ at the end. The entrainment velocity follows the same trend of $Q_{e,h}$, generally decreasing over time. Again, run R3 stands out, showing a ratio of twice that of the remaining runs, nevertheless converging to $u_{e,h} \approx 12u_e$ as the experiment continues.

Figure 4.10 presents the entrainment parameter estimated at the head normalized by bulk entrainment parameter, E_b. The ratio E_h/E_b shows an approximately constant trend over time, oscillating around $E_h/E_b \approx 20$ with some significant scatter. Values of this ratio corroborate what was observed previously in Figs. 4.8 and 4.9, allowing the conclusion that entrainment at the head is more intense than in the current as a whole.

On Figure 4.11, E_h versus densimetric Froude and Reynolds numbers computed at the head of the current are plotted. Local densimetric Froude number, Fr_h, was computed by Eq. 3.3 and local Reynolds number, Re_h, was assessed through $Re_h = u_f h_m/\nu_a$, being subsequently averaged within each stretching phase. Densimetric Froude number show that the head region develops under critical flow conditions since data is distributed in a cloud around $Fr_h \approx 1$. Figure 4.11 center and right plots show that, although the main tendency is to have an increase of entrainment with increase of Re_b and $Fr_b Re_b$, no clear dependence of E_h on Re_h or $Fr_h Re_h$ seems to exist.

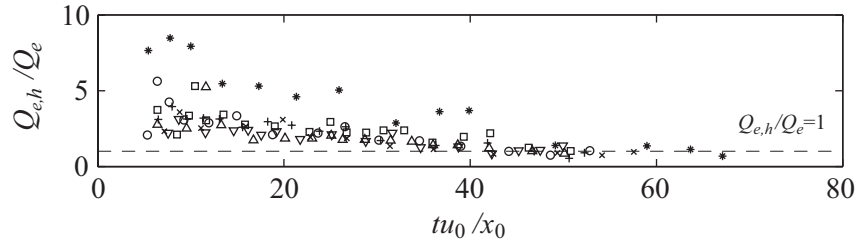

Figure 4.8: Entrainment discharge at the head normalized by bulk entrainment discharge as function of non-dimensional time, one value per stretching phase (symbols explained in Table 2.3).

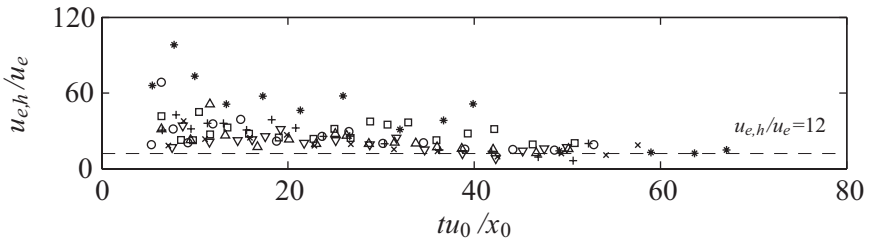

Figure 4.9: Local entrainment velocity normalized by bulk entrainment velocity as function of non-dimensional time, one value per stretching phase (symbols explained in Table 2.3).

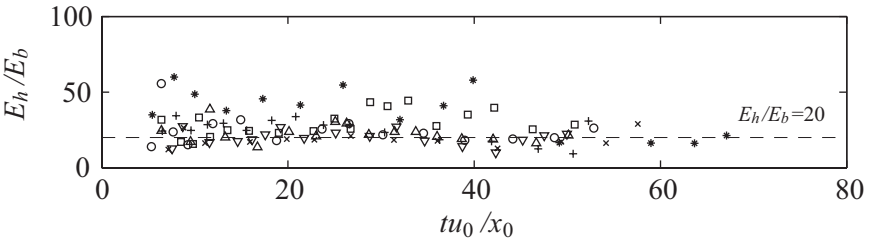

Figure 4.10: Entrainment parameter at the head normalized by bulk entrainment parameter as function of non-dimensional time, one value per stretching phase (symbols explained in Table 2.3).

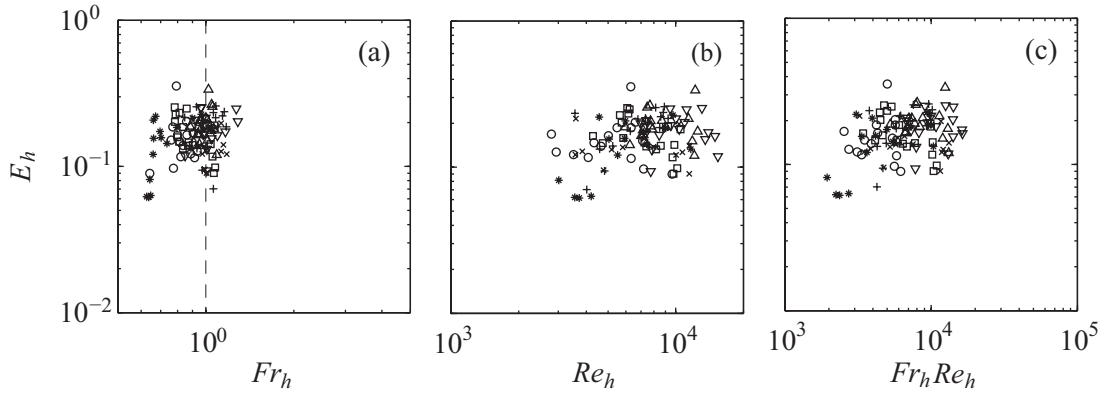

Figure 4.11: Entrainment parameter at the head as function of Fr_h (a), Re_h (b) and Fr_hRe_h (c) (symbols explained in Table 2.3).

4.3.3.B Mass rate

As shown in Figure 4.4, the mass of the gravity current head grows during each stretching phase due to entrainment of ambient fluid into this region, until it reaches a limit and breaks, from where it starts expanding again. The mass growing rate, or stretching rate, of the head can be analyzed by computing the variation of mass during each stretching event over time, i.e., $\mathrm{d}M_h/\mathrm{d}t$, herein taken as a measure to assess the entrainment rate at the head. This quantity is here normalized by the initial mass in the lock, M_{c_0}, resulting the parameter $M_h^* = \mathrm{d}M_h/\mathrm{d}tM_{c_0}^{-1}$. Time derivative was computed through application of second order centered finite differences to the experimental data $M_h(t)$, after applying a moving average ($N = 10$) to instantaneous data. Figure 4.12 shows the average of M_h^* over non-dimensional time, tu_0/x_0, for each stretching phase, for all runs. In general, the mass growing rate decreases as the current advances, suggesting that the entrainment rate at the head is ruled by local reduced gravity. As the current develops and ambient fluid is entrained into the current head, local reduced gravity, the driving force of the current, is reduced due to current dilution and, consequently, current decelerates leading to less fluid to be entrained at the current head. Figure 4.12 shows mass growing rates with a similar decaying trend between

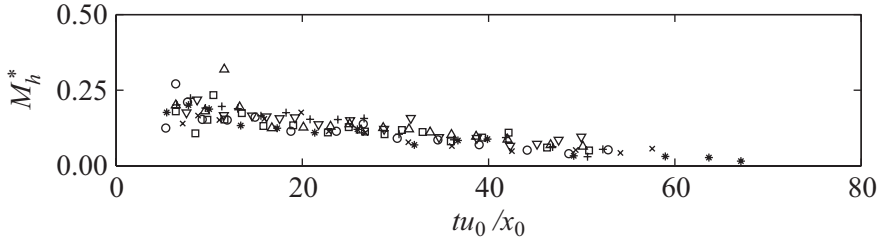

Figure 4.12: Non-dimensional mass rate as function of non-dimensional time (symbols explained in Table 2.3).

runs and their collapse suggests that temporal variation of mass inside the head poorly depends on initial density in the lock ρ_{c_0} and bed roughness k_s. In the authors opinion, the mass growing rate should tend to an equilibrium state (i.e. $M_h^* = 0$), not seen in these experiments due to geometric limitations of the experimental apparatus.

On Figure 4.13 the dependence of M_h^* on local densimetric Froude and Reynolds numbers, Fr_h and Re_h respectively, averaged over each stretching phase, is presented. In general, the dependence on Fr_h is not clear, except for run R3 where it exhibits an increasing trend with Fr_h. Densimetric Froude numbers oscillate around $Fr \approx 1$, suggesting that the head develops under critical conditions. On the other hand, M_h^* is an increasing function of Re_h. This results from the continuously decreasing trend of Re_h over time together with M_h^*. For high values of Re_h, M_h^* increases significantly, showing that mass transfer between current and ambient fluid due to turbulent phenomena is more effective than due to viscous effects, during the initial stages of the current development. For lower values of Re_h, there is a linear relation between M_h^* and Re_h. When plotting Fr_h and Re_h together, Fr_hRe_h, the linear dependence of M_h^* on Fr_hRe_h, for lower values of the latter, becomes evident. This is due to the effect of the local reduced gravity, $g\Delta\rho_h/\rho_{a_0}$, which highlights the similarity between runs. That linear phase corresponds to the final stages of the current development, where Re_h, M_h^* and Fr_h (although Fr_h not consistently), decrease. Both center and right plots in Figure 4.13 show that for high values of Re_h and Fr_hRe_h the dependence on Re_h seems to vanish, which is typical behavior of fully developed turbulent flows.

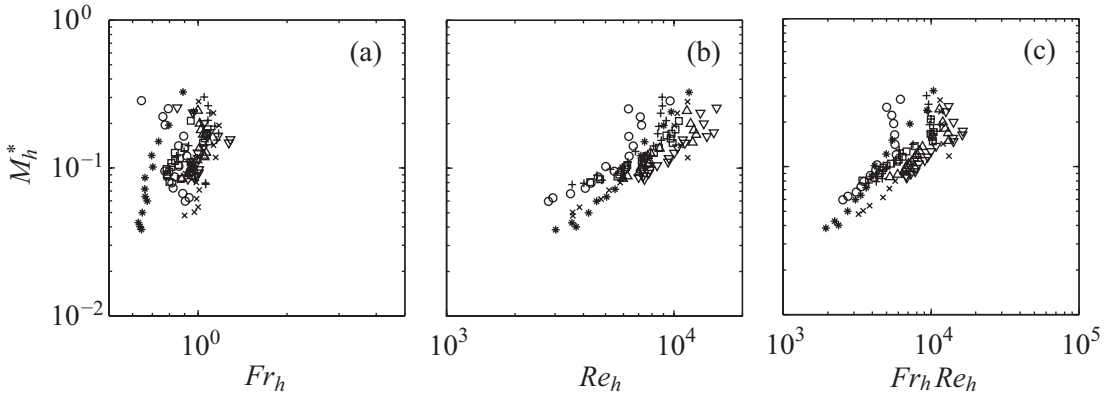

Figure 4.13: Non-dimensional mass rate as function of Fr_h (a), Re_h (b) and Fr_hRe_h (c) (symbols explained in Table 2.3).

4.3.4 Stretching characterization

Figure 4.14 presents the temporal evolution of the mass of the gravity current head normalized by the initial mass in the lock, M_h/M_{c_0}, and plotted as a function of dimensionless front position

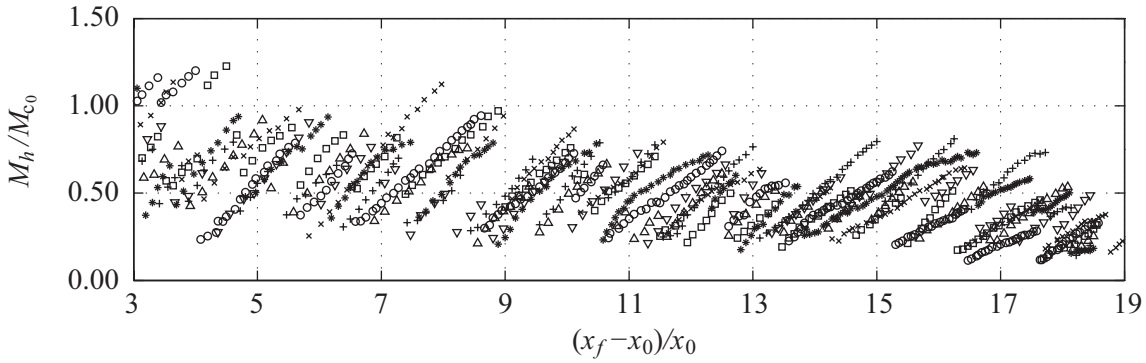

Figure 4.14: Non-dimensional mass per unit width of the gravity current head, M_h/M_{c_0}, as function of non-dimensional front position (symbols explained in Table 2.3).

$(x_f - x_0)/x_0$. Although the information is somewhat analogous to the one presented in Figure 4.4, the use of the of dimensionless front position highlights the similarity in the stretching events between runs. In general, limits of growth of M_h/M_{c_0} are more or less constant during the first phase of the current development when buoyancy overcomes inertial effects, i.e., for $(x-x_0)/x_0 < 9$ it varies approximately in the range limited by $0.2 < M_h/M_{c_0} < 1$, which means that the head tends to break when its mass reaches a value of the same order of that initially in the lock. During the second phase, i.e., for $(x - x_0)/x_0 > 9$, the ratio M_h/M_{c_0} tends to decrease as the current evolves.

In order to analyze the periodicity of the breaking events, Table 4.1 presents the average and maximum non-dimensional wave length, $\mathcal{L}^* = \mathcal{L}/x_0$, where $\mathcal{L}$ is the spatial distance between front positions of two successive breaking events and the average and maximum non-dimensional period between breaking events, $T^* = Tu_0/x_0$, being T the time between two successive breaks.

The average wave length is approximately constant between runs, $\mathcal{L}^* = 1.1 \pm 0.2$ (cf. Table 4.1), which is depicted by the similarity in the plots of Figure 4.14. The maximum wave length shows an increasing trend with bed roughness. The period of the breaking events, T^*, is

Table 4.1: Average and maximum normalized temporal (T) and spatial ($\mathcal{L}$) periodicity of breaking events

Run	$\overline{T^*}$	T^*_{max}	$\overline{\mathcal{L}^*}$	$\mathcal{L}^*_{max}$
D1	3.3	5.9	1.1	2.0
D2	2.5	5.2	0.9	1.5
D3	2.7	5.5	0.9	1.8
D4	2.6	4.2	0.9	1.6
R1	3.0	6.8	1.0	2.0
R2	4.1	8.8	1.3	2.3
R3	4.6	14.4	1.2	2.9

quite irregular within a run (cf. Figure 4.4), where no consistent evolution trend is identified. However, the analysis of the average and maximum values of T^* show a tendency between runs (cf. Table 4.1). Regarding the effect of the initial density for smooth bed (runs D1, D2, D3 and D4), we observe that run D1, with lower initial density, has the highest average and maximum stretching periods. A significant decrease in the average periodicity is observed from run D1 to D2, which apparently stabilizes with the following increase of initial density. The effect of bed roughness can be observed by analyzing the sequence D2, R1, R2 and R3. The average period suggests that as the bed roughness increases, breaking events tend to occur less frequently and a temporal extension of the stretching phases occurs. A similar trend is observed when looking to the maximum period between breaking events; a remarkable increase in the maximum period (5.2, 6.8, 8.8, 14.4) is detected when increasing the bed roughness, trend also observed in the analysis of the maximum wave length $\mathcal{L}^*$.

The aspect ratio of height versus length, h_m/L_h, is plotted in Figure 4.15 for all runs. The aspect ratio of the head is seen to decrease during the stretching period, which is expected since the maximum height of the head has little variation over time while the head length increases continuously during stretching. However, there is a limit in the entrainment capacity of the head, shown by the breaks at $h_m/L_h \approx 0.2$. Britter and Linden (1980) suggested that the head aspect ratio of constant-flux gravity currents developing over horizontal beds is zero, as shown by Figure 8 therein. Nevertheless, the fit line presented for h/L_h as function of slope, based on results from their own experiments and previous ones, clearly indicates a trend towards 0.2 as the slope angle approaches zero. Özgökmen *et al.* (2004) presents a limit of $h/L_h = 0.2$, for numerical modeling in lock-exchange gravity currents down slope (3.5°), being 0.25 their average or trend. Hence, the limit given by the head aspect ratio, $h_m/L_h = 0.2$, is essentially a good criterion to predict

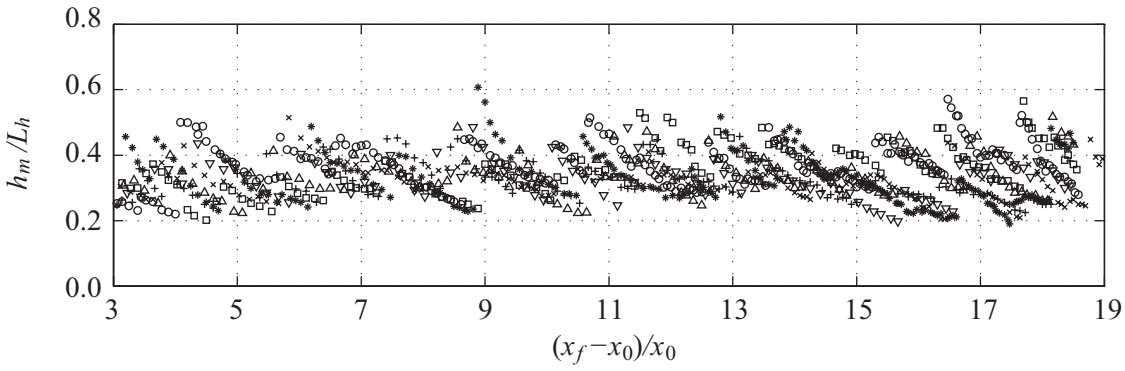

Figure 4.15: Head aspect ratio, h_m/L_h, as function of non-dimensional front position (symbols explained in Table 2.3).

the instant of head breaking, for unsteady currents developing over horizontal beds, or even, over small slopes.

To evaluate the similarity within stretching periods, a phase analysis is performed over one cycle of duration θ, varying from 0 to 1, where 0 is the begin and 1 the end of the stretching cycle. The collapse of the stretching cycles of the variables h_m/L_h, M_h/M_{c_0}, E_h/E_b and M_h^* were analyzed by plotting all cycles together, for each variable and for each run. A very good data collapse is observed, highlighting the similarity between stretching cycles for the variables under analysis. For comparison between runs, the phase average trend of each variable is analyzed. Given the different number of points in each stretching cycle, a sub-discretization of data over one cycle was adopted, taken the shortest temporal discretization within each run, which corresponds to the discretization of the stretching cycle with more data points. Then, values of variables under analysis are interpolated linearly in order to have one data point for each additional instant, being then possible to compute phase averages for each run.

Figure 4.16 shows phase-averaged values so obtained over each cycle of variables h_m/L_h, M_h/M_{c_0}, E_h/E_b and M_h^*. As already observed in the ensemble plots of the non-dimensional mass and of the head aspect ratio (Figs. 4.14 and 4.15, respectively), a high similarity of these variables between stretching cycles do exist which is highlighted in Figure 4.16(a,b). In average terms, the limit attained by the head aspect ratio, related to the end of the stretching phase/occurrence of break event, is around $h_m/L_h \approx 0.3$, corroborating previous experimental and numerical findings. Mean non-dimensional head mass vary in average between $0.25 < M_h/M_{c_0} < 0.75$. The ratio of local over global entrainment parameters, E_h/E_b (Figure 4.16c), also shows a good similarity between runs, clarifying the average trend around $E_h \approx 20E_b$, as already suggested in section 4.3.3. Also the deviation of run R3 becomes rather clear, approaching the overall trend of the remaining runs in the final stages of stretching. Finally, the evolution of M_h^* (Figure 4.16d) during stretching is seen to vary little. There is a general slight increase during the first half of the standard stretching duration, followed by a decrease during the second half. Run R3 exhibits this trend as well, although with a higher amplitude than the remaining runs.

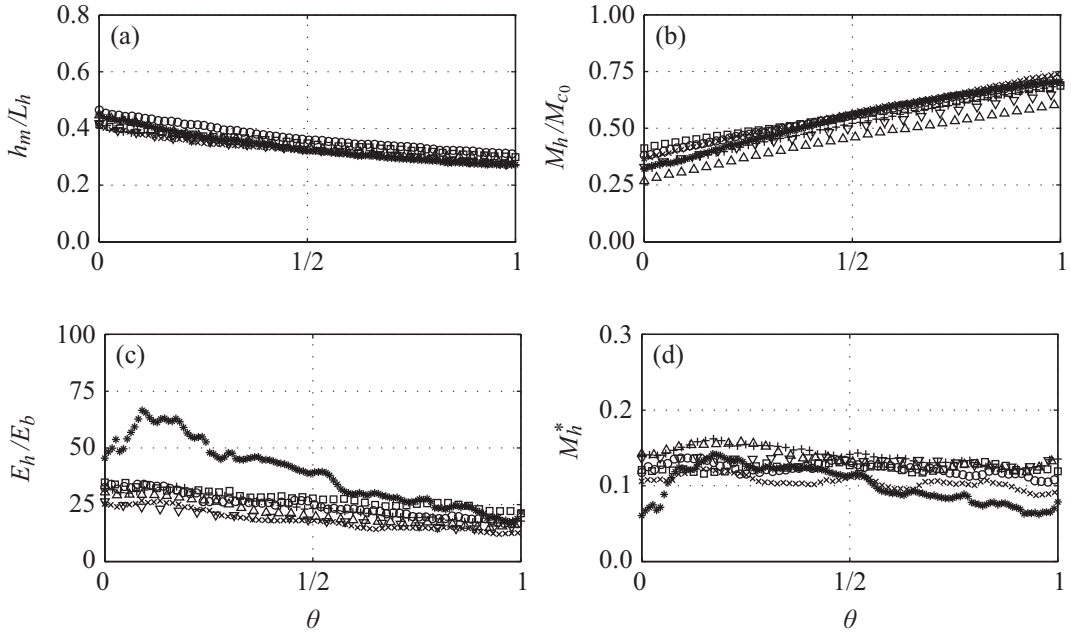

Figure 4.16: Phase-averaged variables as function of the duration of a stretching cycle, θ: (a) head aspect ratio, h_m/L_h; (b) non-dimensional head mass, M_h/M_{c_0}; (c) entrainment parameter at the head over global entrainment parameter, E_h/E_b and (d) non-dimensional mass growing rate, M_h^* (symbols explained in Table 2.3).

4.4 Conclusions

An image analysis technique was used to investigate the dynamics of the head of lock-released gravity currents developing over smooth and rough beds. The influence of the initial buoyancy of the gravity current on its development was assessed, as well as the influence of bed roughness.

Immediately after the release of the dense fluid inside the lock, a gravity current of heavy fluid forms near the bed and evolves towards downstream. During its development, the current mixes with the surrounding ambient fluid and continuously entrains part of it. The interaction between fluids is more dynamic in the head region and a notorious pattern of head stretching and break was herein observed. As the head entrains ambient fluid, its dimensions and mass increase accordingly, until it becomes unstable and, consequently, breaks. After breaking, the head leaves behind quasi-steady large-scale billows that remain at the rear of the head, promoting strong mixing in that region, which eventually fade in time by diffusion-type processes. The evolution of the head aspect ratio during the stretching period shows a consistent limit, for all performed runs, of $h_m/L_h = 0.2$, corresponding to the breaking instants. In addition, during these instants the mass of the gravity current head is seen to be of the same order of the mass initially in the lock, especially during the first phase of the current development. Bed roughness is seen

to play an important role in this process. As roughness increases, besides the expected current deceleration, the break events become less frequent. Similarity of the stretching events between runs is confirmed by the consistent collapse of the analyzed variables at the head.

The bulk entrainment parameter obtained for each run shows that entrainment occurs under subcritical conditions and its magnitude is in good agreement with entrainment predictions of Cenedese and Adduce (2008). Gravity currents with higher initial density are expected to have higher values of entrainment parameter. Regarding the influence of the bed roughness, only the run performed with higher roughness shows a clear deviation from the remaining runs, suggesting that roughness scale and porosity might play a role in the gravity current dynamics. The dependence on Froude and Reynolds numbers was also confirmed by our experiments. Entrainment parameter at the head was assessed for each stretching phase and was seen to be approximately 20 times higher the entrainment parameter obtained in a bulk fashion for the entire current.

The evolution of the mass growing rate at the head shows a decreasing trend in time, suggesting that local buoyancy rules the entrainment phenomenon. The entrained ambient fluid reduces the driving force of the current, due to current dilution, leading to less fluid to be entrained at the current head. Its similarity between runs suggests that this parameter is independent from the initial density gradient and the bed roughness. Both Froude and Reynolds numbers influence, naturally, the evolution of the mass growing rate. In particular, a linear increasing relation is observed for lower values of $Fr_h Re_h$, corresponding to later stages of the current development, when all the parameters in question decrease consistently. For high Reynolds numbers, entrainment increases significantly indicating a higher efficiency of turbulent-type processes in entraining ambient fluid when compared to viscous diffusion. The results presented herein indicate that entrainment at the head is present in gravity currents with densimetric Froude numbers below 0.7 and it was observed at all stages of the current development, including the early stages, where higher entrainment rates are observed.

Chapter 5

KINEMATICS OF GRAVITY CURRENTS BASED ON VELOCITY MEASUREMENTS

Contents

Chapter 5 is based on the paper 'Kinematic characterization of unsteady gravity currents developing over smooth and rough beds' submitted for publication by the authors H.I.S. Nogueira, C. Adduce, E. Alves and M.J. Franca, and based on the preliminary results presented in Nogueira et al. *(2012d). It presents the main results arising from the velocity measurements performed through Particle Image Velocimetry. General kinematics of the current are described, whereas a detailed analysis of the two quasy-steady flow regions of streamwise velocity is presented.*

Abstract

Gravity currents performed through lock-release of a brine solution into a fixed volume of fresh water, in a rectangular cross-section Perspex tank, are herein investigated. Four experiments are performed by changing the roughness of the bed material, maintaining constant all other experimental variables. Particle Image Velocimetry is used to measure the instantaneous velocities of the flow in a vertical plane positioned along the tank centerline, allowing the visualization and characterization of the velocity, vorticity and turbulence fields. Gravity currents here performed are in the inertial phase of development when entering the visualization window. The main characteristics of the flow field were assessed for the quasi-steady streamwise flow regions detected within the head and the body of the current. The flow in these regions result from the interaction between the mean flow and the flow structures generated in both bottom and interfacial shear layers. As the gravity current head passes, the effect of the interfacial shear layer vanishes due to overall reduction of streamwise velocity, being the flow mainly dominated by the bottom generated vorticity. Bed roughness is seen to reduce the front velocity and the streamwise velocity within the current, due to extra drag induced by the roughness elements, and to homogenize the velocity distribution within the current, reducing the maximum velocity gradient. Striking differences are observed in the velocity and vorticity fields between gravity currents developing over smooth bed and over the highest bed roughness tested, confirming that the size and porosity of the bed material play a role in the gravity current kinematics.

5.1 Introduction

The use of non-intrusive techniques to measure the flow velocity, such as laser Doppler anemometry (LDA) or velocimetry (LDV) (Kneller *et al.* 1997, 1999) and particle image velocimetry (PIV) (Alahyari and Longmire 1996, Zhu *et al.* 2006, Adduce *et al.* 2011, Lopes *et al.* 2013), allowed

the visualization and characterization of the velocity field and structure of turbulence of gravity currents. The combination of PIV with other methods, such as laser-induced fluorescence (PLIF) (Martin and García 2009) and scalar PIV (PIV-S) (Ramaprabhu and Andrews 2003, Gerber *et al.* 2011), allows the measurement of velocity and density simultaneously. Alahyari and Longmire (1996) used PIV to investigate the dynamics of the head of unsteady axisymmetric gravity currents in the inertia-buoyancy phase of the flow. They observed two counter-rotating large-scale vortices at the current head in the instantaneous velocity maps, which persist after ensemble-averaging over several realizations. Those vortices are seen to accelerate the flow in between, inducing current dilution and consequent reduction of the flow velocity. Kneller *et al.* (1997, 1999), through velocity measurements with LDA in lock-exchange saline currents in the slumping phase, analyzed the mean flow in the current head and body, as well as the turbulent structure. Two regions of negative Reynolds stresses were observed in the current head: beneath the nose and in the upper boundary, at the rear of the head; both regions are related to ambient fluid incorporation by the current. Large eddies generated in the upper shear layer are seen to dominate the turbulent kinetic energy budget throughout the flow. Thomas *et al.* (2003) used particle-tracking velocimetry (PTV) to study gravity currents during the slumping phase, with Reynolds numbers varying in the range from 120 to 4000. Based on time-averaged velocity fields they observed the existence of two counter-rotating cells in the current head, whose location was seen to depend on the Reynolds number. Gerber *et al.* (2011) investigated the turbulent structure of the body of steady, continuously fed, saline currents with Reynolds number of 2300 using scalar particle image velocimetry (PIV-S). They discuss the distribution of velocity and brine concentration within the current, as well as the turbulent structure of the flow, also comparing with results given by RANS numerical simulations.

Most of the research efforts in the visualization and characterization of the flow field of gravity currents concern flows developing over smooth beds. Few contributions have studied the effect of bed roughness in the dynamics of gravity currents (Peters and Venart 2000, La Rocca *et al.* 2008, Özgökmen and Fischer 2008, Adduce *et al.* 2009, Nogueira *et al.* 2013a), showing that roughness decreases the front velocity and induce higher dilution in the head region, the latter depending on the scale and porosity of the roughness material (Nogueira *et al.* 2013a). Despite all the research efforts, there is a lack of information of the bed roughness effect on the structure of gravity current flows.

The experiments herein presented complement the analysis presented in Chapters 5 and 4,

where lock-release gravity currents were performed over smooth and rough beds. In these, the density field was assessed through an image analysis technique, allowing the description of the kinematics and dynamics of these currents. This work aims at contributing to the characterization of the inner velocity, vorticity and turbulent structure of similar currents and to assess the effect of the bed roughness on the distribution of the referred fields within the current through PIV measurements.

After this introduction, experimental details are given in section 5.2, general characteristics observed in the performed currents are presented in section 5.3, section 5.4 presents and discusses the main results, being section 5.5 devoted to the main conclusions.

5.2 Experimental setup

The experiments were performed in the experimental tank defined in Chapter 2. A saline mixture of initial density ρ_{c_0} was placed in a lock with a vertical sliding gate at a distance $x_0 = 0.15$ m from the upstream section, i.e., left wall of the tank (cf. Figures 2.2 and 2.1). The right side of the tank was filled with water with density ρ_{a_0}. In the experiments with bed roughness, the depth of the saline mixture in the lock, h_0, was measured from the top of the bed crests. Further details of the experimental procedure can be consulted in Chapter 2.

The location of the visualization window, starting from $x = 1.50$ m as shown schematically in Figure 2.10, in terms of lock-lengths is $(x-x_0)/x_0 = 9$, which corresponds to the transition between the slumping and inertial phases of lock-exchange currents, predicted in Rottman and Simpson (1983) and confirmed by our experiments (cf. Chapter 3). However, for currents developing over rough beds, and depending on the roughness scale and porosity of the material, the transition between phases may occur earlier, as shown by our results, due to a fast deceleration and dilution of the current induced by extra resistance of the bed. Thus, gravity currents here performed are in the inertial phase of development when entering the visualization window.

Four experiments were performed by changing the bed roughness k_s, maintaining constant all other variables. Table 2.3 summarizes the parameters of the experiments and the symbols used in the figures. Brine and water have different refractive indices which leads to the deviation of the laser light sheet when crossing the interface of both fluids. This was observed in the performed experiments and only with the lowest excess density tested, $\Delta\rho$ =17 kg·m^{-3}, the particles had sufficient definition for velocity measurement purposes, as shown in Figure 2.12 and below in

Figure 5.1 (see section 2.4 for more details). The latter shows snapshots of the current for run R3 acquired at four different stages after the gate removal (t = 24.3, 27.7, 29.7 and 34.3 s), where the individual seeding particles can be distinguished. The definition of the boundary of the current shown in Figure 5.1 is explained later in the text.

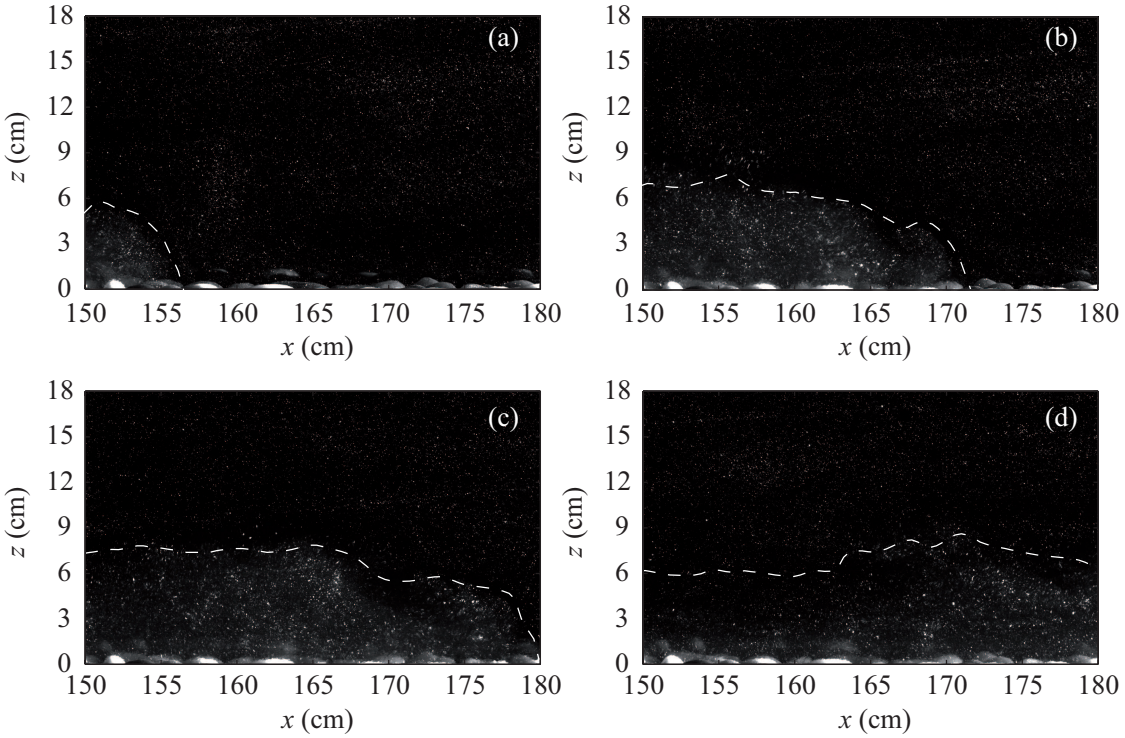

Figure 5.1: Frames acquired at (a) t = 24.3, (b) t = 27.7, (c) t = 29.7 and (d) t = 34.3 s after the gate removal in run R3.

The fast removal of the lock gate induces oscillations in the water surface with a well defined narrow-band signature in the velocity field. A Butterworth filter of 5^{th} order was used to attenuate oscillations with frequency in the range 0.20 to 0.25 Hz in both velocity components. Additional details on the filtering procedure are presented in Appendix A.

As predicted in the literature, and corroborated by the results in Chapter 3, when the current enters the visualization area it is in the inertial phase in which the front position varies non-linearly with time. The front position, x_f, can be estimated by a power-law presented in Eq. 3.1, where β_i are the coefficients obtained by a least-squares regression, where the coefficient of determination, r^2, was used to evaluate the goodness of fit. In the analysis presented here, the values of β_1 and β_2 adopted are the ones presented in Chapter 3 for gravity currents with comparable excess density performed over smooth bed. The parameters $\beta_1 = 0.74$ and $\beta_2 = 0.81$ obtained therein (used later in the text) were seen to describe well the temporal evolution of the current front position in runs R0 and R1, for the instants in which the current front is visible in the visualization window. For runs

R2 and R3 a slight adjustment in the coefficient β_2 was necessary to improve the adjustment by the power-law, leading to the values 0.79 and 0.76, respectively. In conclusion, the values obtained for the coefficients β_1 and β_2 are: $\beta_1 = [0.74, 0.74, 0.74, 0.74]$ and $\beta_2 = [0.81, 0.81, 0.79, 0.76]$, with the corresponding values of $r^2 = [0.94, 0.94, 0.95, 0.98]$ for runs [R0, R1, R2, R3], respectively.

5.3 General characterization of the flow

Figure 5.2 shows instantaneous maps of the flow velocity, u and w components, the vorticity component normal the plane of measurement, η, and the Okubo-Weiss parameter, OW, for the instant the current reached the limit of the window of visualization (29.7 s after the gate removal) for run R3 (cf. Figure 5.1). The characterization of the flow field is here presented for this selected run but the general characteristics of the flow are common to the remaining runs.

The vorticity component normal to the measurement plane is obtained through:

$$\eta = \frac{\partial w}{\partial x} - \frac{\partial u}{\partial z} \tag{5.1}$$

The algorithm used to estimate the spatial derivatives in the definition of η is the one proposed by Sveen (2004), Raffel *et al.* (2007):

$$\left.\frac{\partial w}{\partial x}\right|_{i,j} = \frac{2w_{i+2,j} + w_{i+1,j} - w_{i-1,j} - 2w_{i-2,j}}{10\Delta x} \tag{5.2}$$

$$\left.\frac{\partial u}{\partial z}\right|_{i,j} = \frac{2u_{i,j+2} + u_{i,j+1} - u_{i,j-1} - 2u_{i,j-2}}{10\Delta z} \tag{5.3}$$

where i and j are the streamwise, x, and vertical, z, coordinates of the measuring point, respectively, Δx and Δz being the distances in both directions between adjacent points. This algorithm excludes the two-pixel region throughout the border of the image, therefore no vorticity information for this region is presented. The boundary between current and ambient fluid is also presented in the plots of Figure 5.2 and it was obtained by considering the condition $u = 0$ for the upper limit and $\partial w/\partial x = 0$ for the frontal limit, using the approximation for the partial derivative given by Eq. (5.2). This boundary definition is considered throughout the manuscript.

The Okubo-Weiss parameter is used to distinguish the regions dominated by rotation and strain

within the flow. This parameter is defined as (Okubo 1970, Weiss 1991):

$$OW = \gamma^2 - \eta^2 \tag{5.4}$$

where $\gamma^2 = \gamma_n^2 + \gamma_s^2$, γ_n being the normal component of strain, $\gamma_n = \partial u/\partial x - \partial w/\partial z$, while γ_s is the shear component, $\gamma_s = \partial w/\partial x + \partial u/\partial z$. Regions dominated by vorticity are then characterized by high negative values of OW, while high positive values for this parameter highlight strain-dominated regions. The threshold $OW_0 = 0.2\sigma_{OW}$, with σ_{OW} being the standard deviation in the whole domain, is usually adopted to isolate the regions dominated by strain ($OW > OW_0$) and the regions dominated by vorticity ($OW < -OW_0$) (cf. Isern-Fontanet *et al.* 2004) .

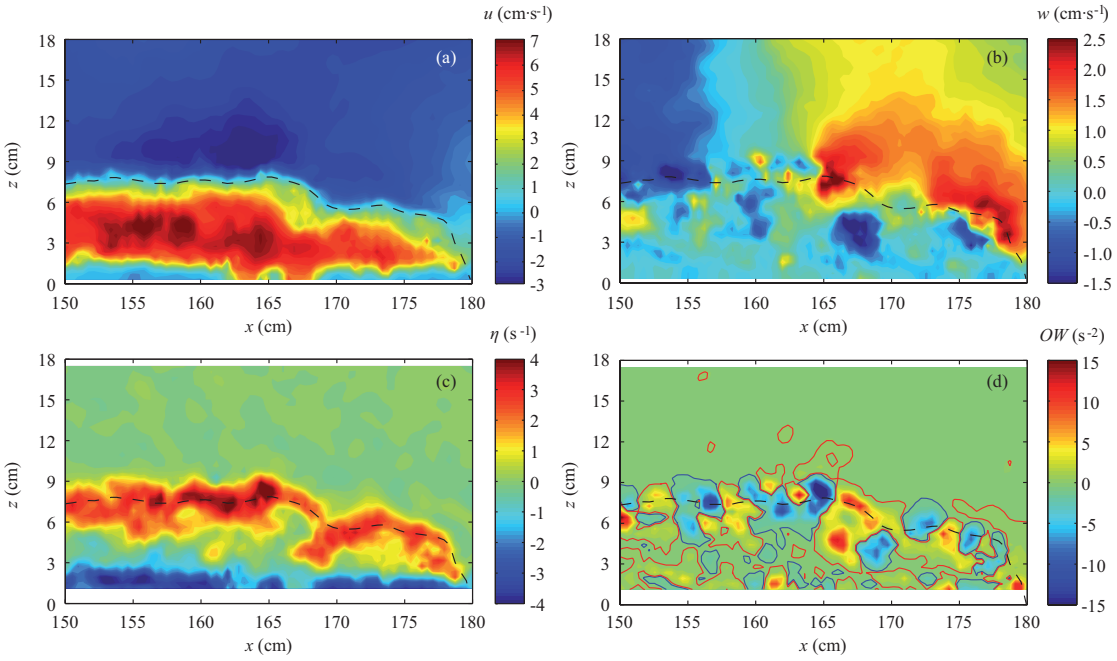

Figure 5.2: Flow maps with the current development at $t = 29.7$ s after the gate removal in run R3 (cf. Figure 5.1c): (a) streamwise velocity field, u; (b) vertical velocity field, w; (c) vorticity field, η and (d) Okubo-Weiss parameter, OW.

The flow in the current head is three-dimensional and its complex pattern results from the interaction between the mean flow and the flow structures that are generated in both bottom and interface shear layers. The frontal region of the current is characterized by low streamwise velocity (Figure 5.2a), whereas the vertical component of velocity is rather strong in that region (Figure 5.2b), indicating that there is a generalized upward flow in front of the current, in accordance to the observations by Zhu *et al.* (2006), Kneller *et al.* (1997, 1999). The flow displaced upwards is then incorporated by the countercurrent flowing in the upstream direction, above the heavier

current. The streamwise velocity field shows that the region of u maximum is not located near the front but rather upstream, under the region of intense vortex generation (155 cm $< x <$ 165 cm, 15 cm from the front); the vortical structures in the interfacial shear layer rotate counterclockwise, accelerating towards downstream the flow below, within the current. By continuity, the ambient fluid above is accelerated towards upstream, reaching its maximum in the region at z = 10 cm, 155 cm $< x <$ 165 cm (Figure 5.2a). At the rear of these vortices (150 cm $< x <$ 155 cm), ambient fluid is then incorporated by the current, as shown by the downward flow in that region. The upward flow has greater magnitude than the downward flow, reaching 30 to 40 % of the instantaneous $u_{\max}$, while the maximum downward flow is of the order of 20 to 30 % of $u_{\max}$. The vertical velocity field within the current is near zero in most of the captured area (Figure 5.2b). Possibly due to limitations in the experimental technique in capturing the flow near the bed, it was not here observed ambient fluid trapped inside the roughness layer being overridden and incorporated by the current.

In general, two regions of opposite vorticity are observed in Figure 5.2(c): a region of positive vorticity characterizes the interface between current and ambient fluid, resulting from shear between two flows in opposite directions, while near the flow bed a region of negative vorticity arises, resulting from the shear between upper flow and low velocities in the tank bed. The vorticity magnitude is comparable in both regions. Regarding the layer thickness, δ_η, the interfacial shear layer is generally thicker than the bottom layer, spanning over a region of 6 cm $< \delta_\eta^+ <$ 8 cm, while the bottom layer occupies the region 2 cm $< \delta_\eta^- <$ 5 cm near the bed. In the interfacial shear layer it is possible to distinguish several rotating cells (Figure 5.2c, 157 cm $< x <$ 165 cm), evidenced in Figure 5.2(d) by the dark blue regions. These eddies are generally surrounded by strain-dominated regions, as shown by the red areas in Figure 5.2(d), where mixing between dense and ambient fluids is more intense, leading to current dilution.

Figure 5.3 shows the temporal evolution of the instantaneous velocity components, streamwise u and vertical w, in run R3, at x = 165.2 cm for three different vertical locations: z = 3.3, 7.4 and 12.3 cm. The arrival of the current is clear in all locations under analysis and its effect is felt throughout the fluid depth. Within the current (z = 3.3 cm, Figure 5.3c) this is evidenced by a generalized increase in both velocity components starting from $t \approx$ 24 s. As already seen in Figure 5.2(c), the ambient fluid in front of the current is mainly displaced upwards as the current front approaches. After the frontal interface has passed, the vertical velocity component starts to decrease until t = 27 s, followed by a period of oscillation around zero during the passage of the

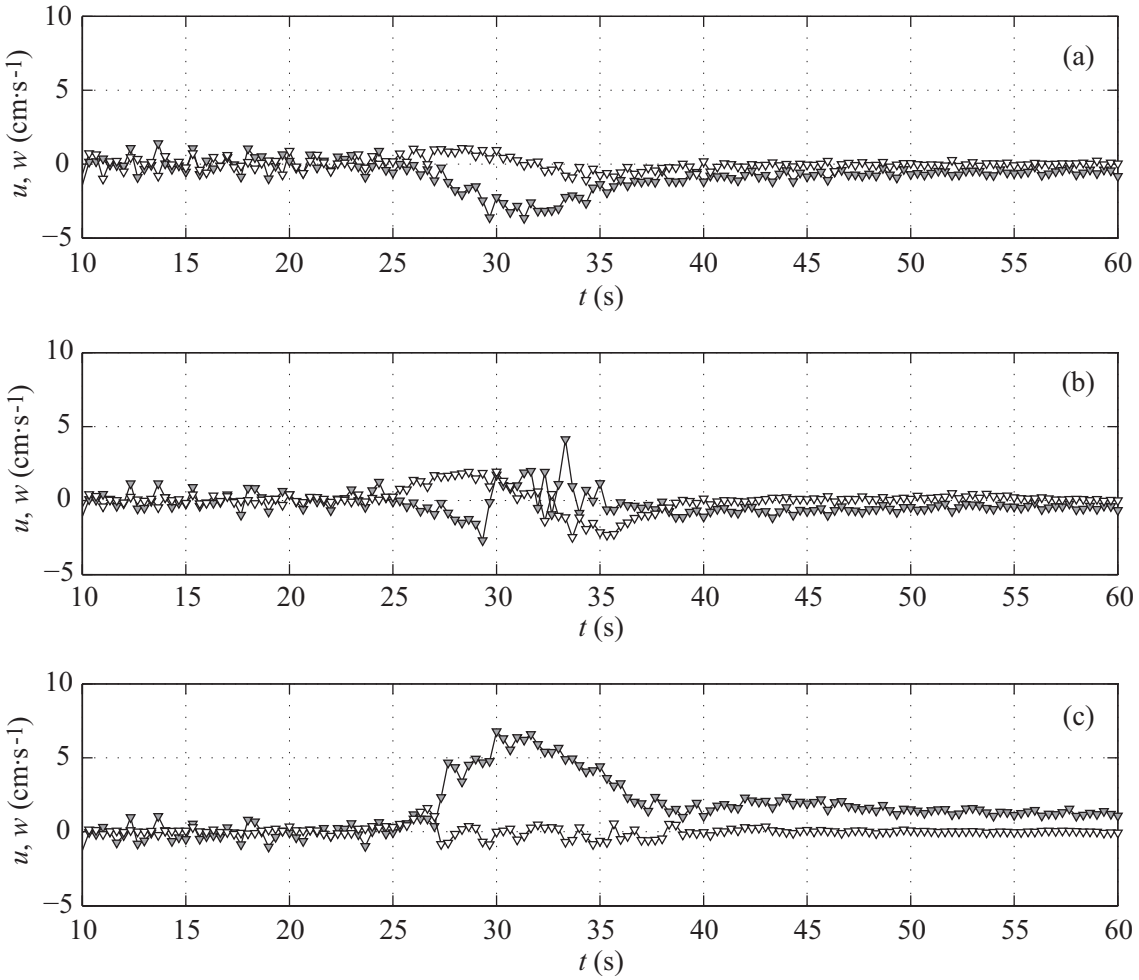

Figure 5.3: Time series of instantaneous velocity components u (filled symbols) and w (open symbols) in run R3 in measuring points located at (a) (x, z) = (165.2,12.3) cm; (b) (x, z) = (165.2,7.4) cm and (c) (x, z) = (165.2,3.3) cm.

current head. This alternating vertical flow results from the vortical activity within the current, which stabilized after t = 39 s. After the head passed, the vertical velocity at this location is practically negligible thenceforth. Regarding the streamwise component, during the passage of the head it increases until reaching a maximum at t = 29.7 s. A period of high streamwise velocity lasts for few instants from where it decreases gradually until $t \approx 40$ s. Then, a period of roughly constant velocity follows, seen by the plateau in u from t = 41 to 46 s; afterward, the streamwise component decreases continuously and asymptotically towards zero.

The position z = 7.4 cm (Figure 5.3b) is located in the upper shear layer during the passage of the current head (cf. Figure 5.2). The flow upwards and towards upstream verified between t = 24 and 29 s evidences the ambient fluid displaced upwards that is being incorporated by the countercurrent as above referred. After instant 29 s, the inversion of the vertical flow together with the sudden increase, and the following oscillation, of u shows that this point was crossed by

a vortex, leading to flow inwards the dense current. After t = 38 s the vortex and the current head in general have passed, and both velocity components tend to vanish.

Figure 5.3(a) shows the upper point analyzed, z = 12.3 cm, in which the flow behavior is similar to the point at the interface with the difference that the vertical flow is attenuated, the inversion between upward and downward flow being smoother and the streamwise velocity component showing mainly the counter current during the passage of the head. The maximum magnitude of the countercurrent occurs at the same time as the maximum streamwise flow within the denser current. After the head has passed, both velocity components tend to vanish.

5.4 Results

5.4.1 Mean velocity

In order to characterize the temporal evolution of the velocity field within the current, the mean flow velocity was computed by depth-averaging both velocity components, u and w, within the current with boundary, h, defined in section 5.3. The depth-averaged streamwise velocity, $u_d(x,t)$, is thus given by

$$u_d(x,t) = \frac{1}{h}\int_0^h u(x,z,t)\mathrm{d}z \tag{5.5}$$

where $u(x,z,t)$ is the local streamwise velocity. The mean vertical velocity, $w_d(x,t)$, was computed by analogy to Eq. (5.5). The time series $u_d(t)$ and $w_d(t)$, obtained for each streamwise location x visible in the measuring frame, are plotted in Figure 5.4 normalized by the buoyancy velocity. Within a run, each time series was shifted in time in order to align the time of arrival of the current front at each streamwise location, providing an inertial reference system for further analysis. Therefore, in Figure 5.4 two temporal axis are presented for each run: the bottom scale, t, presents the time after the gate removal, the series being aligned by the time the current arrived at the window of visualization, i.e., horizontal position x = 150 cm (cf. Figure 2.10). This scale is useful to visualize the difference in the front velocity among runs, where it is clear the influence of the bed roughness: as roughness increases the current front travels with lower velocity, reaching the visualization area at later times. The scale at the top, t_{rel}, represents the time relative to the instant of the current arrival, which serves to track the evolution of the depth-average velocity within each run. Averaging over the x position of the instantaneous depth-averaged velocity series, considering the inertial reference system above described, provides the spatially averaged time series of depth-averaged streamwise $\langle u_d \rangle$ and vertical $\langle w_d \rangle$ velocities shown in Figure 5.4.

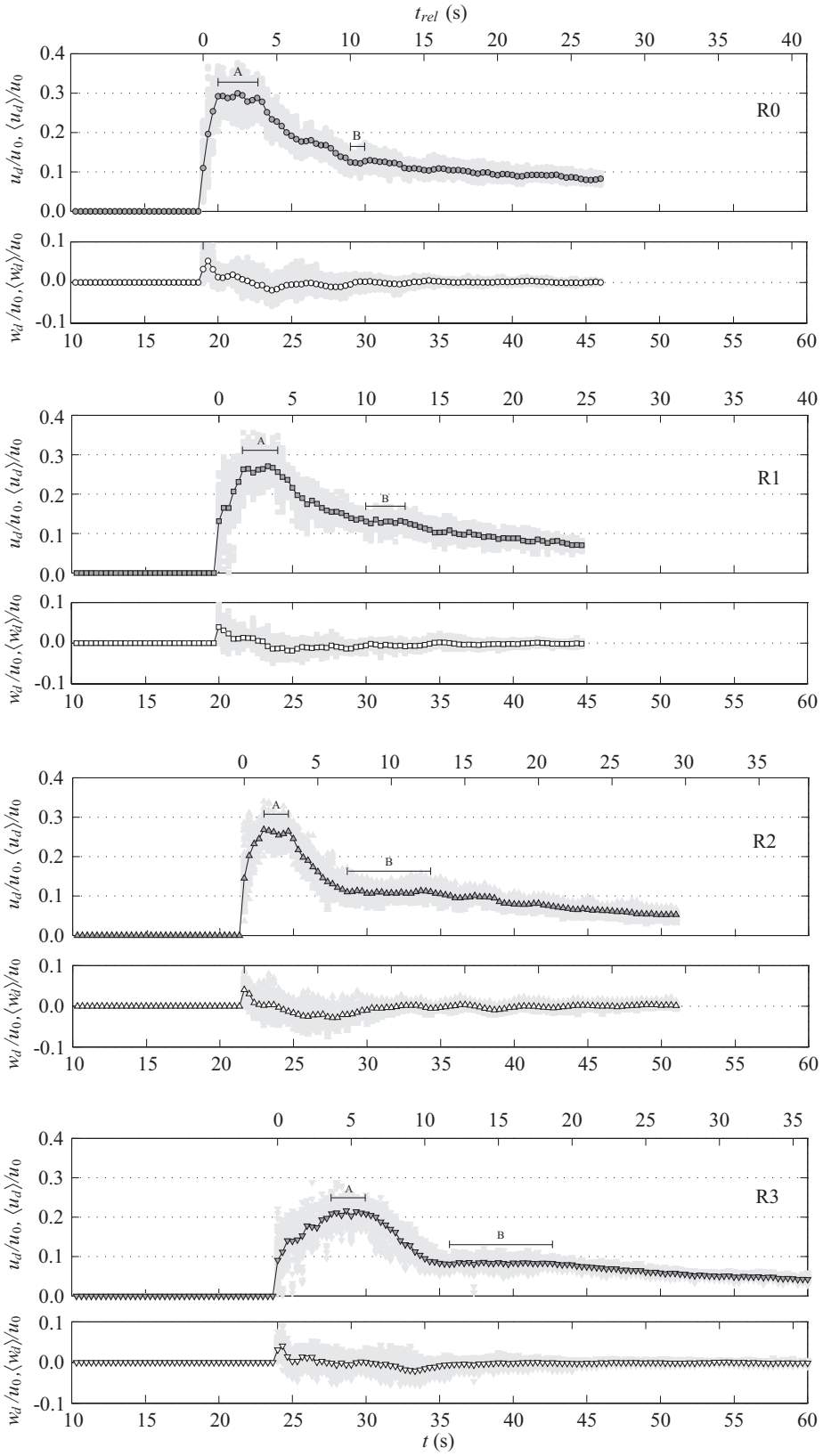

Figure 5.4: Normalized depth-averaged velocity components: time series for each individual streamwise location, $u_d(t)/u_0$ and $w_d(t)/u_0$ (shaded areas); spatially averaged time series $\langle u_d \rangle/u_0$ (filled symbols) and $\langle w_d \rangle/u_0$ (open symbols), for all runs performed (symbols explained in Table 2.3).

Figure 5.4 shows a period of *quasi*-steady streamwise flow corresponding to the current head for all runs; it is seen to occur in R0 from t_{rel} =1 to 4 s, in R1 from t_{rel} = 1.7 to 4 s, R2 from t_{rel} = 1.3 to 3 s and R3 from t_{rel} = 3.7 to 5.7 s. Kneller *et al.* (1999) had already observed similar behavior in the temporal series of the instantaneous streamwise velocity in a selected location within the current. This period, or region, is identified henceforth as 'A', for both temporal and spatial identification. The transition from the head to the remaining body of the current is characterized by a decrease in the streamwise component. This transition is more abrupt, i.e, with shorter duration, as the bed roughness increases. An outstanding consistent plateau in $\langle u_d \rangle$ that succeeds the transition phase is detected in all runs, with duration also influenced by the effect of roughness, increasing with this: for R0 a short stage is detected from t_{rel} = 10 to 11 s ($\approx$ 1 s), R1 from t_{rel} = 10 to 12.7 s ($\approx$ 3 s), R2 from t_{rel} = 7 to 13 s ($\approx$ 6 s) and R3 from t_{rel} = 11.7 to 18.7 s ($\approx$ 7 s). This *quasi*-steady region is then followed by a continuously decreasing asymptotic trend towards zero, compatible with the unsteady nature of the flow. The plateau in the body of the current is identified hereafter as region 'B'. The consistency of the steady behavior of the depth-averaged streamwise velocity in both regions A and B was confirmed by analyzing the cumulative sum of $\langle u_d \rangle$: the accumulated data follows a linear trend during the *quasi*-steady regions A and B, whereas the transition phase and the phase following region B are clearly non-linear (see Appendix B for more details).

5.4.2 Anatomy of the current

To have a global picture of the current profile, given the size-limited window of visualization, a compound profile of the current, $\langle h \rangle$, was obtained for each run from its instantaneous current profile $h(x,t)$. For each instant ($t = cte$), the series of the current height $h(x, t = cte)$ were shifted in space to align by the position of the current front, $x_f(t)$, all the profiles starting at the same streamwise reference point, by analogy with what was done in the previous section for the depth-averaged velocity. In this procedure it was necessary to estimate the current front position when it leaves the visualization window, which was done through Eq. (3.1) with the coefficients presented in section 5.2. A time-averaged profile is then computed for each run, resulting in the profiles of $\langle h \rangle$ presented in Figure 5.5, normalized by the initial water depth h_0. In Figure 5.5 the grey-shaded regions surrounding the mean profiles represent the standard deviation of the current height, σ_h. The x-axis represents the relative distance to the current front, normalized by the lock-length x_0. In Figure 5.5 the average delimitation of the regions A and B is also presented.

The compound profiles show that there is similarity between the current height among runs R0,

R1 and R2. Run R3 shows a profile with different shape, specially in the frontal part of the current. In general, the height starts to increase from the nose to the head of the current, until reaching a maximum in $\langle h \rangle / h_0 \approx 0.4$, which is then followed by a decrease trend until the end of region B, more or less pronounced depending on the run. The continuous decrease of the streamwise velocity that follows region B (cf. Figure 5.4) has a raising effect in the vertical location of $u = 0$, which leads to the increase of the current height since it is here defined as the location of zero streamwise velocity (cf. section 5.3). Using a kinematic variable to define the boundary of the current originates current profiles considerably different from the ones obtained through density assessment (cf. Hacker *et al.* 1996, Marino *et al.* 2005, and results in Chapter 3). The density of the gravity current decreases in time as a result of mixing with ambient fluid, leading to the decrease of the current height, an opposite behavior of what is observed here.

Run R2 shows a region of high deviation from the mean profile starting from x/x_0 =6.0 towards the end. This is a signature of a large-scale vortex, observed in the instantaneous vorticity maps (not shown here), that induces strong oscillations in the boundary of the current.

Regarding the average delimitation of the *quasi*-steady flow regions, the length of A is kept fairly constant among runs, nevertheless with varying position. The bed roughness is seen to influence the length of the transition from A to B and the length of the latter confirming the discussion in section 5.4.1: as roughness increases, transition length is shorter and the length of the steady region in the body tends to increase, also with a non-fixed location among runs.

5.4.3 Velocity and vorticity profiles

Based on the above given definitions of the *quasi*-steady flow regions within the current head (A) and body (B), mean velocity and vorticity profiles, presented in Figure 5.6, were obtained by spatial-averaging the compound (or time-averaged) profiles at each streamwise position within both regions. In Figure 5.6 the grey-shaded regions correspond to the standard deviation of each variable presented.

The mean streamwise velocity profiles, $\langle \bar{u} \rangle$, show for region A the countercurrent occupying a layer from the water surface until $z \approx 9$ cm, below which the streamwise velocity starts to increase until reaching a maximum around $z = 3$ cm. Velocity values then decrease towards zero at the flow bed. The height where maximum velocity occurs is conditioned by both drag forces at the upper shear layer and lower bottom layer (Middleton 1993, Kneller *et al.* 1997) and it was here observed to occur in the range $0.39 < z/h < 0.50$ in region A. These values are higher than the ones observed

in the literature for currents developing over smooth beds, with negligible countercurrent velocity ($0.20 < z/h < 0.30$). This shows the effect of the extra drag induced by the bed roughness and of the strong countercurrent flow, which raised the position where velocity maximum occurs, as already predicted by Kneller and Buckee (2000) and Gerber *et al.* (2011).

In region A, differences in both shape and magnitude in the profiles of $\langle \bar{u} \rangle$ between runs are notorious; run R0 (smooth bed) has the maximum velocity gradient detected, the transition between extreme velocity values being fairly linear. As roughness increases, maximum velocity gradients decrease and the transition between extreme values occurs nonlinearly, which is particularly well evidenced by the round-shaped profile in run R3. This smoother shape of the velocity profile with

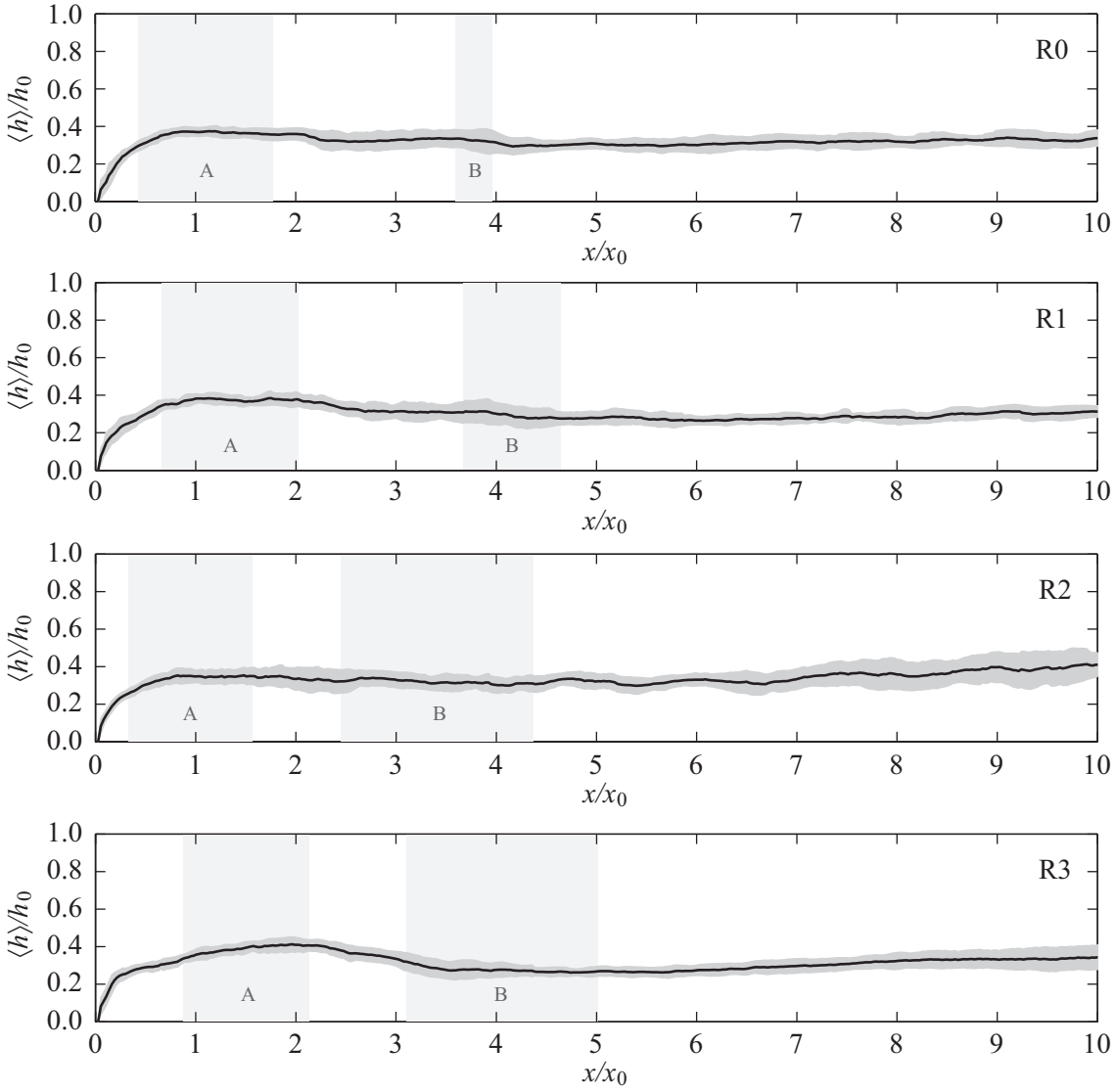

Figure 5.5: Compound profiles of the current $\langle h \rangle$, normalized by the water depth h_0, obtained by time-averaging the instantaneous profiles $h(x,t)$, shifted in space to align by the position of the current front $x_f(t)$ among instants. Shaded areas surrounding the mean profile correspond to the standard deviation. Shaded rectangle areas delimit the averaged location of regions A and B.

the increase of roughness seems to be related with the homogenization verified in the distribution of turbulence through the water depth for higher bed roughness, which was verified in the analysis of instantaneous velocity maps shown in Nogueira *et al.* (2012a). In run R3, an evident inflection of the velocity profile near the flow bed is observed due to extra bed drag induced by the roughness elements; this effect is also noted in run R2, with less expression, being apparently absent in run R1.

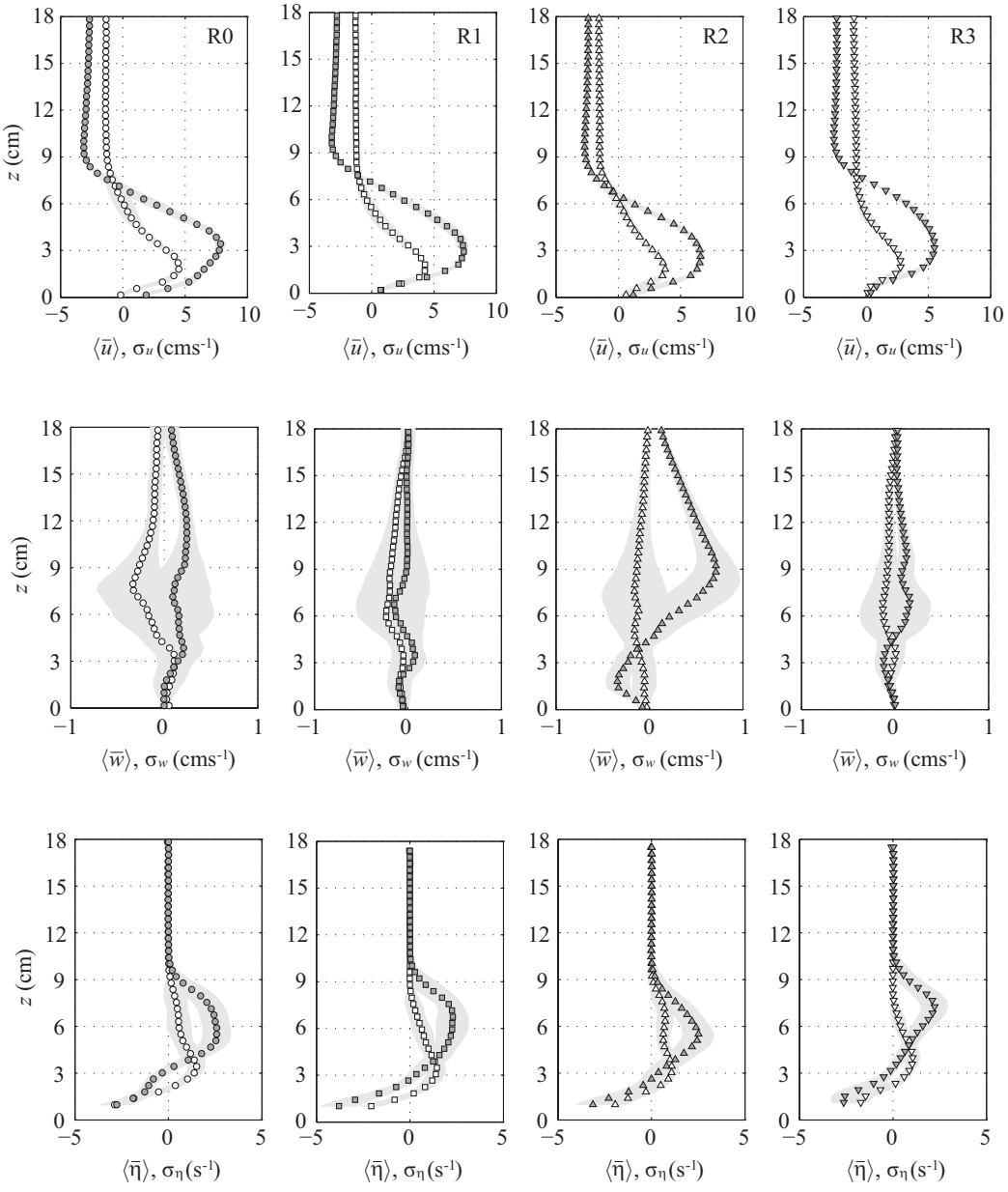

Figure 5.6: Averaged profiles of the streamwise $\langle\bar{u}\rangle$ and vertical $\langle\bar{w}\rangle$ velocity components, and vorticity $\langle\bar{\eta}\rangle$, for regions A (filled symbols) and B (open symbols), within the current, for all runs performed (symbols explained in Table 2.3). Shaded areas correspond to the standard deviation, σ, of each variable under analysis.

Regarding the profiles in the body of the current (region B), velocity gradients are lower than in the head region and the maximum velocity gradient is also seen to decrease as roughness increases. The maximum of $\langle\bar{u}\rangle$ is located at lower vertical positions, nearer the flow bed, $0.24 < z/h < 0.33$. These values are closer to the observations in the literature (Kneller *et al.* 1999, Kneller and Buckee 2000). Regarding the shape of the profiles, run R3 stands out from the remaining, exhibiting the typical round-shape profile already observed in region A. In the remaining runs, the linear phase observed in the profiles in region A, between velocity maximum and minimum, give place to a non-linear evolution of the streamwise velocity within the current.

The vertical component of velocity (Figure 5.6) shows that this is negligible in the flow bed and in the water surface. Within region A, positive values of the vertical velocity highlight the flow displaced upwards above the head and in the interfacial layer. This is observed in all runs with higher relevance in run R2 and less expression in R1. In region B, the vertical flow is negligible throughout the water depth, with exception in run R0 where downward flow is observed in the interfacial layer.

The averaged vorticity profiles for region A show that this is negligible within the countercurrent flow, starting to increase roughly near $z = 10$ cm, when the interfacial shear layer begins. The position of the maximum vorticity is seen to vary between runs, located, in general, at a higher height as roughness increases. Vorticity then decreases, crossing zero where the averaged streamwise velocity reached its maximum value, near $z = 3$ cm, undergoing to negative values in the bottom layer. Although the thickness of the layer of positive vorticity is fairly constant among runs, $\langle\bar{\delta}\rangle_\eta^+ \approx 8$ cm, (cf. Table. 5.1), its shape is clearly affected by the bed roughness: the region of maximum positive vorticity concentrates in a narrow region as roughness increases. While the vorticity magnitude is of the same order in both interfacial and bottom layers, the region of negative vorticity spreads over a thinner layer, with thickness of less then half the positive vorticity layer: $0.32 < \langle\bar{\delta}\rangle_\eta^-/\langle\bar{\delta}\rangle_\eta^+ < 0.38$, for region A and $0.19 < \langle\bar{\delta}\rangle_\eta^-/\langle\bar{\delta}\rangle_\eta^+ < 0.26$, for region B. There is a clear reduction in the rate of vorticity generation in region B when compared with the region within the head; vorticity generated near the flow bed is seen to dominate the interfacial vorticity after the head has passed, due to the reduction of the streamwise velocity and, consequently, the shear between currents.

Non-dimensional profiles of streamwise velocity and vorticity are presented in Figure 5.7 for both regions A and B. These were obtained by using their own outer flow scales: maximum velocity gradient, $\Delta\langle\bar{u}\rangle_{max}$, maximum vorticity, $\langle\bar{\eta}\rangle_{max}$, and length scale, $z_{0.5}$ (Table 5.1), defined

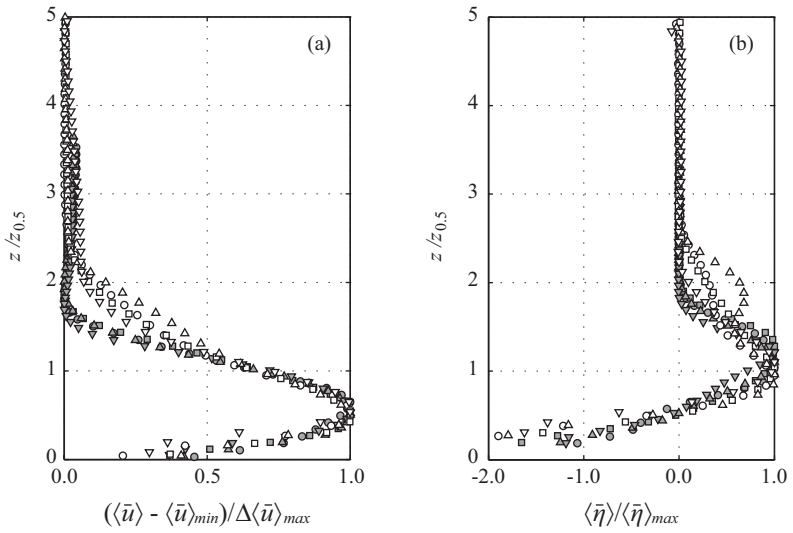

Figure 5.7: Normalized profiles of the averaged streamwise velocity (a) and vorticity (b) for regions A (filled symbols) and B (open symbols), for all runs performed (symbols explained in Table 2.3).

as the height of half the maximum averaged velocity (following Launder and Rodi 1983, Kneller and Buckee 2000, Gerber *et al.* 2011). There is a good data collapse of the velocity profiles in the head region (A). Maximum normalized streamwise velocities occur at $0.50 < z/z_{0.5} < 0.65$, higher than the values obtained when the countercurrent flow is negligible (Kneller and Buckee 2000, Gerber *et al.* 2011). The region within the body (B) has also a good data collapse for $z/z_{0.5} < 1$, exhibiting a significant scatter in the region above. Regarding the normalized vorticity profiles, below $z/z_{0.5} = 1$ data collapses well with the chosen scales. However, above that limit run R2 clearly deviates from the remaining (also visible in Figure 5.6). This is due to a large scale vortex that has temporal persistence in the body of the current, already detected in the profile of the current (Figure 5.5), and observed in the sequence of the instantaneous vorticity maps.

Table 5.1 summarizes the averaged variables evaluated in the regions A and B: current height, $\langle\bar{h}\rangle$, height of half the maximum velocity, $z_{0.5}$, maximum velocity, $\langle\bar{u}\rangle_{max}$, mean velocity $\langle\bar{u}\rangle_{mean}$, maximum velocity gradient, $\Delta\langle\bar{u}\rangle_{max}$, maximum vorticity, $\langle\bar{\eta}\rangle_{max}$, thickness of the upper and bottom shear layers normalized by the water depth, $\langle\bar{\delta}_{\eta}^{+}\rangle/h_0$ and $\langle\bar{\delta}_{\eta}^{-}\rangle/h_0$, respectively, Froude number, $Fr_{mean} = \langle\bar{u}\rangle_{mean}/\sqrt{g_0'\langle\bar{h}\rangle}$, and Reynolds number $Re_{mean} = \langle\bar{u}\rangle_{mean}\langle\bar{h}\rangle/\nu_a$, being ν_a the kinematic viscosity of water, here taken as $10^{-6}\mathrm{m}^2\cdot\mathrm{s}^{-1}$. Local Froude number shows that the flow in region B is less inertial than in the head, as expected given the velocity reduction observed between these regions. The flow within region A is still of turbulent nature, as shown by Reynolds numbers, while in the body the effect of viscosity becomes evident. Run R3 shows the lowest turbulent and inertial levels of all runs.

5.4.4 Reynolds stresses

Figures 5.8 and 5.9 present the profiles of the normal and shear Reynolds stresses evaluated in the *quasi*-steady regions within the gravity current head (A) and body (B), respectively. Reynolds stresses were evaluated in a similar fashion as time averaged velocity by averaging over space the time averaged profiles, $\overline{u_i' u_j'}(x,z)$, according to Eq. 1.13. The same kinematic outer scales used in Figure 5.7 are herein adopted for normalization.

Reynolds numbers in Table 5.1 indicate a strong decay of turbulence from the head region (A) to the region B of the current, which is followed by the turbulence levels observed in Figs. 5.8 and 5.9. In the body, the current tends to a viscosity phase which is more evident in run R3, as shown by the Reynolds number for this run (cf. Table 5.1). This result corroborate the findings on the kinematics of similar currents presented in Chapter 3, where the viscous phase seems to arrive earlier to the run with roughness R3, eventually due to deceleration induced by the extra bed resistance. The tendency to the homogenization of the velocity profiles above referred (cf. section 5.4.3) when roughness increase, seems thus to be an effect of viscosity which acts diffusing the current vertically, rather than an effect of turbulence transport. Although high values of $\langle\overline{u'u'}\rangle$ are observed in the bed region, maxima are generally located slightly above the position of maximum streamwise velocity, where the maximum gradient of this occur and within the interfacial shear layer, being thus this the main source of turbulence in the flow. This is observed for streamwise normal Reynolds stresses for both regions, A and B (Figures 5.8a and 5.9a, respectively). Local minima in streamwise normal stresses are seen roughly at the level corresponding to

Table 5.1: Variables characterizing the averaged flow in the regions of quasi-steady flow within the current head and body

Variable	R0		R1		R2		R3	
	A	B	A	B	A	B	A	B
$\langle\bar{h}\rangle$ (cm)	6.8	6.0	6.9	5.3	6.2	5.9	7.1	5.1
$z_{0.5}$ (cm)	5.3	3.6	5.3	3.4	5.0	3.6	6.0	3.6
$\langle\bar{u}\rangle_{max}$ (cm·s^{-1})	7.8	4.5	7.4	4.3	6.6	3.8	5.5	2.8
$\langle\bar{u}\rangle_{mean}$ (cm·s^{-1})	5.1	2.2	4.7	2.4	4.3	1.9	3.6	1.5
$\Delta\langle\bar{u}\rangle_{max}$ (cm·s^{-1})	11.0	5.9	10.6	5.6	9.3	5.3	8.1	3.8
$\langle\bar{\eta}\rangle_{max}$ (s^{-1})	2.7	1.5	2.3	1.7	2.8	1.2	2.3	1.1
$\langle\bar{\delta}_\eta^+\rangle/h_0$	0.40	0.43	0.41	0.37	0.38	0.48	0.42	0.37
$\langle\bar{\delta}_\eta^-\rangle/h_0$	0.15	0.10	0.13	0.08	0.13	0.09	0.16	0.10
Fr_{mean}	0.49	0.23	0.44	0.26	0.43	0.20	0.34	0.16
Re_{mean}	3472	1331	3204	1271	2715	1142	2543	738

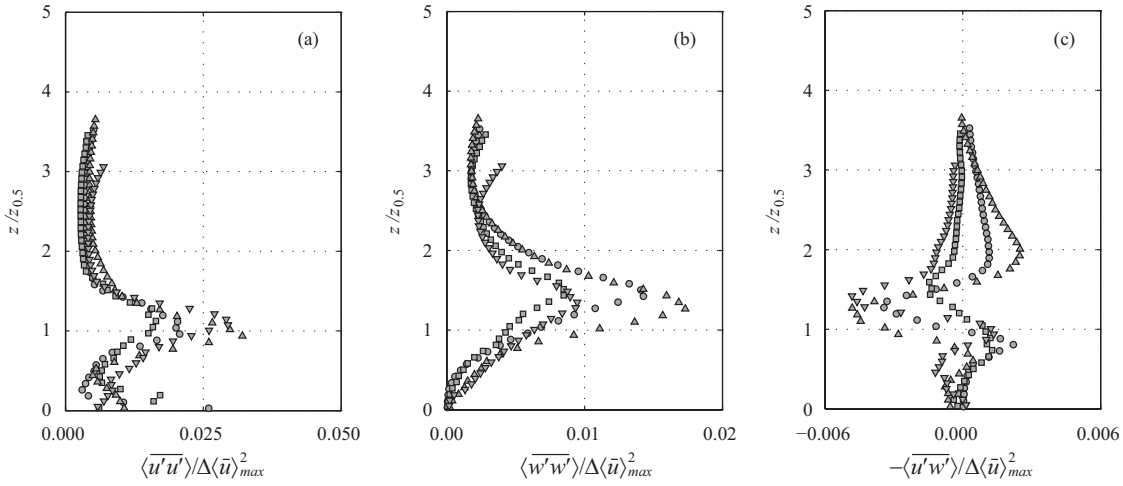

Figure 5.8: Normalized profiles of the averaged Reynolds stresses in the region A for all runs performed (symbols explained in Table 2.3).

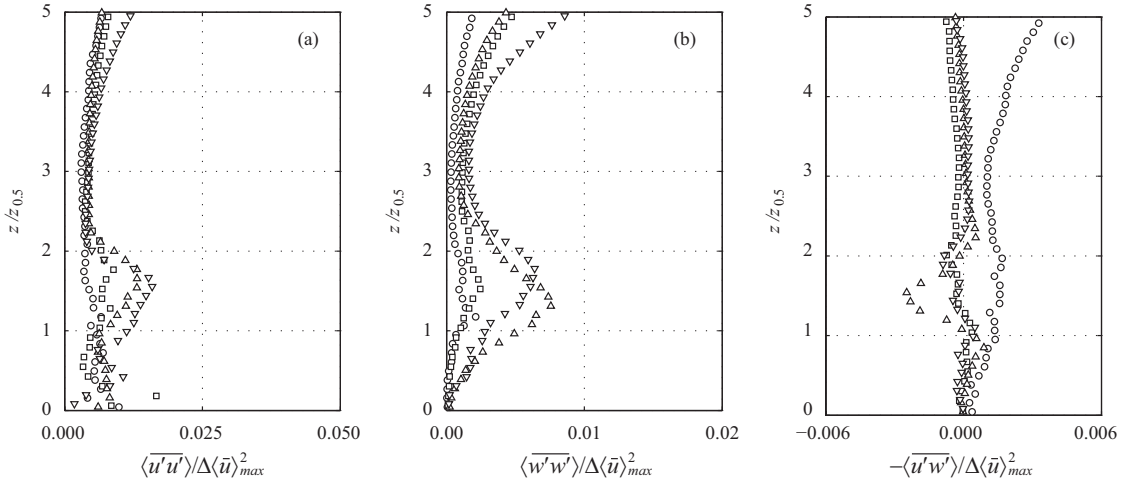

Figure 5.9: Normalized profiles of the averaged Reynolds stresses in the region B for all runs performed (symbols explained in Table 2.3).

maximum streamwise velocity for both regions of the current. For the vertical component $\langle\overline{w'w'}\rangle$ (Figures 5.8b and 5.9b), maximum occur also in the interfacial region, slightly above $\langle\overline{u'u'}\rangle$ maxima, whereas it tends to zero towards the lower layer of the flow, when fluctuation of the vertical component of the velocity are dumped by the tank bed.

From the present measurements, the effect of bed roughness in the turbulent characteristics of the flow is evidenced in the profiles taken in the body of the current: roughness is seen to enhance normal stresses as shown by Figures 5.9a) and b). In the head region, this trend is also observed in the profiles of $\langle\overline{u'u'}\rangle$ and $\langle\overline{u'w'}\rangle$. However, the effect of the bed roughness is not clear in the vertical component of the Reynolds stresses taken in region A.

Regarding the Reynolds shear stresses, in the head (region A, Figure 5.8c) and in the counter-

current region, these are are generally negligible. Towards the bed, when entering in the interfacial regions, one first positive peak is observed followed by a negative peak with lower amplitude located slightly above the position of maximum streamwise velocity. Below this position, shear stress tends to zero. In the region B (Figure 5.9c), significant values of shear stress are only observed in the interfacial region as well. Here, the smooth bed case presents only negative values with considerably higher amplitude than the remaining tests. These latter generally show the same trend as observed for the head, two adjacent positive and negative regions, although with less expression. Results in terms of shear stress confirm again the lower turbulence levels in region B. The effect of the extra drag induced by the bed roughness does not cause additional shear stresses but rather a decrease of turbulence due to the deceleration of the flow and the anticipation of the viscous phase.

Shear stresses near the bed are low, even for the rougher beds. The manifestation of the extra resistance induced by the rough bed must thus be given either by form-induced (or dispersive) stresses, due to the spatial and time intermittency of the turbulent field within the roughness layer, either by the pressure drag caused by the flow separation within this layer (Nikora *et al.* 2001).

5.5 Conclusions

Lock-exchange gravity currents were performed to visualize and to characterize the inner flow features and to investigate the influence of the bed roughness in the velocity, vorticity and turbulence fields, through Particle Image Velocimetry.

The arrival of the gravity current at each streamwise location is noticed throughout the water depth: in the frontal interface, ambient fluid is mainly displaced upwards, being incorporated by the strong countercurrent flowing in the upstream direction that develops above the denser current. This countercurrent flow is accelerated by the intense vortex generation in the interfacial shear layer which, by continuity, propagates this effect to the streamwise flow beneath it. Several rotating cells are generated in the interfacial shear layer. These are usually surrounded by strain-dominated flow, responsible for the exchange and mixture of both ambient and dense fluids, inducing current dilution.

Two regions of *quasi*-steady streamwise flow were observed within the current by analyzing the time series of instantaneous streamwise velocity, both local and depth-averaged values; the characterization of the flow within the head and body of the current was based on the averaged

quantities, in both time and space, assessed within each of these regions. In the head, the flow is characterized by higher streamwise velocity and higher vorticity production in both interfacial and bottom layers. After the current head has passed, vorticity generated in the interfacial shear layer vanishes, due to the reduction of the overall streamwise velocity within the water depth, and the vorticity generated at the bed level starts to dominate the flow.

Reynolds stresses are predominant in the head region, above the streamwise velocity maxima, in the interfacial shear layer. In the body, turbulence levels tend to vanish with exception of the normal streamwise stresses which become also important near the flow bed, in accordance with the observations above.

Bed roughness has the expected effect of velocity reduction: front velocity and inner streamwise velocity were reduced with the increase of the size of the bed material used. The shape of the vertical profiles of streamwise velocity and vorticity is also affected by the increase of the roughness elements: it was seen to homogenize the velocity distribution within the current, reducing the maximum velocity gradient, and to originate a round-shaped velocity profile, with inflection near the flow bed more evident with the increase of roughness, in both head and body regions. This effect in the velocity profiles is probably due to the reduction of the streamwise velocity, inducing diffusive-type effects within the current.

The results presented herein confirm that the size and porosity of the bed material play a role in the current kinematics, since differences in the velocity and vorticity fields are more relevant in the extreme runs performed, i.e., the smooth bed and the highest roughness bed case.

Chapter 6

Conclusions and future research

Contents

6.1 Conclusions

To meet the aims of the present research, two sets of lock-exchange experiments were performed to assess separately the density and the velocity fields of unsteady gravity currents. The first set of experiments allowed the temporal and spatial width-averaged characterization of the density field through an image analysis technique, from where the bulk and local characteristic variables of the gravity current could be estimated. These allowed the parameterization of the current front velocity and of the entrainment of ambient fluid into the current, clarifying the effect of the initial density gradient and of the bed roughness. The second set of experiments, using Particle Image Velocimetry, enabled the visualization and characterization of the instantaneous velocity field, from where the vorticity and the turbulence fields were obtained. Two regions of quasi-steady streamwise velocity were detected in both head and body of the current. These regions were characterized, being investigated the effect of the bed roughness.

Immediately after the release of the dense fluid inside the lock, a gravity current of heavy fluid forms near the bed and evolves towards downstream; simultaneously, a current formed by lighter fluid flows above the heavy current in the opposite direction, towards upstream. During its development, the denser current mixes with the surrounding ambient fluid and continuously entrains part of it. The interaction between fluids is more dynamic in the head region and a notorious pattern of head stretching and break was herein observed and characterized. As the head entrains ambient fluid, its dimensions and mass increase accordingly, until it becomes unstable and, consequently, breaks. After breaking, the head leaves behind quasi-steady large-scale billows that remain at the rear of the head, promoting strong mixing in that region, which eventually fade in time by diffusion-type processes.

The answers to the research questions initially raised are presented below.

- ◊ Q_1 - *How does the bed roughness and the initial density gradient affect the velocity of propagation and the density distribution of gravity currents?*

  The front velocity increases with the initial density gradient and decreases with the increase of the bed roughness. The kinematics of the front show two different phases: (i) a first phase where the front velocity is nearly constant; the analysis of the densimetric Froude number showed that front velocity is well parameterized by a characteristic velocity obtained with the initial quantities of each experiment, $u_0 = \sqrt{g'_0 h_0}$, where a consistent collapse around $Fr = 0.46$ was obtained; (ii) a second phase of continuously decreasing front veloc-

ity starts when the reflected bore, generated by the gate removal, overtakes the current front; during this phase the current front is seen to be in equilibrium with its buoyancy celerity, where densimetric Froude number defined purely with local variables assessed at the head, $Fr_{h,h_m} = u_f / \sqrt{g'_h h_m}$, collapses consistently around $Fr = 1$. The results obtained for the run with highest roughness elements deviate from the remaining runs: the transition between phases occur earlier and the decrease of the front velocity during the second phase is more pronounced than the remaining runs. The parameterization adopted for the front position and front velocity does not seem fully adequate for this run, indicating that an additional parameter taking into account the roughness of the lower boundary and/or the porosity of the rough bed is needed.

Regarding the density distribution within the current, the head is where higher density is observed. This observation was considered to establish the criterion used to isolate this region for further analysis. Significant dilution occurs since the early stages of the current development, and as the initial density gradient increases, stronger mixing with the surrounding fluid is observed, leading to faster density decay. The bed roughness effect is similar to the initial density gradient, except for the highest roughness tested, where no significant dilution is observed when compared with the smooth bed case.

◊ *Q_2 - In which stages of the gravity current development does entrainment occur? How is it affected by the bed roughness and density gradient? How does entrainment affect the head dynamics?*

The bulk entrainment parameter shows that entrainment occurs under subcritical conditions. Entrainment estimated at the gravity current head corroborates the previous affirmation and it was observed at all stages of the current development, including the early stages, where higher entrainment rates are observed. Gravity currents originated with higher density gradients are expected to have higher values of entrainment parameter, a trend also observed when using roughness elements in the tank bed. However, the highest roughness does not corroborate this trend, showing the lowest value of the entrainment parameter of all runs.

As the current evolves, ambient fluid is continuously entrained at the current head increasing its size and mass. As a consequence, the entrained ambient fluid reduces the driving force of the current, due to current dilution, leading to less fluid to be entrained afterwards. This is reflected in the temporal decreasing trend of the normalized mass growing rate at the

head. The similarity of this parameter between runs suggests that this is independent from the initial density gradient and the bed roughness. Both Froude and Reynolds numbers influence, naturally, the evolution of the mass growing rate. In particular, a linear increasing relation is observed for lower values of $Fr_h Re_h$, corresponding to later stages of the current development, when all the parameters in question decrease consistently. For high Reynolds numbers, entrainment increases significantly indicating a higher efficiency of turbulent-type processes in entraining ambient fluid when compared to viscous diffusion.

The gravity current head was seen to develop in successive cycles of stretching and consequent break, being herein identified and characterized. The evolution of the head aspect ratio during the stretching period shows a consistent limit, for all performed runs, of $h_m/L_h = 0.2$, corresponding to the breaking instants. In addition, during these instants the mass of the gravity current head is seen to be of the same order of the mass initially in the lock, especially during the first phase of the current development. Bed roughness is seen to play an important role in this process. As roughness increases, besides the expected current deceleration, the break events become less frequent. Similarity of the stretching events between runs is confirmed by the consistent collapse of the analyzed variables at the head, h_m/L_h, M_h/M_{c_0}, E_h/E_b and M_h^*, when performing a phase analysis over stretching cycles with normalized duration.

◊ *Q_3 - What are the effects of the bed roughness on the inner velocity, vorticity and turbulence fields?*

Two regions of quasi-steady streamwise flow were observed within the current by analyzing the time series of instantaneous streamwise velocity, both local and depth-averaged values. The increase of the bed roughness has the expected effect of streamwise velocity reduction. The shape of the vertical streamwise velocity profiles and vorticity is also affected by the increase of the lower boundary roughness: these were seen to homogenize the velocity distribution within the current, reducing the maximum velocity gradient, and to originate a round-shaped velocity profile, with inflection near the flow bed more evident with the increase of roughness, in both head and body regions. This effect in the velocity profiles is probably due to the reduction of the streamwise velocity, inducing diffusive-type effects within the current.

In the head, the flow is characterized by higher streamwise velocity and higher vorticity

production in both interfacial and bottom layers. After the current head has passed, vorticity generated in the interfacial shear layer vanishes, due to the reduction of the overall streamwise velocity within the water depth, and the vorticity generated at the bed level starts to dominate the flow.

Reynolds stresses are predominant in the head region, above the streamwise velocity maxima, in the interfacial shear layer. In the body, turbulence levels tend to vanish with exception of the normal streamwise stresses which become also important near the flow bed.

In the present research a new image analysis technique to measure the width-averaged density field of the current was developed. It is a simple way to assess the density distribution within the gravity current, allowing the investigation of the gravity current dynamics and mixing processes.

The results arising from the present research provide useful data for mixing and entrainment parameterization in unsteady gravity currents. It was shown that entrainment occurs at all stages of the gravity current development and for subcritical flow conditions, contributing to fill the gap in the entrainment estimation for such flows. The experimentally obtained rates of advance and dilution of unsteady gravity currents are nevertheless important data to calibrate numerical models used to predict their kinematics and dynamics in many practical applications in geosciences and environmental engineering.

6.2 Future research

The research presented in this thesis have raised some questions indicating several lines of research to be pursued.

The effect of the initial density gradient in the propagation of gravity currents is a rather well understood problem. It increases the buoyancy force of the current, which leads to the increase of the front velocity and, consequently, faster mixing with the ambient fluid occurs. This leads to higher values of the entrainment parameter, accordingly.

On the other hand, the effect of the bed roughness is not completely understood. Contradictory results were obtained and need further development. Previous works have found that higher roughness elements lead to higher entrainment and dilution. The results here presented could not corroborate such affirmation for all the roughness scales tested. The size and porosity of the bed material play a role in both current kinematics and dynamics, since differences in the front velocity, in the density field and in the inner velocity, vorticity and turbulence fields are more relevant

in the runs where highest roughness bed was used. In particular, a broader range of material sizes to reproduce bed roughness should be considered in further research works.

The effect of the bed roughness could be combined with the variation of other experimental variables, such as the slope of the tank/channel (upsloping, downsloping), the fractional depth, in the case of unsteady currents, or combined with continuously fed currents.

The simultaneous measurement of density and velocity fields would contribute to adequate closures for governing mass and momentum conservation equations, which are not available. More specifically, closures are still needed in what concerns the interaction between developing density currents and the lower fixed-bed and the upper permeable boundary, where spatial and temporal varying boundaries must be taken into account. It should also be explored the limits for which the two-dimensional flow assumption is adequate for such currents and where its three-dimensional behavior should be considered.

PIV experiments could be improved by using “Kosher” salt instead or regular kitchen salt. This type of salt has no additives, minimizing the blurriness of the PIV images. A wider range of densities could therefore be tested as well as flow analysis near the lock, where are observed the highest density gradients. To overcome the problem of different refractive indices between fluids, techniques of RIM (Refractive Index Matching) could also be explored and applied.

Bibliography

Adduce, C., Lombardi, V., Sciortino, G., La Rocca, M., Morganti, M. (2011). Analysis of lock release gravity currents by PIV. In *Proc. 7th Int. Symp. on Stratified Flows*, Rome, Italy, 1097.

Adduce, C., Lombardi, V., Sciortino, G., Morganti, M. (2009). Roughness effects on gravity currents dynamics. In *Proc. 33rd IAHR Congress*, Vancouver, Canada.

Adduce, C., Sciortino, G., Proietti, S. (2012). Gravity currents produced by lock-exchanges: experiments and simulations with a two layer shallow-water model with entrainment. *J. Hydr. Eng.* 138(2), 111 – 121.

Alahyari, A., Longmire, E.K. (1996). Development and structure of a gravity current head. *Exp. Fluids* 20, 410 – 416.

Alavian, V. (1986). Behaviour of density currents on an incline. *J. Hydr. Eng.* 112(1), 27 – 42.

Aleixo, R. (2012). Experimental study of the early stages of a dam-break flow over fixed and mobile beds. *PhD thesis*, Université catholique de Louvain, Louvain-la-Neuve, Belgium.

Allen, J.R.L. (1971). Mixing at turbidity currents heads, and its geological implications. *Sedimentary Petrology* 41(1), 97 – 113.

Althaus, J.M.I.J., De Cesare, G., Schleiss, A.J. (2011). Fine sediment release from a reservoir by controlled hydrodynamic mixing. In *Proc. 34th IAHR World Congress*, Brisbane, Australia, 662 – 669.

Altinakar, M.S. (1993). Weakly depositing turbidity currents on small slopes. *PhD thesis*, École Polytechnique Fédérale de Lausanne, Lausanne, Switzerland.

Alves, E. (2008). Sedimentação em albufeiras por correntes de turbidez. *PhD thesis*, Universidade Técnica de Lisboa, Lisbon, Portugal.

Alves, E., González, J., Freire, P., Cardoso, H. (2008). Experimental study of plunging turbidity currents in reservoirs. In *Proc. River Flow 2008*, Çeşme-Izmir, Turkey, 1157 – 1164.

Arneborg, L., Fiekas, V., Umlauf, L., Burchard, H. (2007). Gravity current dynamics and entrainment - a process study based on observations in the Arkona Basin. *J. Physical Oceanogr.* 37, 2094 – 2113.

Baines, P.G. (2001). Mixing in flows down gentle slopes into stratified environments. *J. Fluid Mech.* 443, 237 – 270.

Ball, F.K. (1956). The theory of strong katabatic winds. *Aust. J. Phys.* 9, 373 – 386.

Baringer, M.O., Price, J.F. (1997). Mixing and spreading of the Mediterranean outflow. *J. Phys. Oceanogr.* 27, 1654 – 1677.

Benjamin, T.B. (1968). Gravity currents and related phenomena. *J. Fluid Mech.* 31, 209 – 248.

Bombardelli, F.A., Cantero, M.I., García, M.H., Buscaglia, G.C. (2009). Numerical aspects of the simulation of descontinuous saline underflows: the lock-exchange problem. *J. Hydr. Res.* 47(6), 777 – 789.

Britter, R.E., Linden, P.F. (1980). The motion of the front of a gravity current travelling down an incline. *J. Fluid Mech.* 99(3), 531 – 543.

Britter, R.E., Simpson, J. (1978). Experiments on the dynamics of a gravity current head. *J. Fluid Mech.* 88(2), 223 – 240.

Brocchini, M., Peregrine, D.H. (2001). The dynamics of strong turbulence at free surfaces. part 2. free-surface boundary conditions. *J. Fluid Mech.* 449, 255 – 290.

Cantero, M.I., Balachandar, S., García, M.H., Bock, D. (2008). Turbulent structures in planar gravity currents and their influence on the flow dynamics. *J. Geophys. Res.* 113(C08018).

Cantero, M.I., Lee, J.R., Balachandar, S., García, M.H. (2007). On the front velocity of gravity currents. *J. Fluid Mech.* 586, 1 – 39.

Cenedese, C., Adduce, C. (2008). Mixing in a density driven current flowing down a slope in a rotating fluid. *J. Fluid Mech.* 604, 369 – 388.

Cenedese, C., Adduce, C. (2010). A new entrainment parametrization for mixing in overflows. *J. Physical Oceanogr.* 40(8), 1835 – 1850.

Cenedese, C., Whitehead, J.A., Ascarelli, T.A., Ohiwa, M. (2004). A dense current flowing down a sloping bottom in a rotating fluid. *J. Physical Oceanogr.* 34, 188 – 203.

Chassignet, E., Cenedese, C., Verron, J. (Eds.) (2012). *Buoyancy-Driven Flows*. Cambridge University Press.

Dallimore, C.J., Imberger, J., Ishikawa, T. (2001). Entrainment and turbulence in saline underflow in Lake Ogawara. *J. Hydr. Eng.* 127(11), 937 – 948.

Ding, A., Wang, T., Zhao, M., Wang, T., Li, Z. (2004). Simulation of sea-land breezes and a discussion of their implications on the transport of air pollution during a multi-day ozone episode in the Pearl River Delta of China. *Atmos. Environ.* 38(39), 6737 – 6750.

Elder, R.A., Wunderlich, W.O. (1972). Inflow density currents in TVA reservoirs. In *Proc. of Int. Symp. on Stratified Flows*, Novosibirsk.

Ellison, T.H., Turner, J.S. (1959). Turbulent entrainment in stratified flows. *J. Fluid. Mech.* 6, 423 – 448.

Fan, J., Morris, G.L. (1992). Reservoir sedimentation I: delta and density current deposits. *J. Hydr. Eng.* 118(3), 354 – 369.

Fernandez, R.L., Imberger, J. (2006). Bed roughness induced entrainment in a high Richardson number underflow. *J. Hydr. Res.* 44(6), 725 – 738.

Fine, I.V., Rabinovich, A.B., Bornhold, B.D., Thomson, R.E., Kulikov, E.A. (2005). The Grand Banks landslide-generated tsunami of November 18, 1929: preliminary analysis and numerical modeling. *Marine Geology* 215, 45 – 57.

García, C.M., Oberg, K., García, M.H. (2007). ADCP measurements of gravity currents in the

Chicago river, Illinois. *J. Hydr. Eng.* 133(12), 1356 – 1366.

García, M.H., Parsons, J.D. (1996). Mixing at the front of gravity currents. *Dynamics of Atmospheres and Oceans* 24, 197 – 205.

Gerber, G., Diedericks, G., Basson, G.R. (2011). Particle image velocimetry measurements and numerical modeling of a saline density current. *J. Hydr. Eng.* 137(3), 333 – 342.

Girton, J.B., Sanford, T.B. (2003). Descent and modification of the overflow plume in Denmark Strait. *J. Phys. Oceanogr.* 33, 1351 – 1364.

Graf, W.H., Altinakar, M.S. (1998). *Fluvial Hydraulics. Flow and transport processes in channels of simple geometry*. John Wiley and Sons, England.

Hacker, J., Linden, P.F., Dalziel, S.B. (1996). Mixing in lock-release gravity currents. *Dynamics of Atmospheres and Oceans* 24, 183 – 195.

Hallworth, M.A., Huppert, H.E., Phillips, J.C., Sparks, R.S.J. (1996). Entrainment into two-dimensional and axisymmetric turbulent gravity currents. *J. Fluid Mech.* 308, 289 – 311.

Härtel, C., Meiburg, E., Necker, F. (2000). Analysis and direct numerical simulation of the flow at a gravity-current head. part 1. flow topology and front speed for slip and no-slip boundaries. *J. Fluid Mech.* 418, 189 – 212.

Hebbert, B., Imberger, J., Loh, I., Patterson, J. (1979). Collie River underflow into the Wellington reservoir. *J. Hydr. Div. ASCE* 105(5), 533 – 545.

Huppert, H.E. (1982). The propagation of two-dimensional and axisymmetric viscous gravity current over a rigid horizontal surface. *J. Fluid Mech.* 121, 43 – 58.

Huppert, H.E. (2006). Gravity currents: a personal perspective. *J. Fluid Mech.* 554, 299 – 322.

Huppert, H.E., Simpson, J.E. (1980). The slumping of gravity currents. *J. Fluid Mech.* 99(4), 785 – 799.

Isern-Fontanet, J., Font, J., García-Ladona, E., Emelianov, M., Millot, C., Taupier-Letage, I. (2004). Spatial structure of anticyclonic eddies in the Algerian basin (Mediterranean Sea) analyzed using the Okubo-Weiss parameter. *Deep-Sea Res. II* 51, 3009–3028.

Kantoush, S.A., Sumi, T., Murasaki, M. (2010). Evaluation of sediment bypass efficiency by flow field and sediment concentration monitoring techniques. *J. Hydr. Eng.* 55.

Kestin, J., Khalifa, H.E., Correia, R.J. (1981). Tables of the dynamic and kinematic viscosity of aqueous NaCl solutions in the temperature range 20-150°C and the pressure range 0.1-35MPa. *Physical and Chemical Reference Data* 10(1), 71 – 87.

Keulegan, G.H. (1949). Interfacial instability and mixing in stratified flows. *J. Res. US Bur. Stand.* 43(487).

Khavasi, E., Afshin, H., Firoozabadi, B. (2012). Effect of selected parameters on the depositional behaviour of turbidity currents. *J. Hydr. Res.* 50(1), 60 – 69.

King, D., Galvin, C.J. (2002). Coastal Sediment Properties. *Costal Engineering Manual, Part III, Engineering manual 1110-2-1100*, ed. D. King. US Army Corps of Engineers, Washington D.C.

Klein, T., Heinemann, G., Bromwich, D.H., Cassano, J.J., Hines, K.M. (2001). Mesoscale model-

ing of katabatic winds over Greenland and comparisons with AWS and aircraft data. *Meteorol. Atmos. Phys.* 78, 115 – 132.

Kneller, B.C., Bennett, S.J., McCaffrey, W.D. (1997). Velocity and turbulence structure of density currents and internal solitary waves: potential sediment transport and the formation of wave ripples in deep water. *Sediment. Geol.* 112, 235 – 250.

Kneller, B.C., Bennett, S.J., McCaffrey, W.D. (1999). Velocity structure, turbulence and fluid stresses in experimental gravity currents. *J. Geophys. Res.* 104(C3), 5381 – 5391.

Kneller, B.C., Buckee, C. (2000). The structure and fluid mechanics of turbidity currents: a review of some recent studies and their geological implications. *Sedimentology* 47(1), 62 – 94.

Kostic, S., Parker, G. (2003). Progradational sand-mud deltas in lakes and reservoirs. part 1. theory and numerical modeling. *J. Hydr. Res.* 41(2), 127 – 140.

La Rocca, M., Adduce, C., Lombardi, V., Sciortino, G., Hinkelmann, R. (2012b). Development of a lattice Boltzmann method for two-layered shallow-water flow. *Int. J. Numer. Meth. Fluids* 70(8).

La Rocca, M., Adduce, C., Sciortino, G., Pinzon, A.B. (2008). Experimental and numerical simulation of three-dimensional gravity currents on smooth and rough bottom. *Phys. Fluids* 20, 106603.

La Rocca, M., Adduce, C., Sciortino, G., Pinzon, A.B., Boniforti, M.A. (2012a). A two-layer, shalow water model for 3D gravity currents. *J. Hydr. Res.* 50(2), 208 – 217.

Lalas, D.P., Asimakopoulos, D.N., Deligiorgi, D.G. (1983). Sea-breeze circulation and photochemical pollution in Athens, Greece. *Atmos. Environ.* 17(9), 1621 – 1632.

Launder, B.E., Rodi, W. (1983). The turbulent wall jet - measurements and modeling. *Ann. Rev. Fluid Mech.* 15, 429–459.

Legg, S. (2012). Overflows and convectively driven flows. *Buoyancy-Driven Flows*, eds. E. Chassignet, C. Cenedese, and J. Verron. Cambridge University Press.

Lombardi, V. (2012). Gravity currents: laboratory experiments and numerical simulations. *PhD thesis*, Università degli studi Roma Tre, Rome, Italy.

Lopes, A.F., Nogueira, H.I.S., Ferreira, R.M.L., Franca, M.J. (2013). Laboratorial study of continuously fed low-submergence gravity currents over smooth and rough beds. *Geophys. Res. Abstracts*, Vienna, Austria, 15(8847).

Marino, B.M., Thomas, L.P., Linden, P.F. (2005). The front condition for gravity currents. *J. Fluid Mech.* 536, 49 – 78.

Martin, J.E., García, M.H. (2009). Combined PIV/PLIF measurements of a steady density current front. *Exp. Fluids* 46, 265 – 276.

Martin, J.E., Sun, T., García, M.H. (2012). Optical methods in the laboratory: an application to density currents over bedforms. *Environmental Fluid Mechanics: Memorial Volume in Honour of Prof. Gerhard H. Jirka - IAHR Monograph*, eds. W. Rodi and M. Uhlman. CRC Press - Taylor & Francis Group.

Mauritzen, C., Price, J., Sanford, T., Torres, D. (2005). Circulation and mixing in the Faroese

Channels. *Deep-Sea Res I* 52, 883 – 913.

Middleton, G.V. (1993). Sediment deposition from turbidity currents. *Ann. Rev. Earth Planet. Sci.* 21, 89 – 114.

Neufeld, J. (2002). Lobe-cleft patterns in the leading edge of a gravity current. *PhD thesis*, University of Toronto, Toronto, Canada.

Nikora, V., Goring, D., McEwan, I., Griffiths, G. (2001). Spatially averaged open-channel flow over rough bed. *J. Hydr. Eng.* 127(2), 123 – 133.

Nogueira, H.I.S. (2011). Time and space analysis of entrainment on density currents. In *Proc. 34th IAHR World Congress*, Brisbane, Australia, 3667 – 3674.

Nogueira, H.I.S., Adduce, C., Alves, E., Franca, M.J. (2010). Evaluation of time-space varying density distribution on gravity currents by image analysis technique. In *Proc. XVIII A.I.VE.LA. Meeting & Exhibition*, Rome, Italy.

Nogueira, H.I.S., Adduce, C., Alves, E., Franca, M.J. (2011a). Analysis of the entrainment on lock-exchange density currents. *Geophys. Res. Abstracts*, Vienna, Austria, 13(7011).

Nogueira, H.I.S., Adduce, C., Alves, E., Franca, M.J. (2011b). Phase analysis of lock-exchange gravity currents. In *Proc. 7th Int. Symp. on Strat. Flows*, Rome, Italy.

Nogueira, H.I.S., Adduce, C., Alves, E., Franca, M.J. (2012a). Dynamics of the head of gravity currents. In *Proc. 4th IAHR Int. Symp. Hydr. Struct.*, Porto, Portugal, 9-11 February.

Nogueira, H.I.S., Adduce, C., Alves, E., Franca, M.J. (2012b). The influence of bed roughness on the dynamics of gravity currents. In *Proc. River Flow 2012*, San José, Costa Rica, 5-7 September, 357–362.

Nogueira, H.I.S., Adduce, C., Alves, E., Franca, M.J. (2012c). Periodic cycle of stretching and breaking of the head of gravity currents. *Geophys. Res. Abstracts*, Vienna, Austria, 14(3486).

Nogueira, H.I.S., Adduce, C., Alves, E., Franca, M.J. (2012d). Visualization and characterization of gravity currents over rough beds by means of PIV measurements. In *Proc. 2nd IAHR Europe Congress*, Munich, Germany, 27-29 June.

Nogueira, H.I.S., Adduce, C., Alves, E., Franca, M.J. (2013a). Analysis of lock-exchange gravity currents over smooth and rough beds. *J. Hydr. Res.* 51(4), 417 – 431.

Nogueira, H.I.S., Adduce, C., Alves, E., Franca, M.J. (2013b). Dynamics of the head of gravity currents. *Env. Fluid Mech.*. Advance online publication. doi:10.1007/s10652-013-9315-2.

Nogueira, H.I.S., Adduce, C., Alves, E., Franca, M.J. (2013c). Image analysis technique applied to lock-exchange gravity currents. *Meas. Sci. Technol* 24(047001), 4pp.

Nogueira, H.I.S., Adduce, C., Alves, E., Franca, M.J. (2013d). Kinematic characterization of unsteady gravity currents developing over smooth and rough beds. *Manuscript submitted for publication*.

Nogueira, H.I.S., Adduce, C., Alves, E., Franca, M.J. (2013e). Phase analysis of the stretching cycles of the head of unsteady gravity currents developing over smooth and rough beds. In *Proc. 35th IAHR World Congress*, Chengdu, China, 8-13 September.

Oehy, C., Schleiss, A.J. (2007). Control of turbidity currents in reservoirs by solid and permeable

obstacles. *J. Hydr. Eng.* 133(6), 637 – 648.

Okubo, A. (1970). Horizontal dispersion of floatable particles in the vicinity of velocity singularities such as convergences. *Deep Sea Res.* 17(3), 445 – 454.

Ooi, S.K., Constantinescu, G., Weber, L.J. (2007). 2D Large-eddy simulation of lock exchange gravity current flows at high Grashof numbers. *J. Hydr. Eng.* 133(9), 1037 – 1047.

Özgökmen, T.M., Fischer, P.F. (2008). On the role of bottom roughness in overflows. *Ocean Modelling* 20(9), 336 – 361.

Özgökmen, T.M., Fischer, P.F., Duan, J., Iliescu, T. (2004). Three-dimensional turbulent bottom density currents from a high-order nonhydrostatic spectral element model. *J. Physical Oceanogr.* 34, 2006 – 2026.

Özgökmen, T.M., Iliescu, T., Fischer, P.F. (2009). Large eddy simulation of stratified mixing in a three-dimensional lock-exchange system. *Ocean Modelling* 26, 134 – 155.

Paik, J., Eghbalzadeh, A., Sotiropoulos, F. (2009). Tree-dimensional unsteady RANS modelling of discontinuous gravity currents in rectangular domains. *J. Hydr. Eng.* 135(6), 505 – 521.

Parish, T.R., Bromwich, D.H. (1991). Continental-scale simulation of the Antarctic katabatic wind regime. *J. Climate* 4, 135 – 146.

Parker, G., García, M.H., Fukushima, Y., YU, W. (1987). Experiments in turbidity currents over an erodible bed. *J. Hydr. Res.* 25, 123 – 147.

Parsons, J.D., García, M.H. (1998). Similarity of gravity current fronts. *Phys. Fluids* 10(12), 3209 – 3213.

Peters, W.D., Venart, J.E.S. (2000). Visualization of rough-surface gravity current flows using laser-induced fluorescence. In *Proc. 9th Int. Symp. of Flow Visualization*, Edinburgh.

Pokrajac, D., Kikkert, G.A. (2011). RADINS equations for aerated shallow water flows over rough beds. *J. Hydraul. Res.* 49(5), 630 – 638.

Price, J.F., Baringer, M.O. (1994). Outflows and deep water production by marginal seas. *Prog. Oceanogr.* 33, 161 – 200.

Princevac, M., Fernando, H.J.S., Whiteman, C.D. (2005). Turbulent entrainment into natural gravity-driven flows. *J. Fluid Mech.* 533, 259 – 268.

Raffel, M., Willert, C.E., Wereley, S.T., Kompenhans, J. (2007). *Particle Image Velocimetry. A practical guide*. Springer.

Ramaprabhu, P., Andrews, M.J. (2003). Simultaneous measurements of velocity and density in buoyancy-driven mixing. *Exp. Fluids* 34, 98 – 106.

Rossato, R., Alves, E. (2011). Experimental study of turbidity currents flow around obstacles. In *Proc. 7th Int. Symp. on Stratified Flows*, Rome, Italy.

Rottman, J.W., Simpson, J.E. (1983). Gravity currents produced by instantaneous releases of a heavy fluid in a rectangular channel. *J. Fluid Mech.* 135, 95 – 110.

Shin, J.O., Dalziel, B.S., Linden, P.F. (2004). Gravity currents produced by lock exchange. *J. Fluid Mech.* 521, 1 – 34.

Simpson, J.E. (1969). A comparison between laboratory and atmospheric density currents. *Quart.*

J. R. Met. Soc. 95, 758 – 765.

Simpson, J.E. (1972). Effects of the lower boundary on the head of a gravity current. *J. Fluid Mech.* 53(4), 759 – 768.

Simpson, J.E. (1997). *Gravity currents: in the environment and the laboratory.* 2nd ed. Cambridge University Press, New York.

Simpson, J.E., Britter, R.E. (1979). The dynamics of the head of a gravity current advancing over a horizontal surface. *J. Fluid Mech.* 93(3), 477 – 495.

Sveen, J.K. (2004). *An introduction to MatPIV v. 1.6.1.* Dept. of Math. University of Oslo.

Tanaka, M., Girard, G., Davis, R., Peuto, A., Bignell, N. (2001). Recommended table for the density of water between 0°C and 40°C based on recent experimental reports. *Metrologia (IOP Science)* 38, 301 – 309.

Thomas, L.P., Dalziel, S.B., Marino, B.M. (2003). The structure of the head of an inertial gravity current determined by particle-tracking velocimetry. *Exp. Fluids* 34, 708 – 716.

Tokyay, T., Mohamed, Y.A., Constantinescu, G. (2011). Effect of Reynolds number on the propagation of the lock exchange gravity currents in a porous medium. In *Proc. 34th IAHR Congress*, Brisbane, Australia, 2962 – 2969.

Ungarish, M., Zemach, T. (2005). On the slumping of high Reynolds number gravity currents in two-dimensional and axisymmetric configurations. *European Jounal of Mechanics B/Fluids* 24, 71 – 90.

Vanoni, V.A. (Ed.) (1975). *Sedimentation Engineering, manuals and reports on engineering practice no. 54*. American Society of Civil Engineers, New York.

Weiss, J. (1991). The dynamics of enstrophy transfer in two-dimensional hydrodynamics. *Physica D* 48, 273 – 294.

Wells, M.G. (2007). Influence of Coriolis forces on turbidity currents and their sediment patterns. In *Proc. Euromech Colloquium*.

Zhu, J.B., Lee, C.B., Chen, G.Q., Lee, J.H.W. (2006). PIV observation of instantaneous velocity structure of lock release gravity currents in the slumping phase. *Communications in Nonlinear Science and Numerical Simulation* 11, 262 – 270.

Appendix A

VELOCITY FILTER

The gate that separates the two volumes of fluid in the tank is removed manually, as fast as possible, in the beginning of each run. The fast removal of the gate induces oscillations in the water surface that are propagated to the flow, influencing the velocity field. The temporal series of the instantaneous streamwise velocity component show those oscillations with a well defined periodicity, as shown in Figure A.1(a), for a point located near the flow bed. The vertical velocity component, in the same point of the flow, does not seem to be affected by such oscillations (cf. Figure A.1b). However, as these oscillations are stronger near the free surface, the vertical velocity component for a point taken near the surface shows an oscillating pattern, as shown in Figure A.1(c).

Power spectral density function was obtained for the time-series of both velocity components and confirms the existence of a narrow frequency range, [0.20 0.25] Hz, related to the water surface oscillation, although with low energy. This can be seen in Figure A.2(a) for the streamwise velocity component in a point located near the flow bed and in Figure A.2(b) for the vertical velocity

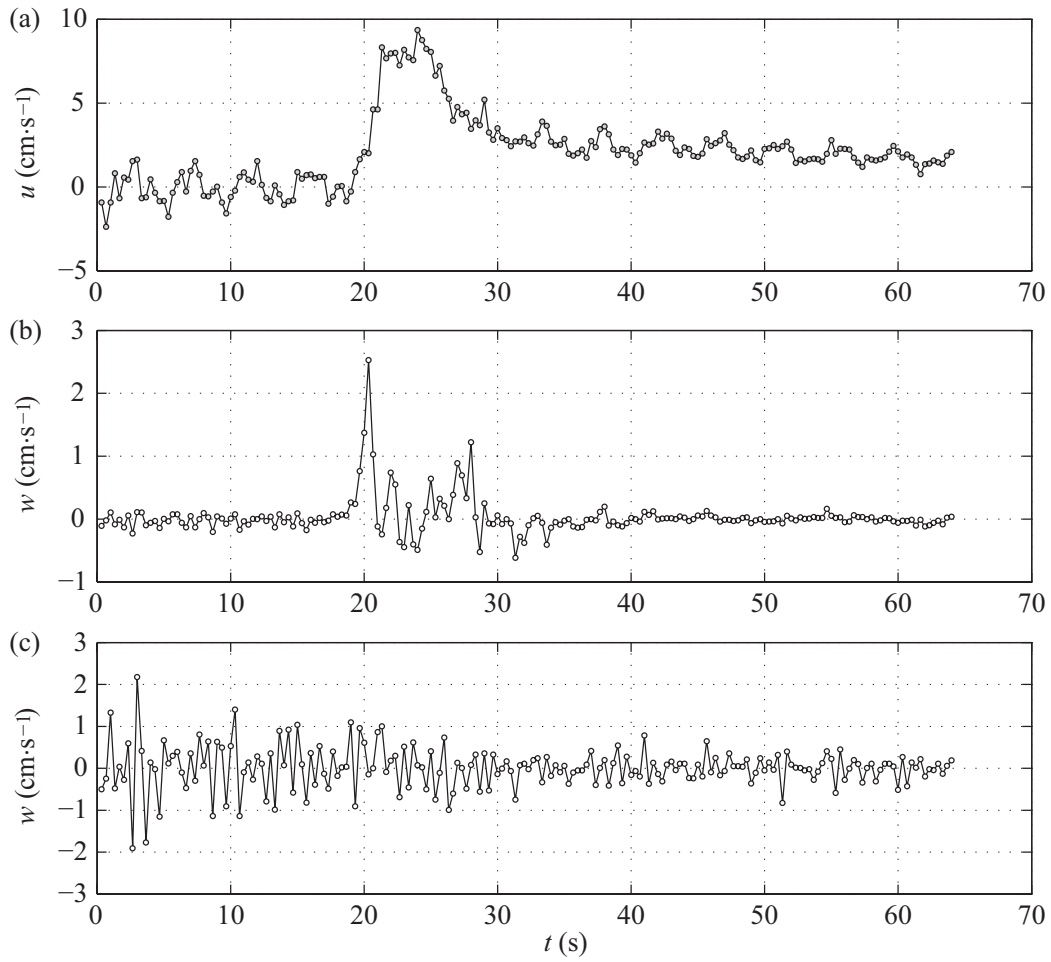

Figure A.1: Temporal series of the instantaneous velocity at a point within the flow: (a) and (b) streamwise and vertical components, respectively, at a point located near the flow bed $(x, z) = (164.7, 3.3)$ cm and (c) vertical velocity component at a point near the free surface $(x, z) = (164.7, 16.8)$ cm (cf. Figures 5.1 and 5.2 for location)

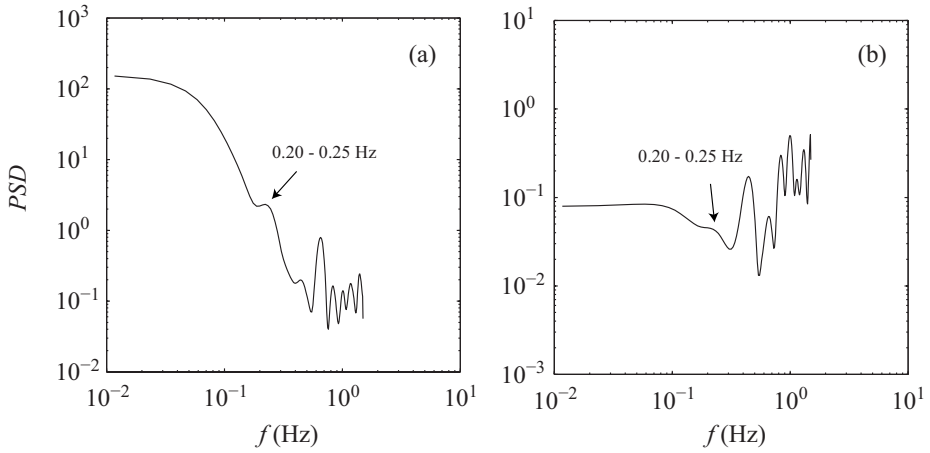

Figure A.2: Power spectral density of the temporal series of velocity: (a) u-component at a point located at $(x, z) = (164.7, 3.3)$ cm and (b) w-component at a point located at $(x, z) = (164.7, 16.8)$ cm

component in a point near the free surface.

To attenuate such oscillations, a Butterworth filter of 5^{th} order was applied to the temporal series of both velocity components at all points within the flow. The filter function 'filtfilt', implemented in the software MATLAB, has zero-phase distortion and was used to filter the velocity time-series. The resulting attenuation is smooth but effective in reducing the oscillations induced by the surface waves, as shown in the filtered time-series presented in Figure A.3 for a point near the flow bed. This filter was applied to the velocity data acquired with PIV, to both streamwise and vertical components, from where the results presented in Chapter5 are derived.

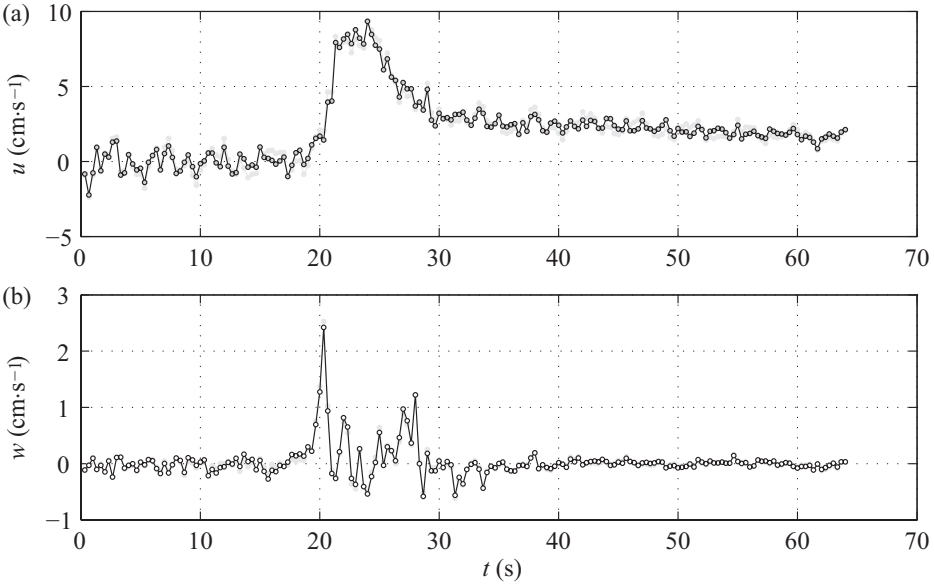

Figure A.3: Original (grey-shaded symbols) and filtered (symbols with black line in the edge) time-series of the streamwise velocity component (a) and vertical velocity component (b) at a point located at $(x, z) = (164.7, 3.3)$ cm

Appendix B

IDENTIFICATION OF REGIONS OF QUASI-STEADY STREAMWISE VELOCITY

The observation of the temporal series of the instantaneous streamwise velocity within the current, at a given point, revealed that during the passage of the head maximum values of u remain more or less constant, despite oscillations, for a certain period. After the head passed, the streamwise velocity decreases followed by another period of fairly constant streamwise velocity. These features are kept in the local time-series of the depth-averaged velocity, $u_d(t)$. The similarity of the times-series of u_d between streamwise locations (cf. Figure B.1) led to the computation of the spatial average of the depth-averaged velocity, $\langle u_d \rangle$, after each local time series being shifted in time in order to align the time of arrival of the current front at each streamwise location, providing an inertial reference system represented by the temporal scale t_{rel} in Figure B.2. The resulting series were shown in Chapter 5 (Figure 5.4) and below in Figure B.2 for one of the performed runs.

The accumulated sum of $\langle u_d \rangle$ revealed the existence of a linear phase associated to each quasi-steady region, in the gravity current head (A) and body (B), as shown in Figure B.3. The transition between regions A and B is clearly non-linear, as well as the region following region B. Therefore, these observations were used in the identification and isolation of regions A and B for further analysis. A linear regression with least squares method was applied to fit the accumulated sum data, allowing the identification of the linear phases in Figure B.3. Data sets composed by samples of different sizes were evaluated, being selected for each linear phase the larger data set corresponding to the maximum value of r^2. This procedure was applied to all runs and was the basis of the analysis and results presented in Chapter 5.

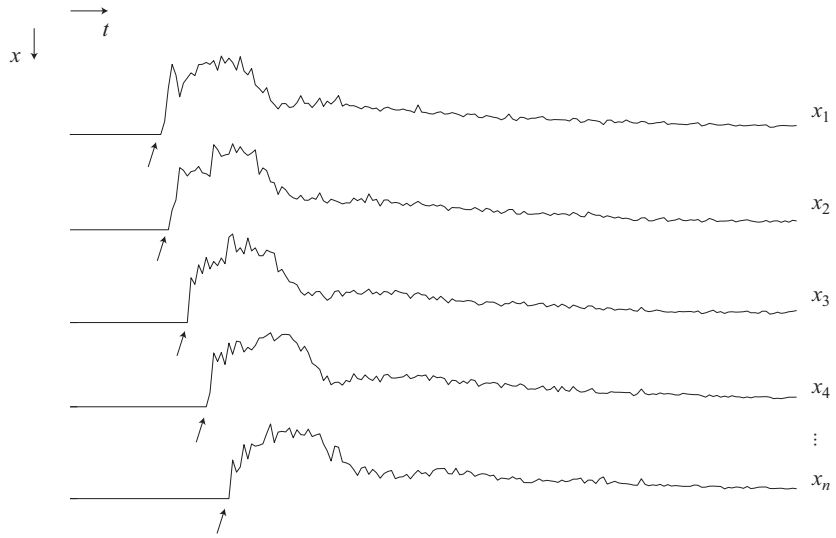

Figure B.1: Time series of the depth-averaged streamwise velocity component, $u_d(t)$, taken at different streamwise locations; arrows mark the arrival of the gravity current head to each streamwise location.

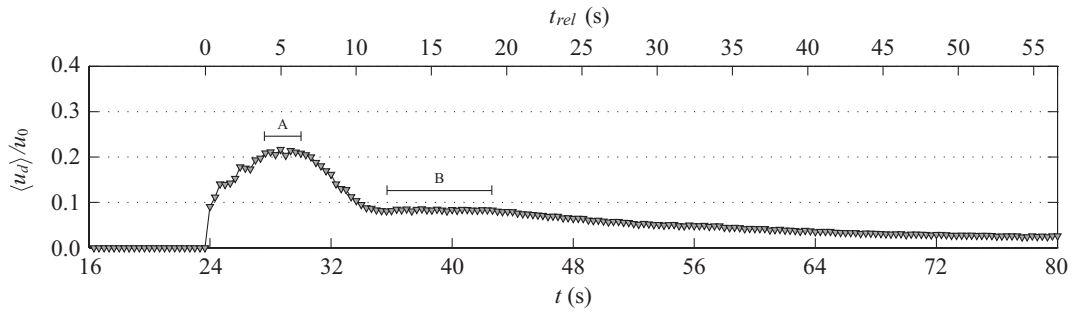

Figure B.2: Spatial averaged depth-averaged streamwise velocity, $\langle u_d \rangle$, for run R3

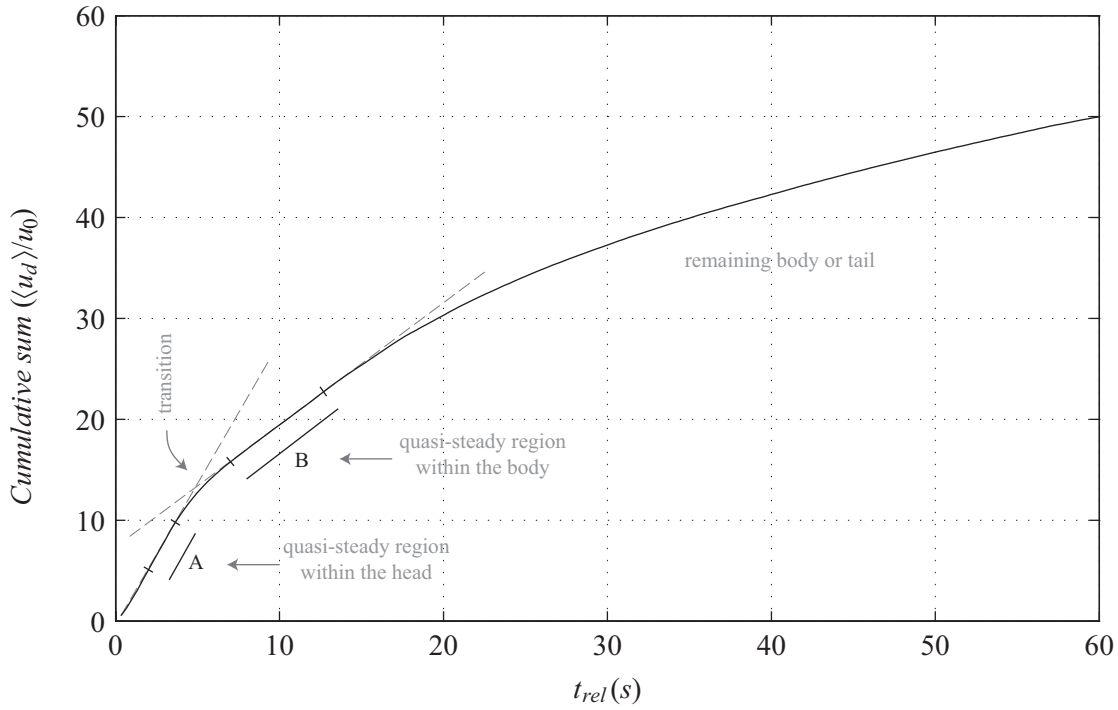

Figure B.3: Accumulated sum of $\langle u_d \rangle / u_0$.